

The role of decimeter-scale surface roughness in passive remote sensing of sea ice in L-band

Dissertation zur Erlangung des Doktorgrades
an der Fakultät für Mathematik, Informatik und Naturwissenschaften
im Fachbereich Geowissenschaften der Universität Hamburg

vorgelegt von

Maciej Miernecki

Hamburg

2017

Tag der Disputation: 14.07.2017

Folgende Gutachter empfehlen die Annahme der Dissertation:

Prof. Dr. Lars Kaleschke

und

Prof. Dr. Stefan Bühler

Day of oral defense: 14.07.2017

The following evaluators recommend the admission of the dissertation:

Prof. Dr. Lars Kaleschke

and

Prof. Dr. Stefan Bühler

To my Father and Grandfather.

Abstract

In this study we investigate the influence of large scale surface deformation on sea ice brightness temperature (T_B) at 1.4 GHz (L-band). Additionally we investigate the possibility of detecting the sea ice deformation with L-band radiometry.

The European Space Agency’s *SMOS* mission is the first space-borne radiometer carrying out multi-angular measurements at the frequency of 1.4 GHz. The L-band T_B is sensitive to sea ice thickness, and therefore is used for sea ice thickness retrieval over thin sea ice. Snow cover is another factor that influences the L-band T_B over sea ice, this property can be used to infer the snow depth over thick ice. However, the effect of the surface roughness on sea ice T_B is not well characterized.

In the following study we address this knowledge gap by using a combination of experimental data from field campaign and a sea ice emission model. We use the airborne laser scanner (*ALS*) to characterize sea ice surface roughness off-coast of Svalbard during *SMOSice2014* campaign. Then, we use the geometrical optics and surface slopes probability density functions to simulate emissions from a random faceted surface. Emissions from individual facets are calculated with **M**icrowave **L**-band **L**Ayered **S**ea ice emission model (*MILLAS*). Finally, we compare several simulations with different roughness setups with *EMIRAD2* radiometer data from *SMOSice2014* campaign.

We use areal photography to identify three ice types with distinct roughness features: “smooth ice”, “medium-deformed ice” and “deformed ice”. We calculate surface roughness statistics for each ice type: standard deviation of surface height (σ_z), mean square slope and the power spectral densities. The σ_z for “smooth ice” of 0.02 m is lower than the *ALS* accuracy of 0.025 m, for the “medium-deformed ice” and “deformed ice” the σ_z is 0.15 m and 0.25 m, respectively. In case of “medium-deformed ice” and “deformed ice” the auto correlation function is exponential.

We interpolate the *ALS* raw elevation data to obtain the digital elevation model (*DEM*) of the ice surface. The one-meter resolution of the *DEM* enables the characterization of large-scale surface roughness in terms of facets altering the local incidence angle. We found that facet slopes probability density distribution can be described by an exponential function ($PDF_\alpha \approx \exp(-\alpha/s_\alpha)$) with the slope parameter s_α . The values of s_α for the three labeled ice types are 0° , 8° and 15° , respectively. We observe a correlation of 0.68 between sea ice thickness and s_α . Additionally, we investigate the distribution of facet azimuthal orientation, which can be treated as isotropic only at scales greater than 4.3 km.

The PDF_α and *MILLAS* are integrated in a Monte Carlo method to simulate brightness temperature over sea ice with different degree of roughness. We found that as the surface gets rougher, the most pronounced change in T_B is the decrease in vertical polarization, which at high incidence angles can reach up to 8 K. Horizontal polarization is less affected, but still shows an up to 4 K increase for high incidence angles ($> 50^\circ$). The change at nadir is a decrease of less than 1 K for the most deformed

ice.

Based on the Monte Carlo simulations we developed a “Fast roughness model” directly calculating the T_B change as a function of s_α . The ‘Fast roughness model’ consists of parametrization of the polarization mixing and intensity change due to large scale roughness, the exact formula depends on permittivity and PDF_α of the surface. This method can be used with other surfaces.

We use the *SMOSice2014* ice thickness and surface temperature to simulate the T_B with the *MILLAS* model, and compare the simulations with radiometer data. Model setups are tested with and without surface roughness. We observe that for all pairs; simulation vs. radiometer channel, the root-mean-square error is around 27 K and the correlation coefficients do not exceed 0.3. Also, we found that inclusion of snow cover in the simulation setup is more significant than the inclusion of surface roughness. Setups with snow parametrization have higher fraction of explained variance (up to 0.08), whereas inclusion of surface roughness leads to much smaller improvements (from 0.005 to 0.01).

Zusammenfassung

In dieser Studie untersuchen wir den Einfluss der großflächigen Oberflächenverformung auf die Meereis-Helligkeitstemperatur (T_B) bei 1.4 GHz (L-Band). Zusätzlich untersuchen wir die Möglichkeit, die Meereisverformung mit Hilfe von L-Band-Radiometrie zu detektieren.

Die *SMOS* Mission der Europäischen Weltraumorganisation ist das erste Weltraumradiometer, das Messungen mit einer Frequenz von 1.4 GHz unter verschiedenen Einfallswinkeln durchführt. Die L-Band T_B ist empfindlich gegenüber Meereisdicke und wird daher für die Meereisdicken-Berechnung über dünnem Meereis verwendet. Schneebedeckung ist ein weiterer Faktor, der die L-Band T_B über dem Meereis beeinflusst. Diese Eigenschaft kann verwendet werden, um auf die Schneetiefe über dickem Eis zu schließen. Die Wirkung der Oberflächenrauigkeit auf Meereis T_B ist bisher nicht gut beschrieben.

In der folgenden Studie untersuchen wir diese Wissenslücke mit einer Kombination aus experimentellen Daten aus einer Feldkampagne und einem Meereis-Emissionsmodell. Wir verwenden den airborne laser scanner (*ALS*), um die Meereisoberflächenrauigkeit vor der Küste von Svalbard während der *SMOSice2014* Kampagne zu beschreiben.

Dann verwenden wir die geometrische Optik und die Wahrscheinlichkeitsdichtefunktion der Oberflächenneigung, um Emissionen einer zufällig facettierten Oberfläche zu simulieren. Die Emissionen jeder zufälligen Oberfläche werden mit dem **M**icrowave **L**-band **L**Ayered **S**ea ice emission model (*MILLAS*) berechnet. Schließlich vergleichen wir mehrere Simulationen für verschiedene Rauigkeits-Setups mit *EMIRAD2* Radiometerdaten von der *SMOSice2014* Kampagne.

Wir verwenden die Luftfotografie, um drei Eisarten mit ausgeprägten Rauigkeitsmerkmalen zu identifizieren: "Glattes Eis", "mittelmäßigverformtes Eis" und "deformiertes Eis". Wir berechnen die Oberflächenrauigkeitsstatistiken für jeden Eisstyp: Standardabweichung der Flächenhöhe (σ_z), mittlere quadratische Steigung und spektrale Leistungsdichte. Die σ_z für "glattes Eis" von 0.02 m ist niedriger als die *ALS* Genauigkeit von 0.025 m; für "mittelverformte Eis" und "deformiertes Eis" ist σ_z 0.15 m und 0.25 m. Im Falle von "mittelverformtem Eis" und "deformiertem Eis" ist die Autokorrelationsfunktion exponentiell.

Wir interpolieren die Rohdaten der *ALS* Höhen, um das digital elevation model (*DEM*) der Oberfläche zu erhalten. Die Ein-Meter-Auflösung des *DEM* ermöglicht die Charakterisierung einer großflächigen Oberflächenrauigkeit in Form von Facetten, die den lokalen Einfallswinkel verändern. Wir haben festgestellt, dass die Wahrscheinlichkeitsdichteverteilung der Oberflächenneigung durch eine exponentielle Funktion ($PDF_\alpha \approx \exp(-\alpha/s_\alpha)$) mit dem Slope-Parameter s_α beschrieben werden kann. Die Werte von s_α für die drei bezeichneten Eisarten sind 0° , 8° und 15° . Wir beobachten eine Korrelation von 0,68 zwischen Meereisdicke und s_α . Darüber hinaus

untersuchen wir die Verteilung der azimuthalen Facettenorientierung, die nur bei Skalen größer als 4.3 km als isotrop angesehen werden kann.

Die PDF_α und *MILLAS* sind in einer Monte-Carlo-Methode integriert, um die Helligkeitstemperatur über Meereis mit unterschiedlichem Rauigkeitsgrad zu simulieren. Wir haben festgestellt, dass, für rauere Oberflächen die stärkste Änderung in T_B die Abnahme der vertikalen Polarisation ist, die bei hohen Einfallswinkeln bis zu 8 K reichen kann. Die horizontale Polarisation ist weniger betroffen, zeigt aber immer noch eine Erhöhung von bis zu 4 K für hohe Einfallswinkel ($> 50^\circ$). Bei Nadir nimmt T_B um weniger als 1 K bei dem am meisten deformierten Eis ab.

Basierend auf den Monte Carlo Simulationen entwickelten wir ein “Fast roughness model”, das die T_B Änderung direkt als Funktion von s_α beschreibt. Das “Fast roughness model” besteht aus der Parametrisierung der Polarisationsvermischung und der Intensitätsänderung aufgrund der großen Rauigkeit. Die genaue Formel hängt von Permittivität und PDF_α der Oberfläche ab. Diese Methode kann auch für andere Oberflächen verwendet werden.

Wir verwenden die *SMOSice2014* Eisdicke und Oberflächentemperatur, um die T_B mit dem *MILLAS* Modell zu simulieren und die Simulationen mit Radiometerdaten zu vergleichen. Modell-Setups werden mit und ohne Oberflächenrauigkeit getestet. Wir beobachten, dass für alle Paare “Simulations-Radiometerkanal” der mittlere quadratische Fehler um 27 K liegt und die Korrelationskoeffizienten nicht mehr als 0.3 betragen. Auch stellen wir fest, dass die Einbeziehung der Schneedecke im Simulationsaufbau wesentlich wichtiger ist als die Einbeziehung der Oberflächenrauigkeit. Setups mit Schneeparametrisierung erklären einen höheren Bruchteil der Varianz (bis zu 0,08), während die Integration der Oberflächenrauigkeit zu wesentlich kleineren Verbesserungen führt (von 0.005 bis 0.01).

Contents

Abstract	i
Zusammenfassung	iii
1 Introduction	1
2 Data	7
2.1 The SMOS mission	7
2.1.1 The SMOS measurements	8
2.2 SMOSice2014 campaign	10
2.2.1 Airborne laser scanner	12
2.2.2 EMIRAD2 radiometer	14
3 Methods	21
3.1 Brightness temperature	21
3.2 Brightness temperature over sea ice	24
3.3 Sea ice emission model	25
3.4 Surface roughness	28
3.4.1 Impact on surface reflectivity	28
3.4.2 Semi-empirical roughness model for surface reflectivity	30
3.4.3 Rough surface scattering models	30
3.5 Sea ice roughness	31
3.6 Merging the geometrical optics with the radiation model	35
3.7 Summary	36
4 Surface roughness characteristics during SMOSice2014	39
4.1 Sea ice classification	39
4.2 Power spectral densities	42
4.3 Geometrical optics and facet slopes orientation	44
4.4 Summary and discussion	49
5 Influence of the surface roughness on the modeled brightness temperature	51
5.1 The sensitivity study	51

5.1.1	The impact of ice concentration	52
5.1.2	The impact of ice thickness	53
5.1.3	The impact of snow thickness	55
5.1.4	The impact of surface temperature	56
5.1.5	The impact of large scale surface roughness	57
5.2	The assessment of uncertainty factors in the modeled brightness temperature	58
5.3	Fast roughness model	61
5.4	Extending the parametrization for other surfaces	65
5.5	Summary and discussion	68
6	The influence of surface roughness in the measured brightness temperature	71
6.1	The emissivity model setup	71
6.2	Brightness temperature: modeled vs. measured	72
6.3	Summary and discussion	80
7	Summary and conclusions	81
7.1	Back to the research questions	82
	Appendix	vi
	A Coordinates of the identified ice types	vii
	B Atmospheric corrections	ix
	Acronyms	xi
	List of Figures	xvii
	List of Tables	xix
	References	xxviii
	Danksagung	xxix

Chapter 1

Introduction

Sea ice is one of the essential climate variables, its thickness and extent play key roles in the climate system (Bojinski et al., 2014). Forming of the sea ice releases heat, therefore the sea ice volume is an important factor in a polar energy budget. Another consequence of sea ice formation is the release of salts, the process which is essential for deep water formation (Aagaard and Carmack, 1989). Furthermore, the sea ice influences gas, heat and momentum transfer between the ocean and the atmosphere (Maykut, 1978; Loose et al., 2011). Under sufficient stress exerted by the winds and ocean currents sea ice can diverge and break apart or converge and pile up forming a region of thicker and deformed ice with pressure ridges. The regions with high density of pressure ridges drift differently than the level ice, due to their higher form drag (Arya, 1973; Tsamados et al., 2014). Those regions of thicker ice are of spatial interest for commercial activities involving ice braking ships and offshore constructions, since ridged ice poses danger to navigation (Timco and Weeks, 2010; Øystein Jensen, 2016). Thus the knowledge of the ice thickness and location of the ridged ice is of interest for climate studies and exploration of the polar regions, alike.

The Soil Moisture and Ocean Salinity (*SMOS*) mission carries the first spaceborne radiometer that makes full-polarization, multi-angular radiation measurements at a frequency of 1.4 GHz, in the L-band (Kerr et al., 2010). At this frequency, the corresponding wavelength of 21 cm is larger than for any of the previous passive microwave sensors in orbit. The key advantage of a larger wavelength is that the radiation registered by the radiometer originates from greater depths in the ice (Carsey, 1992, pp. 63; Ulaby et al., 2014, pp. 139). Thus, the L-band brightness temperature (T_B) is sensitive to sea ice thickness, a feature that is used for sea ice thickness retrieval from *SMOS* (over thin ice) (Tian-Kunze et al., 2014; Kaleschke et al., 2016).

Several factors influence the T_B measured over ice-covered regions: ice concentration, ice temperature, snow cover and surface roughness are among them (Maaß et al., 2013; Ulaby et al., 2014, pp. 422).

Here, we investigate the effect of surface roughness on the L-band T_B , a factor that

has not been included so far in modeling of the ice emissions and in operational sea ice thickness retrieval from *SMOS*. Hence, my research questions are:

- How are the angular T_B characteristics changing with increasing roughness of the sea ice surface?
- What is the magnitude of those changes in comparison to other factors, such as sea ice concentration?
- Is it possible to measure the sea ice deformation with multi-angular *SMOS* data?

To answer these questions, we use a combination of radiative transfer modeling, air-borne data and satellite observations.

Sea ice thickness measurements and L-band radiometry

Measuring sea ice thickness from the Earth orbit is a tool that enables daily coverage of the polar regions. Several techniques are applied for the global surveying of sea ice thickness. Altimeter-based techniques rely on measurements of ice freeboard from which the total ice thickness is calculated (Zwally et al., 2002; Laxon et al., 2013; Abdalati et al., 2010). However, this method applies only to thick ice, as the freeboard measurement uncertainty for thin ice (approx. less than 1 m), impedes the retrieval (Wingham et al., 2006; Ricker et al., 2014a). The thickness of thin ice can be measured with thermal infrared sensors (Yu and Rothrock, 1996). This method is in turn limited to cold clear-sky cases and prone to errors caused by thin clouds and fog (Yu and Rothrock, 1996; Mäkynen et al., 2013). Considering these limitations, the sea ice thickness retrieval with L-band radiometry complements the above mentioned techniques.

The introduction of the satellites with L-band radiometers (In this work we adopt the band nameing according to the IEEE Standard 521-2002, L-band:1 to 2 GHz. All the radiometers mentioned in this thesis work in a restricted for passive use only band; from 1.400 to 1.427 GHz, therefore hereinafter by L-band we mean 1.4 GHz.) provides the possibility of monitoring the thin sea ice thickness with passive microwave (*PM*) (Lagerloef et al., 2008; Kerr et al., 2010; O'Neill et al., 2010). The L-band T_B is sensitive to sea ice thickness (Kaleschke et al., 2010, 2012; Huntemann et al., 2014), and therefore can be used for operational sea ice thickness retrieval (Tian-Kunze et al., 2014). Apart from ice thickness, other factors influence the L-band T_B over ice covered ocean. For example Maaß et al. (2013) developed and used the **MI**crowave **L**-band **LA**yered **S**ea ice emission model (*MILLAS*) to investigate the effects snow cover. According to their results, snow causes an increase of the T_B , with a most

pronounced change at horizontal polarization. However, the surface roughness was so far omitted from the modeling of the T_B over sea ice. Mills and Heygster (2011) used ice topography obtained from ice thickness measurements to characterize surface roughness. They evaluated the effect of a local incidence angle on the measured T_B . Their result suggests that roughness on the ridged ice makes a significant contribution to the measured signal. Nonetheless, the later result was derived based on 1-D linear ice elevation measurements spaced every 2 to 4 m, a sampling that barely covered the elliptical radiometer footprint of 250 m. Thus a better validation data set combining the radiometer data with high-resolution wide-swath surface elevation measurements is needed.

Brightness temperature observed during “SMOSice2014” campaign

The *SMOSice2014* campaign took place in March 2014 in the area between Edgeøya and Kong Karls Land, east of Svalbard (Kaleschke et al., 2016). On April 24, 2014, the Polar 5 research aircraft flew along two lines over sea ice west of Edgeøya. Among instruments on board the airplane were the airborne laser scanner (*ALS*), the L-band radiometer *EMIRAD2* developed by DTU-Space (Søbjaerg et al., 2013), a *KT19* infrared thermometer and an aerial camera.

The *EMIRAD2* radiometer had two antennas, the first pointing at nadir and the second side-looking at 40° . Both antennas were registering surface emissions at horizontal and vertical polarizations. The infrared thermometer was pointing at nadir. The *ALS* elevation measurements were spaced every 0.2 m along a 70 m scan line in cross-track direction and every 0.5 m along flight direction, covering the entire nadir-looking radiometer footprint.

The obtained surface elevation measurements were used to infer the sea ice thickness from sea ice freeboard. On figure 1.1 on page 4, *EMIRAD2* nadir T_B is plotted against sea ice thickness, there is a $\approx 10 \text{ K m}^{-1}$ increase in nadir T_B over thick ice ($>0.7 \text{ m}$), despite *MILLAS* model prediction plotted as a green dashed line (*MILLAS* setup consisted of one ice layer, permittivity parametrized by ice thickness and temperature).

The radiometer and elevation data collected during the campaign provide an opportunity to test our hypothesis whether the surface roughness can be the cause of the observed T_B increase over thick ice.

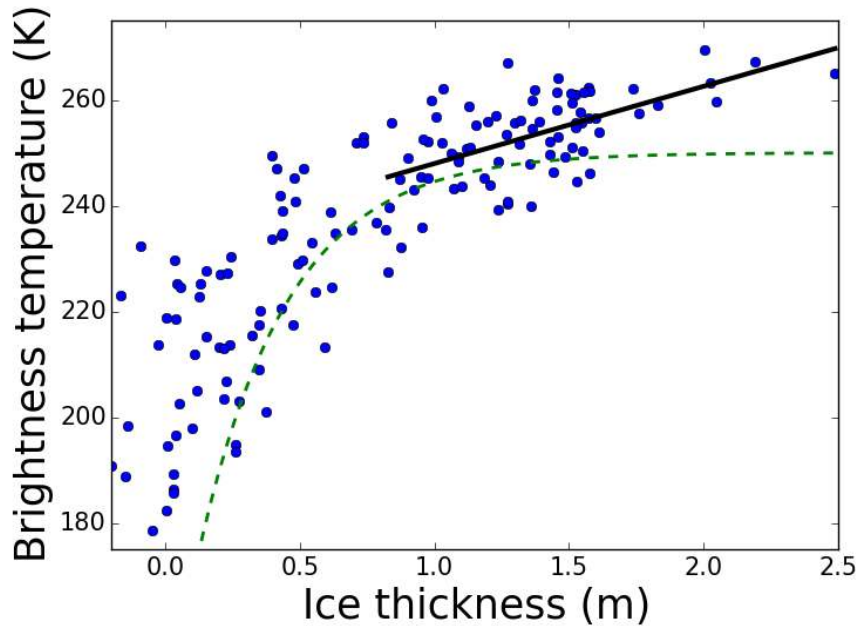


Figure 1.1: Nadir brightness temperature vs. sea ice thickness, measurements from *SMOSice2014*, averaged every 60 s. The *green dashed line* marks the *MILLAS* model prediction. The *black line* marks a linear fit for ice thicker than 0.7 m.

Sea ice surface roughness

The roughness of a random surface is characterized by statistical parameters such as the standard deviation of surface height (σ_z), and the correlation function ($R(\xi)$) measured in units of wavelength (Ulaby et al., 2014, pp.422). The measurements of surface elevation (z), from which the roughness statistics are drawn, are conducted with altimeters characterized by their accuracy (δ) and sampling distance (Δx). Thus, the measurement method has an impact on the result by filtering out spatial frequencies. The sea ice elevation measurements obtained from air-borne altimeters (Ketchum, 1971; Dierking, 1995), supplemented with terrestrial laser scanners (Landy et al., 2015), draw a picture of sea ice roughness as a multi-scale feature covering several orders of magnitude from large floes and pressure ridges of tens and hundreds meters to frost flowers and small ripples of centimeters to millimeters scales.

The incident wavelength reacts differently with individual components of the superimposed roughness (Ulaby et al., 2014). The roughness scales much greater than the electromagnetic wavelength (λ) alter the local incidence angle. On the other end of spectrum, when the change of the surface elevation Δz over sampling distance Δx is much smaller than λ , the roughness stays unnoticed. As a rule of thumb, Δx should be smaller than 0.1λ (Dierking, 2000; Ulaby et al., 2014).

Sea ice roughness measurements with terrestrial lidar carried out by Landy et al.

(2015) show that σ_z ranges from 0.10 cm to 0.64 cm, after high-pass filtering (cut off at 0.25 m, $\Delta x = 2$ mm). These results indicate that, according to the Fraunhofer smoothness criterion (eq. 3.13), most sea ice types (except artificially grown frost flowers), can be treated as a smooth surface in L-band at scales lower than 0.25 m.

Sea ice is “electromagnetically smooth” in L-band at a scale up to 0.25 m. Studies of surface scattering with numerical simulations conclude that a region of $8\lambda \times 8\lambda$ is large enough to represent surface roughness in scattering models (Lawrence et al., 2011, 2013). Hereby we assume that scales greater than 8λ can be characterized in terms of Geometrical Optics (*GO*). In *GO* the surface is represented as a set of facets (Ulaby et al., 2014). This approach was applied in modeling the effective emissivities of mountainous terrain (Matzler and Standley, 2000), as well as other surfaces such as sea (Prigent and Abba, 1990). The latter used probability distribution of slopes in across- and downwind directions. A similar method was used in the context of sea ice to assess the uncertainties caused by the roughness in sea ice concentration products derived from *PM* (Stroeve et al., 2006). Liu et al. (2014) measured ice surface slopes and other roughness statistics in Bohai Sea, but their result was obtained with linear (1-D) scans under the assumption of isotropic roughness characteristics. The study by Beckers et al. (2015) has demonstrated that the statistics of sea ice roughness (mean z , σ_z , kurtosis and skewness) obtained from 1-D altimeter and 2-D laser scanner converge, provided that the surface is not strongly heterogeneous. Nonetheless, the 1-D altimeter data cannot properly represent the spatial orientation of the surface facets, whose orientation is characterized by both slope (α) and azimuthal angles (γ).

In this work, we address the issue of surface slope orientation by extracting this information from digital elevation model (*DEM*) obtained with 2-D *ALS* measurements. Then we identify the spatial scales at which sea ice can be treated as isotropic in terms of surface slopes orientation. The surface roughness statistics are subsequently used in combination with the *MILLAS* model to simulate the brightness temperature over ice with different roughness. Finally, we compare *EMIRAD2* data with modeled T_B with and without roughness parametrization.

Outline

This thesis is organized as follows:

In Chapter 2 we present the data sets used in this study. First, we introduce the *SMOS* mission and the measuring principle of its radiometer. Then we describe the *SMOSIce2014* campaign with an emphasis on the airborne radiometer and the surface elevation measurements.

In Chapter 3 we summarize the theoretical basis for the subsequent analysis. We shortly present the concept of brightness temperature and its relation to surface scattering. Then we describe the sea ice emission model *MILLAS*. Furthermore,

we present various scattering approximations and argue for geometrical optics as the most suitable. Finally, we integrate the *MILLAS* model with statistical distribution of surface slopes into the Monte Carlo roughness model.

In Chapter 4 we show the results of sea ice classification based on aerial photography. Surface roughness statistics for each of the ice type: smooth, medium-deformed and deformed are presented. Based on the *DEM* we analyze the spatial variability of surface slopes, then we compute the probability density functions of surface slopes for each ice type.

In Chapter 5 we use the surface slopes statistics with our Monte Carlo roughness model to evaluate the influence of large scale surface roughness on the modeled T_B . We quantify the method's sensitivity to the input parameters. Subsequently, we parametrize the model results with an analytical function ("fast roughness model"). We also demonstrate the possibility of extending the parametrization on surfaces with different permittivities.

In Chapter 6 we compare the *SMOS* and *EMIRAD2* brightness temperatures from the *SMOSice2014* campaign with the results obtained with our statistical roughness model. We analyze the percentage of explained variance, bias and root-mean-square error.

Chapter 7 presents a summary of the main conclusions of this work.

Chapter 2

Data

In this chapter we provide a description of the main data sets used in this study. In section 2.1 we briefly summarize the measuring principles of the *SMOS* mission and its implications for the brightness temperature data. The *SMOS* brightness temperatures are used for the large scale analysis and comparisons. In section 2.2 we introduce the *SMOSice2014* measurement campaign. We choose this data set because it combines the high resolution surface elevation measurements with simultaneously registered radiometer data. The surface elevation and radiometer data collected during *SMOSice2014* campaign play a central role in our study of the influence of the surface roughness on the L-band T_B .

2.1 The *SMOS* mission

The Soil Moisture and Ocean Salinity mission (*SMOS*) was launched in November 2009 as part of European Space Agency (*ESA*) Earth Explorers program. The satellite orbits the Earth at the altitude of 765 km with a period of approximately 100 min (Kerr et al., 2010). The *SMOS* payload is a 2D, L-band passive microwave interferometer: the Microwave Imaging Radiometer using Aperture Synthesis (*MIRAS*) (McMullan et al., 2008).

The *MIRAS* radiometer consist of 69 receivers distributed over the satellite's central hub and three outward stretching 4 m-long arms. The interferometric 2D image reconstruction technique is based on the cross-correlation between the receiver pairs, so the phase difference of the incident radiation registered at individual receivers is measured (McMullan et al., 2008). Thanks to this technique it is possible to disentangle the radiation originating from different regions/footprints of the *SMOS* field of view. The reconstruction produces an image of the Earth's T_B in the satellite reference frame every 1.2 s. The image has a hexagonal shape, but due to the satellite tilt its projection on the Earth's surface has an elongated hexagonal shape hundreds kilometers across. The projected 2D image is called a snapshot, an example of which is presented in

figure 2.1. The color scale represents the values of incidence angles across the snapshot. As the satellite passes over a fixed region on the Earth’s surface, it registers the T_B originating from the region in several snapshots. But in each snapshot the region has a different position, and it is observed under a different incidence angle. The result of an overpass is an angular characteristic of the L-band radiation originating from the region.

Before we proceed to the more detailed analysis of the antenna footprint, it is important to mention that the brightness temperature registered by *SMOS* is expressed in the antenna reference frame, which changes with instrument orientation in space. In order to obtain the angular characteristic of the T_B in Earth’s local horizontal and vertical polarization coordinates several factors must be accounted for. First, there is the geometrical rotation of the antenna frame with respect to the part of the snapshot. Second the Faraday rotation should be considered: it is a phenomena caused by the interaction of the incident radiation with the Earth’s magnetic field and the free electrons in the ionosphere, which causes the rotation of the plane of polarization. Third, the satellite measures the T_B at the top of the atmosphere (*TOA*). In order to obtain the emissions specific to the Earth’s surface a correction accounting for the atmospheric emission and attenuation, has to be applied. The atmospheric emission and attenuation factors in L-band are mainly functions of the oxygen and water vapor concentration in the atmosphere. The model studies indicate that total atmospheric correction ranges from 2.6 K at nadir up to 5.6 K in horizontal polarization at 56° incidence angle (Zine et al., 2008).

2.1.1 The SMOS measurements

The radiometric accuracy of the T_B measurements varies across the footprint. Due to the image reconstruction accuracy depends on the surface type (land, sea) and on the contrast between the observed T_B s within field of view, as well on the position in the antenna footprint (Corbella et al., 2014; Soldo et al., 2015). The best accuracy is achieved in the central part of the snapshot. After six years in orbit, *SMOS* maintains the designed performance, the instrument’s radiometric accuracy over the whole snapshot is of about 1.5 K and 2 K for the X and Y polarization respectively (Martín-Neira et al., 2016). However, the overall uncertainty of an individual T_B measurement exceeds these values because of other factors such as thermal stability, image reconstruction issues or radio frequency interference. For the core applications the radiometric uncertainty are meeting the design criteria: between 3.5 K and 5.8 K over land and 2.5 to 4.1 K over ocean (Kerr et al., 2010).

The *SMOS* brightness temperature data are projected onto a Discrete Global Grid (*DGG*). For this purpose the *ISEA4H9* grid was chosen. It has a hexagonal grid cell shape of 15 km (Suess et al., 2004), so it can maintain the full information content of *SMOS* measurements, as well as minimize the interpolation errors. The

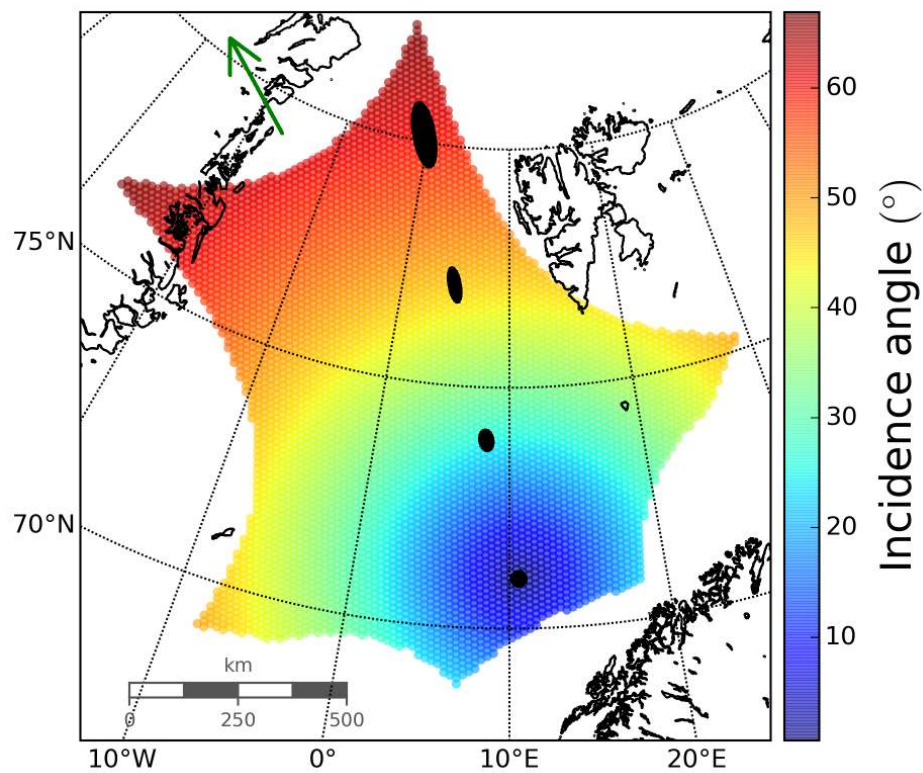


Figure 2.1: Example of a *SMOS* snapshot, taken south-west of Svalbard on March 24th, 2014. Individual granules of the 15 km ISEA 4H9 grid are marked with circles. The colors indicate the incidence angle associated with *DGG* pixels. The black ellipsoids illustrate the orientation and relative size of the individual measurement footprints (not to scale).

snapshot geometry and the image reconstruction cause a variation in footprint size and orientation. The general formula describing the individual beam footprint involves detailed information about the antenna gains of all the receivers. In practice, a simplified formula is used to calculate the beam footprint size and orientation (WEF_A , notation taken from the technical documentation) (Kerr et al., 2011):

$$WEF_A(\rho_{DC}) = \begin{cases} \frac{\text{sinc}(73.3 \cdot \rho_{DC})^{1.4936}}{1 + 524.5 \cdot (\rho_{DC})^{2.1030}}, & \text{for } \rho_{DC} \cdot 73.3 \leq \pi \\ 0, & \text{otherwise} \end{cases} \quad (2.1)$$

where ρ_{DC} is the distance from the beam's center expressed in directional cosines. Figure 2.2 shows the footprint size calculated according to the formula (2.1). For some applications, such as soil moisture retrieval, the formula can be simplified even further. The Mean antenna weighting function (Mean_ WEF), which neglects the incidence angle and geometrical rotation effects, is described by:

$$\text{Mean_}WEF(\rho_{earth}) = \begin{cases} WEF_A(\rho_{earth} \cdot \pi/2932) + 0.02, & \text{for } \rho_{earth} \in [0 \text{ km}, 40 \text{ km}] \\ 0.02, & \text{for } \rho_{earth} \in]40 \text{ km}, 61.5 \text{ km}] \\ 0, & \text{otherwise} \end{cases} \quad (2.2)$$

where ρ_{earth} is the distance from the projection of the beam's center on the Earth's surface expressed in kilometers.

2.2 SMOSice2014 campaign

The *SMOSice2014* campaign took place on the 24th and 26th of March 2014 in the area between Edgeøya and Kong Karls Land, east of Svalbard. A broader description of the campaign was made by Kaleschke et al. (2016). At this point we evoke just the parts relevant to the current work.

In the period preceding the experiment, from late January until early March, the meteorological conditions in the region deviated strongly from the climatological means. The air temperature measured at Hopen Island meteorological station was on average 9 to 12°C higher than the climatological value for the period 1961 to 1990 (Strübing and Schwarz, 2014). Prevailing southerly winds pushed sea ice against the coasts of Nordaustlandet and into Hinlopen Strait, leaving a small strip of compacted ice along the coasts of Edgeøya. When sea ice returned with southerly drift in early March, it set a scene for the experiment. The thickest, most deformed ice was located in the western part of the studied region with gradual decrease in thickness eastwards, where thin newly-formed ice was dominant. This pattern can be observed in the *SMOS* sea ice thickness product displayed on figure 2.3. In this work we analyze only the data

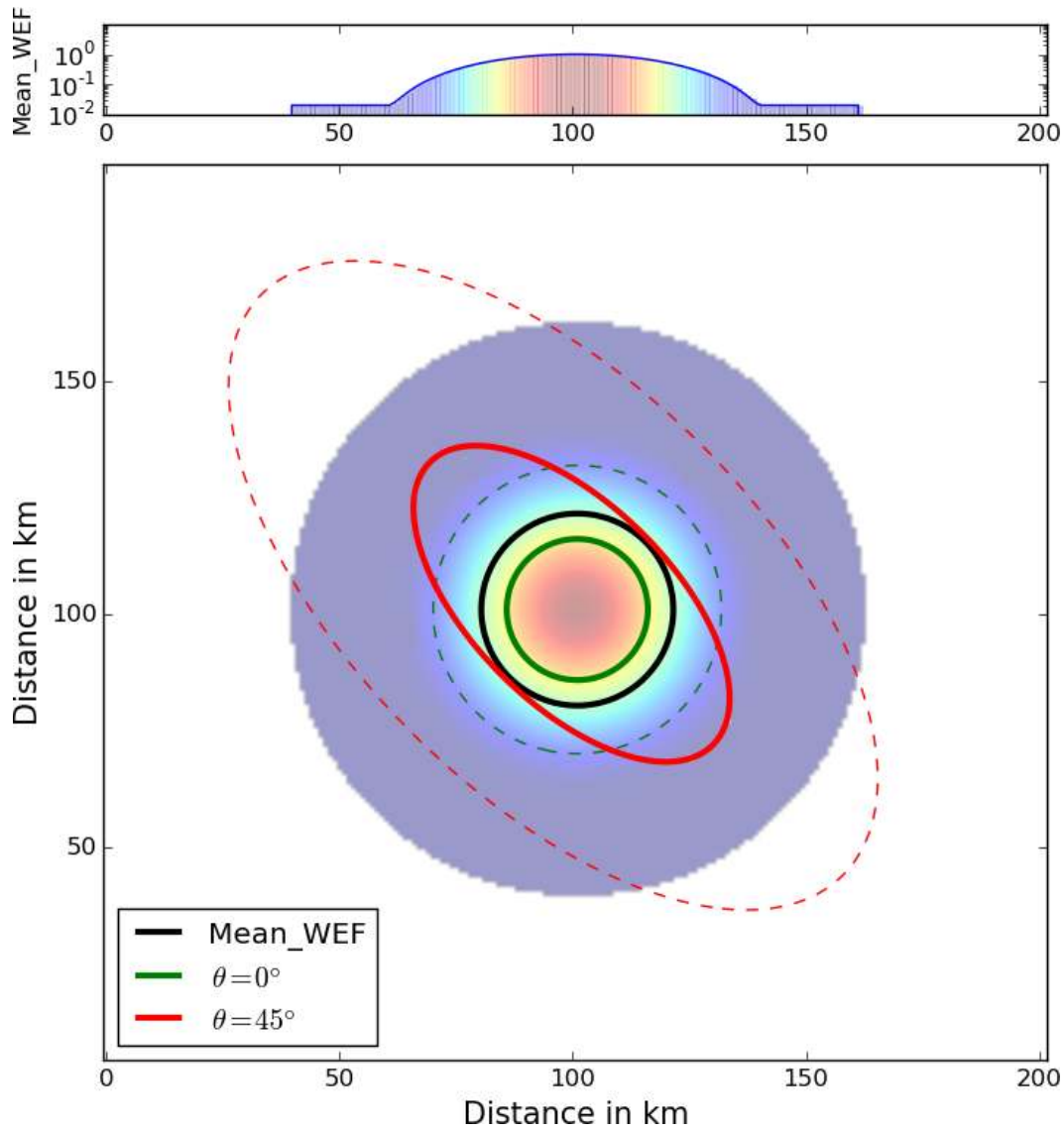


Figure 2.2: *SMOS* Antenna patterns. The -3 dB footprint contours are marked in *solid lines*, the -20 dB contours are marked in *dashed lines*. The mean antenna weighing function (Mean_WEF) approximation is plotted as a color background, with a color scale showed in subplot above in a cross section of the Mean_WEF cutting through the center. The actual size for the nadir *SMOS* measurement is showed in *green*. The elongated *elliptical red contours* correspond to the footprint at 45° incidence angle.

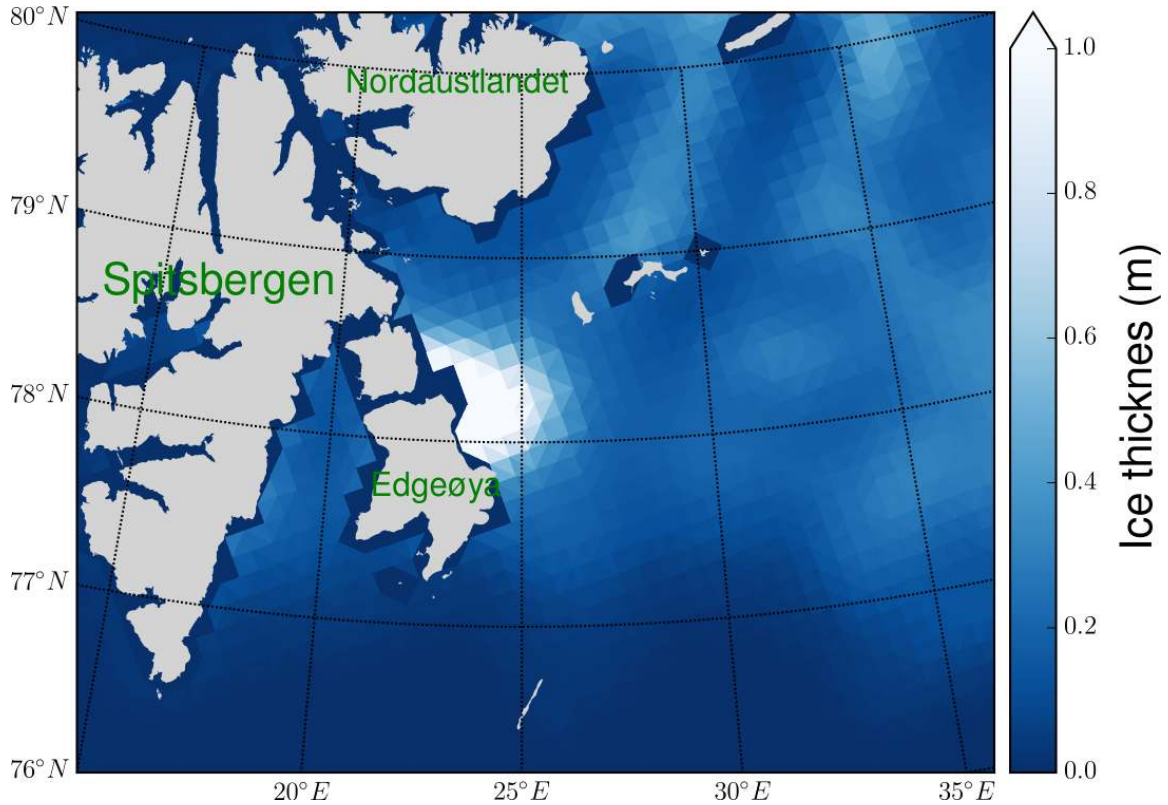


Figure 2.3: Sea ice thickness on March 24, 2014 derived from SMOS. The SMOS sea ice thickness product with resolution of 40 km is presented on 15 km grid. An aggregation of thick ice (>1 m) is visible along the Edgeøya’s eastern coast.

from the low altitude flight at 70 m, as it has the highest spatial resolution of the *ALS* data among all the flights. Also, we limit the analysis to the 24th of March, it is due to the fact that the region covered on 26th March had a discontinuous ice cover and a large scale swell was interfering with the surface elevation measurements.

On March 24, the *Polar 5* research aircraft of the Alfred Wegener Institute (Bremenhaven, Germany), undertook measurement flights starting from the eastern coast of Edgeøya, along the lines marked in red on the figure 2.4. The figure also shows TerraSAR wide swath scenes, taken in the region. Flight **A** was made between 10:05 and 10:41 UTC, flight **B** from 11:25 to 12:07 UTC. A set of instruments was mounted on the aircraft, including an aerial camera to visually register the ice conditions, the Heitronics Kt19.85 pyrometer for surface temperature measurements, the L-band radiometer *EMIRAD2* and the Airborne Laser Scanner (*ALS*) for high-resolution surface elevation measurements.

2.2.1 Airborne laser scanner

An instrument essential to this study is the Riegel VQ-580 laser scanner mounted on the Polar5 aircraft. Its near infrared laser (wavelength 1064 nm) is measuring snow

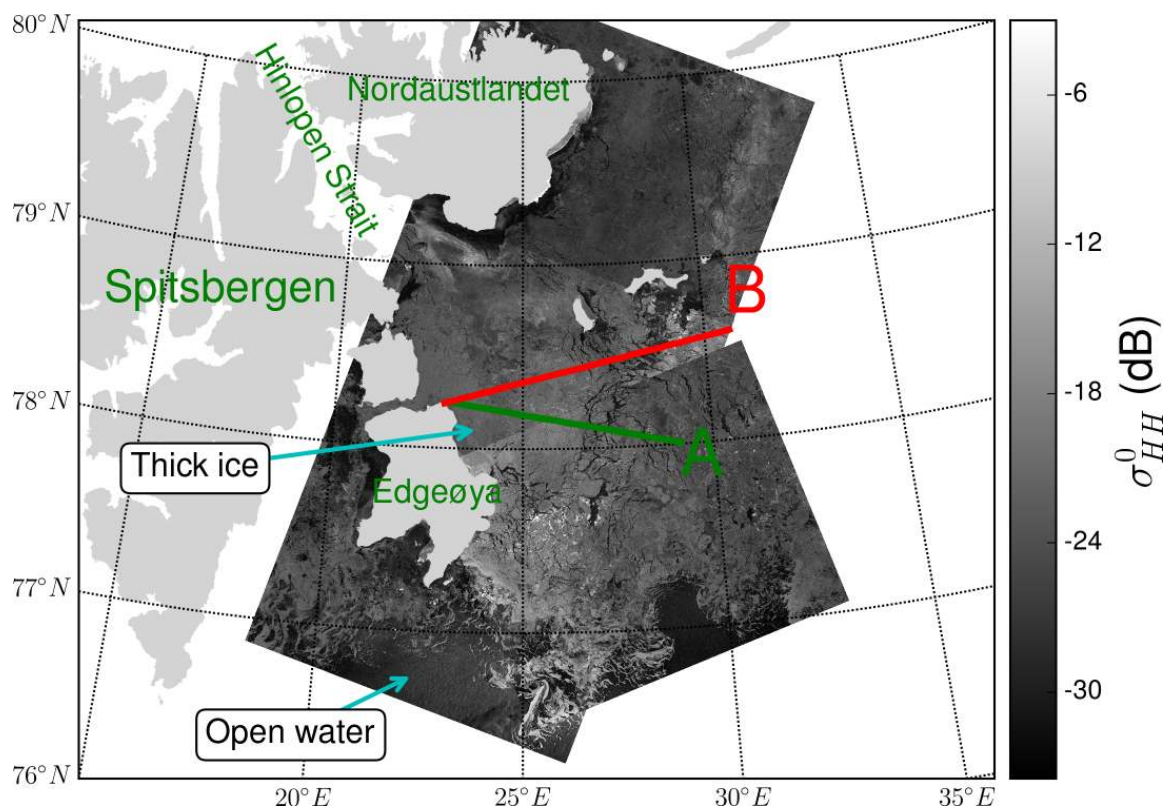


Figure 2.4: Sea ice conditions in the flights region on March 24. The TerraSAR-X wide swath mode (HH polarization), with frames taken at 05:35 UTC and 14:58 UTC. The aircraft tracks are marked in red - **A** at 10:05-10:41 UTC and **B** at 11:25-12:07 UTC .

and ice elevation with the accuracy and precision of 25 mm. During the flights it was operating with pulse repetition frequency of 50 kHz, measuring the surface elevation in cross track linear scan in the range of $\pm 30^\circ$. Such configuration at the flight altitude of 70 m resulted in across-track and along track sampling of 25 cm and 50 cm, respectively. The data was calibrated and georeferenced to the WGS84 datum. Further processing involved manual classification of tie points in leads to obtain local sea level and sea ice freeboard (Hendricks et al., 2014).

In this work, we use the pre-processed *ALS* data, described in the previous paragraph. The geo-referenced surface elevations are used to compute surface roughness statistics. The elevation data are interpolated to a regular $0.5 \text{ m} \times 0.5 \text{ m}$ grid to obtain a digital elevation model (*DEM*) of the sea ice surface. The *DEM* serves to derive surface slopes orientation.

The *ALS* freeboard data is used to estimate the sea ice thickness. The estimation method uses the principle of hydrostatic equilibrium. In order to derive the sea ice thickness, the densities of water and ice must be known, as well as the load of snow, described by snow density and snow thickness. Unfortunately, during the flights the snow radar was still in the test phase of development, therefore we decided not to use this data. In order to tackle the problem of lack of the snow thickness data, we follow Kaleschke et al. (2016) and assume an approximation formula used by Yu and Rothrock (1996) and Mäkynen et al. (2013), which sets the snow thickness to 10% of the sea ice thickness. As for the respective densities, we assume the water density as 1027 kg/m^3 , ice density 917 kg/m^3 after (Ricker et al., 2014b) and snow density 300 kg/m^3 after (Warren et al., 1999).

Figure 2.5 shows the sea ice thickness distributions obtained from *ALS* freeboard data during both flights. Both flights exhibit similar sea ice thickness distribution, with double maxima at ice thickness of 0.3 m and 1.4 m.

2.2.2 EMIRAD2 radiometer

Another vital instrument on board of the aircraft was the L-band radiometer - *EMIRAD2*. The EMIRAD-2 L-band radiometer, developed by DTU-Space, is a fully polarimetric system with advanced radio frequency interference (*RFI*) detection features (Søbjaerg et al., 2013). Two Potter horn antennas, one nadir pointing, one side looking at 40° incidence angle measure the radiation from the surface with a footprint of approximately 60 m for a 70 m flight altitude. The receiver has a sensitivity of 0.1 K for 1 s integration time. During all flight operations navigation data are collected and used to transform the polarimetric brightness temperature into the Earth reference frame (Hendricks et al., 2014)

The EMIRAD-2 data have been screened by evaluating kurtosis, polarimetric (Balling et al., 2012), and T_B anomalies, this revealed up to 30%

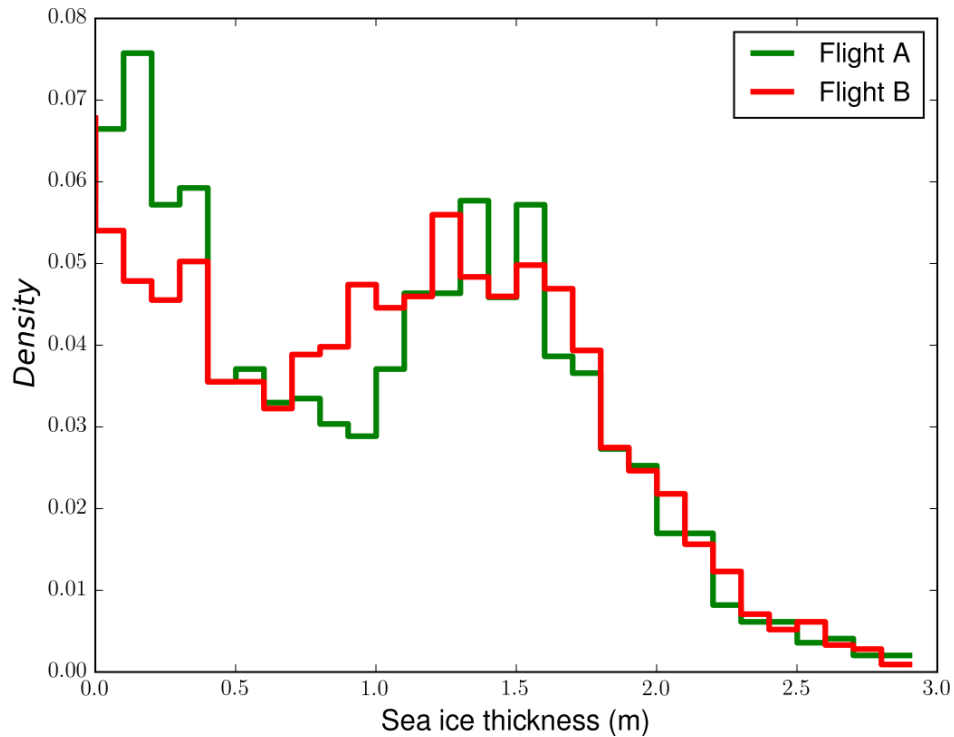


Figure 2.5: Histograms of sea ice thickness along flight **A** and **B** computed from *ALS* freeboard.

RFI contamination. When subtracting the mean value of the *RFI*-flagged data from the mean value of the full data a difference of typically a few K is present for side looking horn and typically 10K for the nadir looking horn. Data analysis further revealed a 20K offset relative to the nadir vertical channel caused by a continuous wave signal from the camera that was mounted on the airplane to obtain visual images. This contamination could not be detected by the *RFI* filters but the analysis concludes a purely additive characteristic and allowed a bias correction (Hendricks et al., 2014). In this study we use the data pre-processed by the DTU-team. The radiometer data was *RFI*-cleaned and bias-corrected and validated using aircraft wing wags and nose wags over open ocean (Hendricks et al., 2014).

The overview of the mentioned data set is presented in Figures 2.6 to 2.9. The one-second time resolution data are presented in light colors and the thirty-second averages in thick lines. For each flight there are two associated figures: the first presenting the nadir brightness temperatures, and the second presenting the brightness temperatures at 40° registered by a side looking antenna.

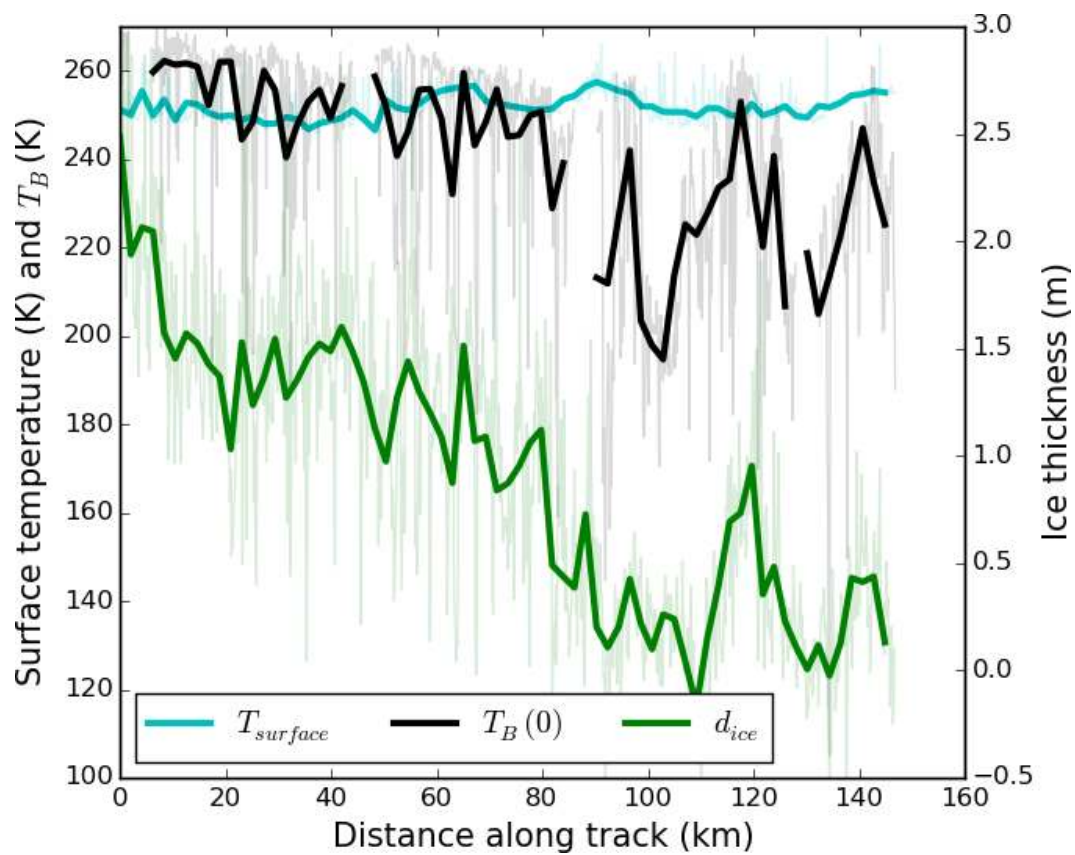


Figure 2.6: Flight **A**, **Nadir** antenna (zero kilometer marks the start of the track at the coast of Edgeøya). *Thin lines* show 1 s measurements, *thick lines* mark the 30 s averaged values. The sea ice thickness from *ALS* freeboard (d_{ice}) is marked in *green*, surface temperature registered by KT19 in *cyan* ($T_{surface}$) and nadir brightness temperature ($T_B(0)$) in *black*.

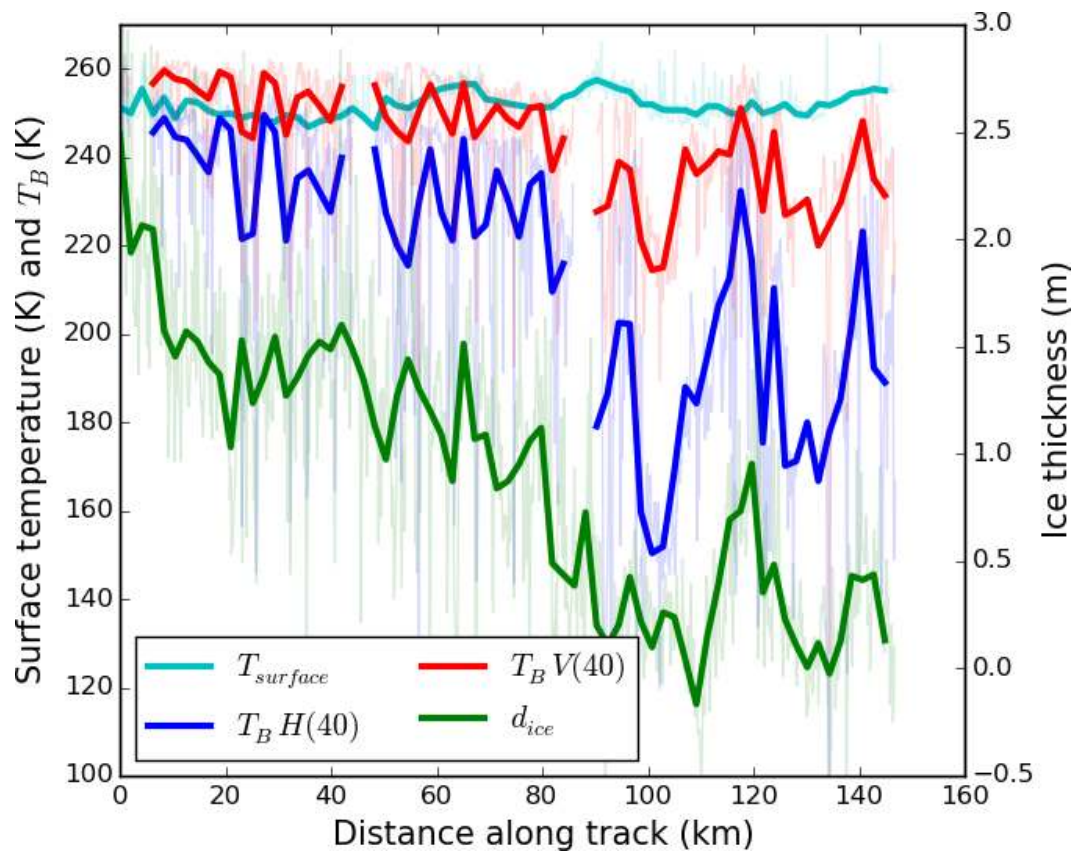


Figure 2.7: Flight **A**, **Side** antenna (zero kilometer marks the start of the track at the coast of Edgeøya). *Thin lines* show 1 s measurements, *thick lines* mark the 30 s averaged values. The sea ice thickness from *ALS* freeboard (d_{ice}) is marked in *green*, surface temperature registered by KT19 in *cyan* ($T_{surface}$) and brightness temperatures from side-looking antenna are marked in *blue* for horizontal polarization ($T_B(H, 40)$) and *red* for vertical polarization ($T_B(V, 40)$).

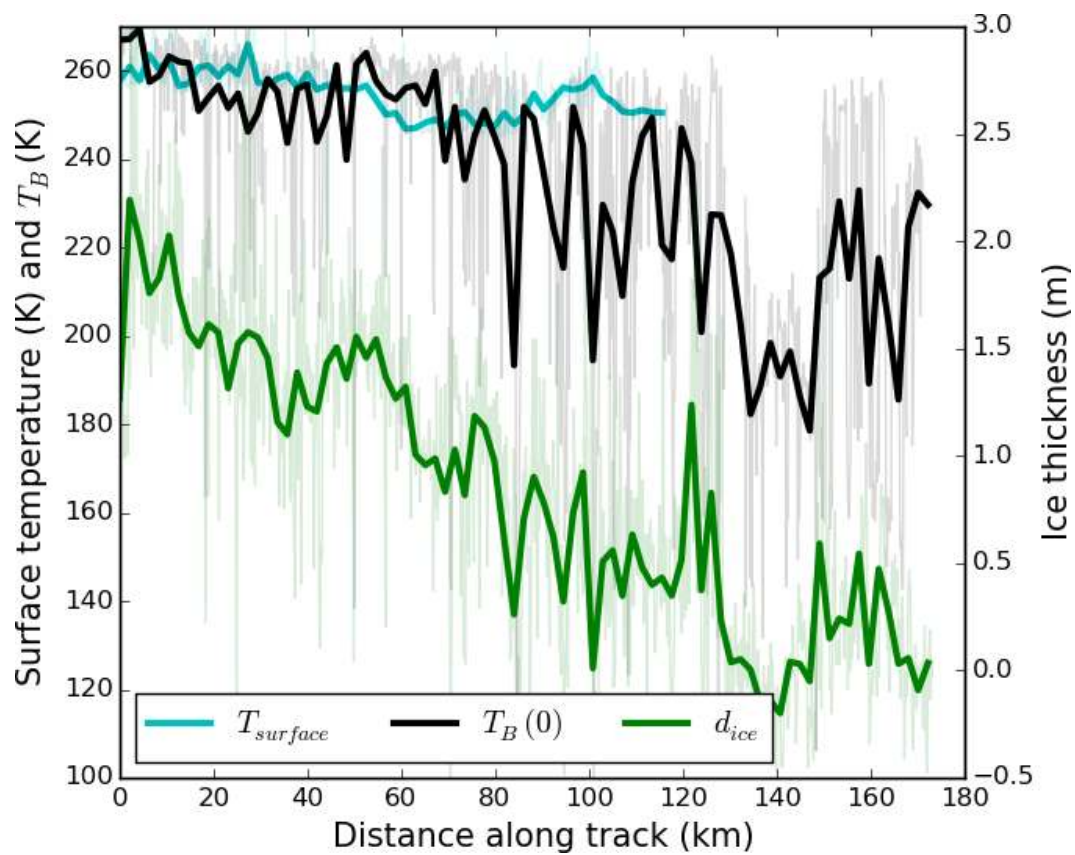


Figure 2.8: Flight **B**, **Nadir** antenna (zero kilometer marks the start of the track at the coast of Edgeøya). *Thin lines* show 1 s measurements, *thick lines* mark the 30 s averaged values. The sea ice thickness from *ALS* freeboard (d_{ice}) is marked in *green*, surface temperature registered by KT19 in *cyan* ($T_{surface}$) and nadir brightness temperature ($T_B(0)$) in *black*.

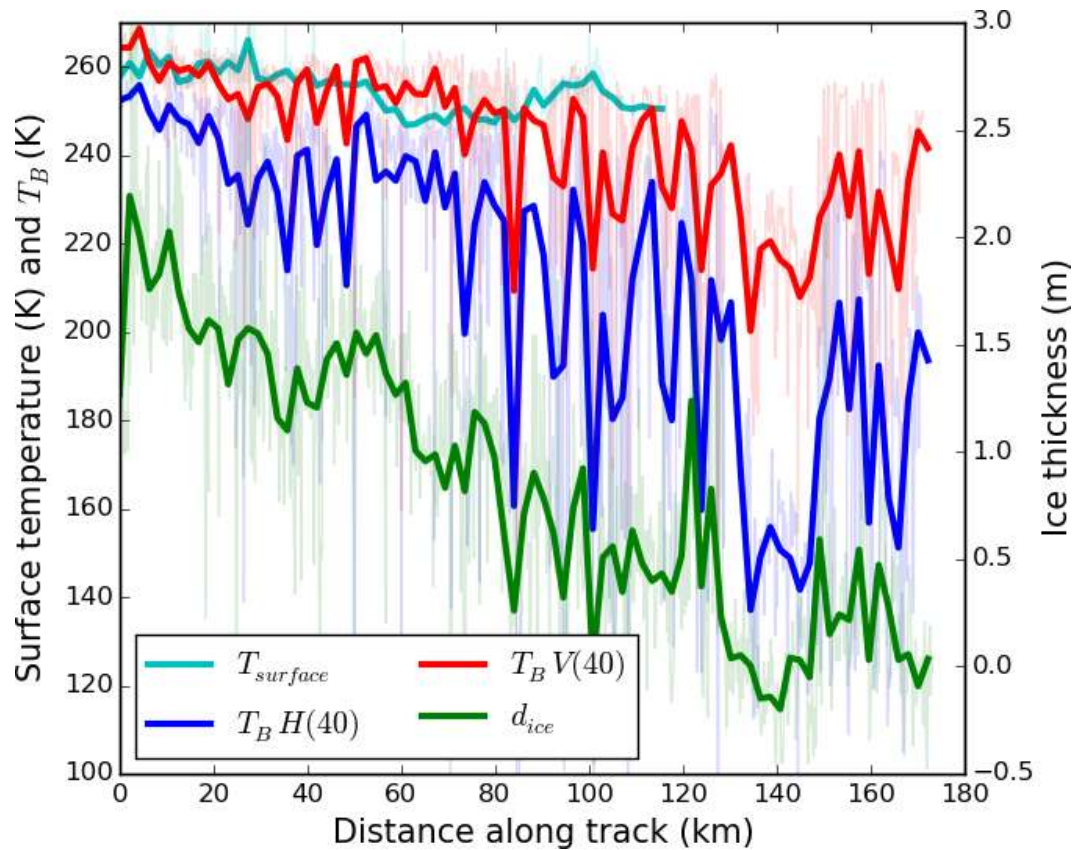


Figure 2.9: Flight **B**, **Side** antenna (zero kilometer marks the start of the track at the coast of Edgeøya). *Thin lines* show 1 s measurements, *Thick lines* mark the 30 s averaged values. The sea ice thickness from *ALS* freeboard (d_{ice}) is marked in *green*, surface temperature registered by KT19 in *cyan* ($T_{surface}$) and brightness temperatures from side-looking antenna are marked in *blue* for horizontal polarization ($T_B(H, 40)$) and *red* for vertical polarization ($T_B(V, 40)$).

Chapter 3

Methods

In this chapter we briefly introduce the basic concepts of microwave remote sensing used in this work. In sections 3.1 and 3.2 we present the theoretical background of microwave emissions. These concepts are implemented in the sea ice emission model presented in section 3.3. Then, in section 3.4 we proceed with an analysis of surface roughness and its role in microwave remote sensing. In section 3.5 we argue for geometrical optics as a suitable method for representing the sea ice surface roughness. Finally, in section 3.6 we connect the sea ice emission model with geometrical optics.

3.1 Brightness temperature

Every physical body emits energy in a form of electromagnetic radiation. The amount of radiation in specific frequency (f) for a perfectly emitting/absorbing “black body” is described by Planck law equation (3.1) (Ulaby et al., 2014, pp. 229-230):

$$I_f = \frac{2hf^3}{c^2} \left(\frac{1}{e^{hf/k_B T} - 1} \right), \quad (3.1)$$

where h is the Planck constant, k_B is the Boltzmann constant, c is the speed of light in vacuum and T is the physical temperature of the body. For the low microwave frequency ($f/T < 3.9 \times 10^8 \text{ Hz K}^{-1}$) an approximation called Rayleigh-Jeans law equation 3.2 can be used with deviation from original curve of less than 1% (Ulaby et al., 2014, pp. 231):

$$I_f \approx \frac{2k_B T}{\lambda^2}, \quad (3.2)$$

where λ denotes the electromagnetic wavelength and $\lambda = c/f$. Figure 3.1 shows two Planck functions corresponding to physical temperatures of 300 K (in black) and 6000 K (in red). The Rayleigh-Jeans’s approximation for $T = 300$ K is marked in black

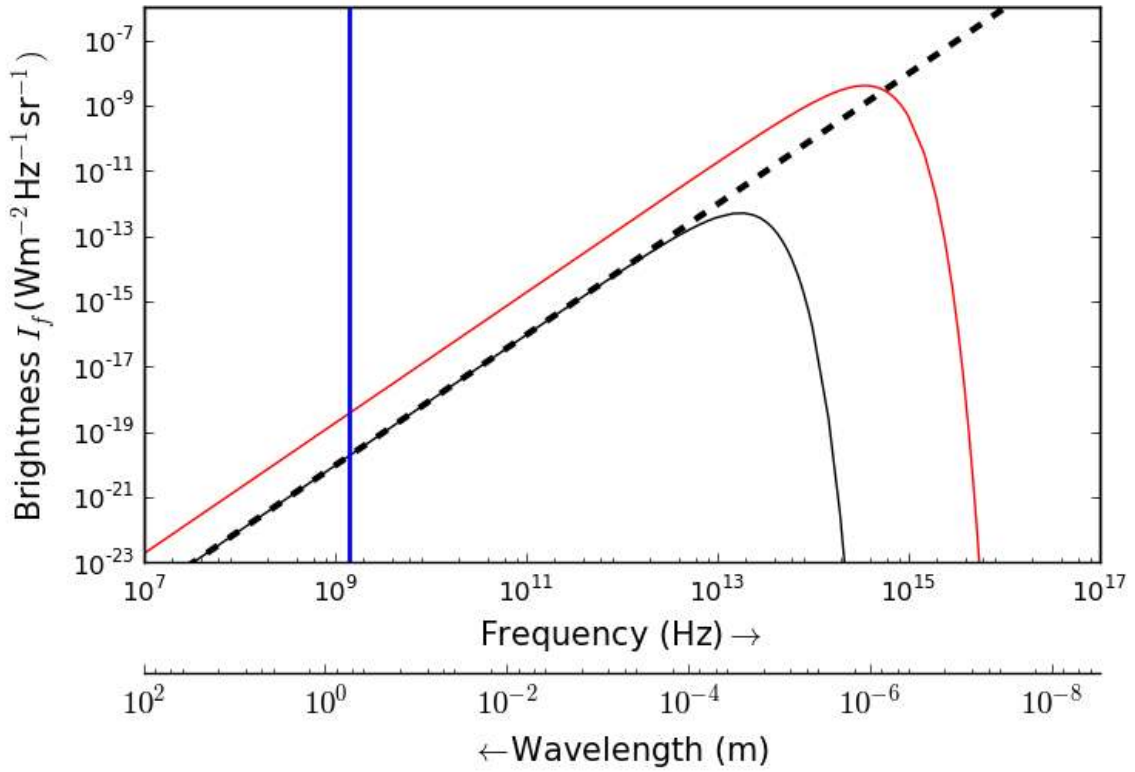


Figure 3.1: Planck curves for 300 K (*black solid line*) and 6000 K (*red solid line*). The Rayleigh-Jeans approximation is marked in *dashed line*. The L-band frequency of 1.4 GHz is marked by a blue vertical line.

dashed line. The frequency of 1.4 GHz, relevant for this study is denoted by a blue vertical line. In the microwave domain of the spectrum, where the Rayleigh-Jeans’s law holds well, physical temperature is a convenient measure of the body’s brightness, i.e. the amount of energy emitted at a given frequency. Hence, the brightness temperature (T_B) is a measure of emitted energy.

The “black body” is a theoretical concept that is an approximation for some real bodies. Nonetheless, the real physical bodies are not perfect absorbers/emitters (Schanda, 1986a, pp. 143-145). They emit less energy than a “black body” with the same physical temperature. The proportional ratio of the real body brightness to the theoretical ‘Black body’ is called the emissivity ($0 < e < 1$) and in general, depends on frequency, polarization and direction of the measurement (θ, ϕ):

$$e(\theta, \phi) = \frac{I}{I_{blackbody}} = \frac{T_B(\theta, \phi)}{T}. \quad (3.3)$$

The non-polarized radiation originating in the medium needs to cross the medium-air boundary to reach the antenna, where it is subsequently registered. When the electromagnetic wave is propagating across the boundary, the electric and magnetic fields must fulfill a set of continuity conditions for their horizontal and vertical

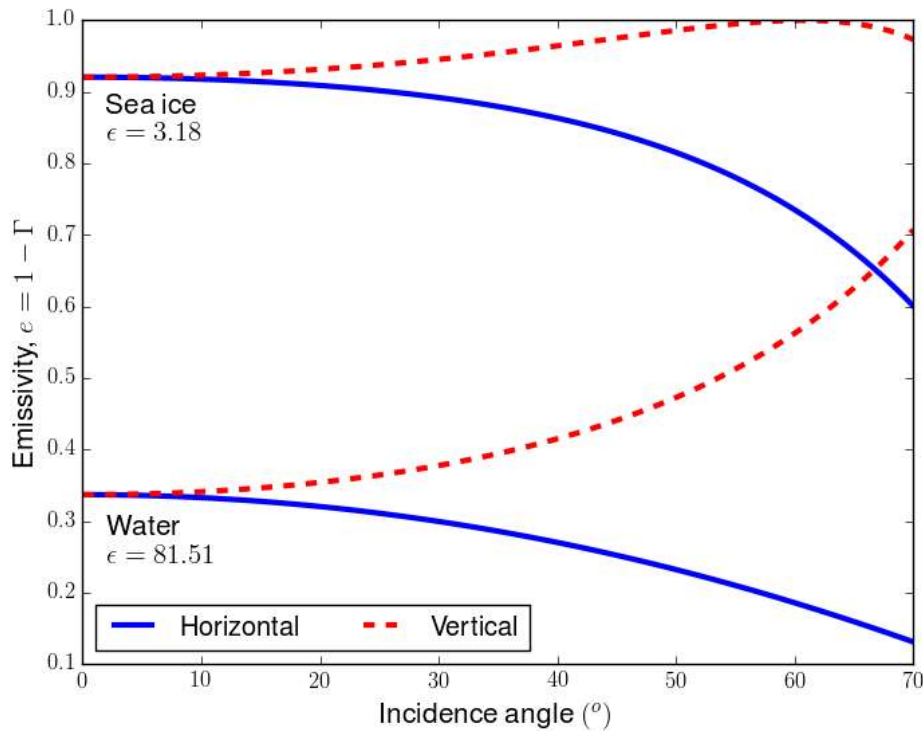


Figure 3.2: Emissivities calculated with Fresnel equations. Horizontal (H) polarization in *blue solid lines*, Vertical polarization (V) in *red dashed lines*. The L-band permittivities of ice ($\epsilon = 3.18$) and water ($\epsilon = 81.51$) cause the difference in calculated emissivities.

components (Jackson, 1975, pp. 278-282). As a result, the values of the brightness temperature observed above the surface depend on the polarization and the incidence angle (θ). Fresnel equations (3.4) describe the reflectivity (Γ^*) for horizontal (H) and vertical (V) polarization as a function of the incidence angle. Mind that Kirchhoff's law states that under thermodynamic equilibrium $e_p = 1 - \Gamma_p^*$ (Ulaby et al., 2014, pp. 253).

$$\Gamma_H^*(\theta_1) = \left| \frac{\sqrt{\epsilon_1} \cos \theta_1 - \sqrt{\epsilon_2} \cos \theta_2}{\sqrt{\epsilon_1} \cos \theta_1 + \sqrt{\epsilon_2} \cos \theta_2} \right|^2, \quad \Gamma_V^*(\theta_1) = \left| \frac{\sqrt{\epsilon_1} \cos \theta_2 - \sqrt{\epsilon_2} \cos \theta_1}{\sqrt{\epsilon_1} \cos \theta_2 + \sqrt{\epsilon_2} \cos \theta_1} \right|^2 \quad (3.4)$$

where $\epsilon_{1/2}$ denotes the permittivities of the respective medium. The Snell law (equation 3.5) relates the respective angles (Ulaby et al., 2014, pp. 248).

$$\sqrt{\epsilon_1} \sin \theta_1 = \sqrt{\epsilon_2} \sin \theta_2 \quad (3.5)$$

Figure 3.2 shows two examples of the angular dependence of the emissivities of ice with $\epsilon = 3.18$ (temperature 263 K, and bulk salinity 1 g/kg for frequency 1.4 GHz, values corresponding to thick multi year ice) and water with $\epsilon = 81.51$ (temperature 273 K and salinity 20 g/kg for frequency 1.4 GHz) calculated with Fresnel equations 3.4.

The complex permittivity constant $\bar{\epsilon}$ comprises of the real term ϵ , characterizing the reaction of the medium to the applied electric field and the imaginary part κ characterizing the attenuation of the electric field in the medium:

$$\bar{\epsilon} = \epsilon + i\kappa \quad (3.6)$$

3.2 Brightness temperature over sea ice

Sea ice forms on the ocean surface as a result of a net heat flux between warm water (≈ 273 K) and cold air (≈ 253 K). When water cools to its critical temperature (depending on its salinity), the ice crystals start to form, expelling the salts from its structure. Some of the salts precipitate into the water below, yet part of them are trapped dissolved in the so-called brine pockets surrounded by the crystalline H_2O structure. The salt content and brine volume influence the complex permittivity of ice. As ice gets thicker it isolates the ocean from the atmosphere, restoring the thermal equilibrium by adjusting the heat flux. This leads to a temperature gradient within the ice (Maykut G., 1971).

The ice is not isothermal and its permittivity varies with depth and temperature (Vant et al., 1978; Cox and Weeks, 1982). Furthermore, the absorption (κ) of radiation at 1.4 GHz in sea ice is weak (Carsey, 1992, pp. 63; Ulaby et al., 2014, pp. 139). As a result, the T_B s emitted by layers with different temperature and emissivity/absorptivity are contributing to the T_B measured at the surface. Thus, the T_B is described by the following radiative transfer equation (Ulaby et al., 2014, pp. 245):

$$T_B(\theta; Z) = T_B(\theta, 0)e^{-\tau(0,Z)} + \int_0^Z \kappa_a(z')T(z') \sec \theta e^{-\tau(z',Z)} dz', \quad (3.7)$$

where $\tau(z_1, z_2) = \int_{z_1}^{z_2} \kappa_a \sec \theta dz'$ is called the optical depth and κ_a is the absorption coefficient of the ice. In equation 3.7 the extinction of radiation caused by volume scattering is neglected. This is due to the fact that usual scattering centers within the ice such as air bubbles and brine pockets, have much smaller dimensions than the wavelength at our frequency of interest (Obbard et al., 2009; Ulaby et al., 2014, pp. 461)

The measurements of T_B over ice need to take into account also other factors. The Earth's atmosphere also emits and absorbs radiation. The upwelling brightness temperature observed over sea ice at the top of the atmosphere (*TOA*) (eq. 3.8), at polarization p and incidence angle θ consists of several elements. This comprises ice

component (T_{Bice}), contributions from the atmosphere ($T_{B atm}$) and cosmic emissions ($T_{B cosm}$).

$$T_{B,TOA} = k_{atm} \cdot T_{B,ice} + k_{atm}(1 - e_{ice})T_{B,atm} + 2k_{atm}(1 - e_{ice}) \cdot T_{B,sky} + T_{B,atm} \quad (3.8)$$

where k_{atm} is the atmospheric attenuation, $T_{B,atm}$ is the emission from the atmosphere and $T_{B,cosm}$ are the cosmic emissions. Depending on the antenna's height, we have to include the atmosphere's emissions reflected from the sea ice surface and the emissions from the portion of atmosphere between the antenna and the surface. The influence of the atmosphere on the L-band T_B can be parametrized by surface values of pressure, temperature and water vapor density (Zine et al., 2008)

The sky emissions is a broad term which aims at describing all emissions coming from beyond the Earth's atmosphere, including the cosmic background radiation, the galactic noise and the emissions from other celestial bodies. All these factors, apart from the cosmic background radiation, vary with geographical location and seasons (Vine and Abraham, 2004). Since an analysis of these factors lies beyond the scope of this work, we consider T_{Bsky} to be identical to cosmic background radiation of 2.7 K (Le Vine et al., 2005; Peng et al., 2013)

3.3 Sea ice emission model

For the simulation of sea ice brightness temperature ($T_{B,ice}$) we use the **MI**crowwave **L**-band **LA**yered **SA**ea ice emission model described by Maaß et al. (2013), further referred to as *MILLAS*. This model is based on the radiative transfer model of Burke et al. (1979)(who used it for soils), with infinite half-space of sea water covered with layers of sea ice, snow and top semi-infinite layer of air. In contrast to the original model of Burke et al. (1979) and its usage by Maaß et al. (2013), the current version of *MILLAS* takes into account multiple reflections at the layer boundaries. The *MILLAS* model describes the brightness temperature above snow-covered sea ice as a function of temperature and permittivity of the layers. The water permittivity depends mainly on the water temperature and salinity (Klein and Swift, 1977). Ice permittivity can be approximately described as a function of brine volume fraction (Vant et al., 1978), which depends on ice salinity and the densities of the ice and brine (Cox and Weeks, 1982), which in turn depend mainly on ice temperature. The permittivity of dry snow can be estimated from its density and temperature (Tiuri et al., 1984). In the simulation setup the ice and water salinity are kept constant. Furthermore, we assume that the system is in thermal equilibrium, and the water beneath the ice is at freezing point. In this configuration the T_B is simulated as a function of ice thickness (d_{ice}), snow thickness (d_{snow}) and surface temperature (T_{surf}). In our setup the snow is assumed to be dry with density of 300 kg/m^3 , which is the average snow density value for December

Parameter		Value
Snow	surface temperature	measured (KT19)
	snow wetness	0%
	snow density	300 kg/m ³
	snow thermal conductivity	0.31 W/(mK)
Ice	ice thermal conductivity	$2.034 \text{ W/(mK)} + 0.13 \text{ W/m} \cdot S_{ice}(\text{g/kg})/T_{ice}(\text{K})$
	ice salinity	4 g/kg
Water	water salinity	33 g/kg
	water temperature	271.2 K

Table 3.1: Brightness temperature simulation setup of the **MI**crowave **L**-band **LA**yered **Sea** ice emission model (*MILLAS*).

Arctic measurements from 1954-91 (Warren et al., 1999). The T_B simulations are only slightly sensitive to snow density, see fig 3 in Maaß et al. (2013). The permittivities of snow and ice are linked to their temperature. The temperature profiles within snow and ice are assumed to be continuous and linear. The values for the ice and snow thermal conductivity are taken from Yu and Rothrock (1996); Untersteiner (1964), shown in table 3.1. Figure 3.3 illustrates the temperature and permittivity profiles computed with *MILLAS* for input values: $T_{surf} = 260 \text{ K}$, $d_{snow} = 0.15 \text{ m}$, $d_{ice} = 1.35 \text{ m}$. Presented setup involves 20 layers within the ice.

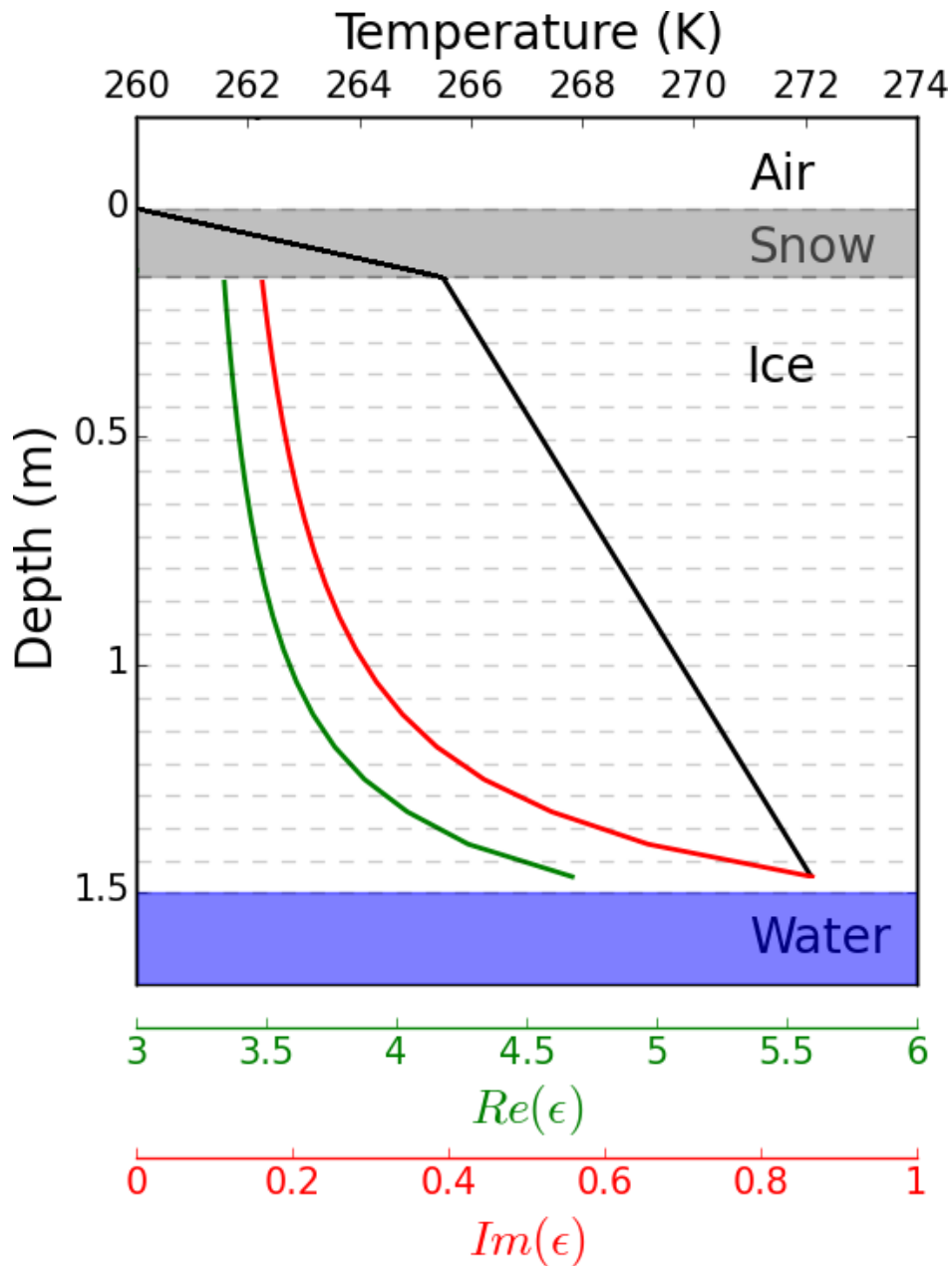


Figure 3.3: An example of temperature (*black*) and permittivity (*green* and *red*) profiles calculated with multilayer setup of *MILLAS*. The snow permittivity $\epsilon_{snow} \approx 1.5 + 0.001i$ is not visible at this axis scale. Input values: $T_{surf} = 260$ K, $d_{snow} = 0.15$ m, $d_{ice} = 1.35$ m.

3.4 Surface roughness

Surface roughness (or simply roughness) describes the interface between two media. It is quantified by the deviation of the local normal vector from the normal vector of the plane approximation of a larger region. There are multiple possibilities to quantify the roughness. The most common is computing the standard deviation of surface height (σ_z) (Ulaby et al., 2014, pp. 422). Higher statistical moments and root mean square slope (m_{ss}) are also used (Dierking, 2000). A random surface is a surface that cannot be described by an analytical function. Such a surface can be characterized by the distribution of surface heights and the spatial correlation function $R(\xi)$ (Ulaby et al., 2014, pp. 422). Commonly the surface height distribution is assumed to be Gaussian, and the correlation function either Gaussian or exponential as shown by equation (3.9).

$$R(\xi) = \exp\left(-\left(\frac{\xi}{l_C}\right)^n\right), \quad (3.9)$$

where $n = 1$ for an exponential and $n = 2$ for a Gaussian correlation function, l_C is the correlation length and ξ is the displacement distance. Considering the above, random surface roughness can be characterized by statistical properties σ_z and $R(\xi)$. The σ_z is measure of roughness vertical scale, whereas horizontal scale is characterized by the l_C .

3.4.1 Impact on surface reflectivity

The reflectivity of a rough surface (Γ_p) can be described as the integral of the bi-static scattering coefficient (σ_{pq}^0) over the upper half-space as shown in eq. 3.10 (Ulaby et al., 2014, pp. 252), where p and q stand for polarization H/V .

$$\Gamma_p(\theta_i, \phi_i) = \frac{1}{4\pi \cos \theta_i} \int_0^{2\pi} \int_0^{\pi/2} [\sigma_{pp}^0(\theta_i, \phi_i; \theta_s, \phi_s) + \sigma_{pq}^0(\theta_i, \phi_i; \theta_s, \phi_s)] \sin \theta_s d\theta_s d\phi_s \quad (3.10)$$

Generally, the σ_{pq}^0 are complex functions of the medium dielectric properties, direction of incidence (θ_i, ϕ_i), direction of scattering (θ_s, ϕ_s), as well as the surface roughness characterized by σ_z and $R(\xi)$. The equation 3.10 can be also expressed as a sum of the reflectivity along the specular direction and all other directions:

$$\Gamma_p = \Gamma_p^* e^{-4\psi^2} + \Gamma_{diff,p}, \quad (3.11)$$

where the first term in the sum is called the coherent component, with $\psi = \frac{2\pi}{\lambda} \sigma_z \cos \theta_i$, and the second term is called the diffusive component (Ulaby et al., 2014, pp. 197). The coherent component exists only along the specular direction. Figure 3.4

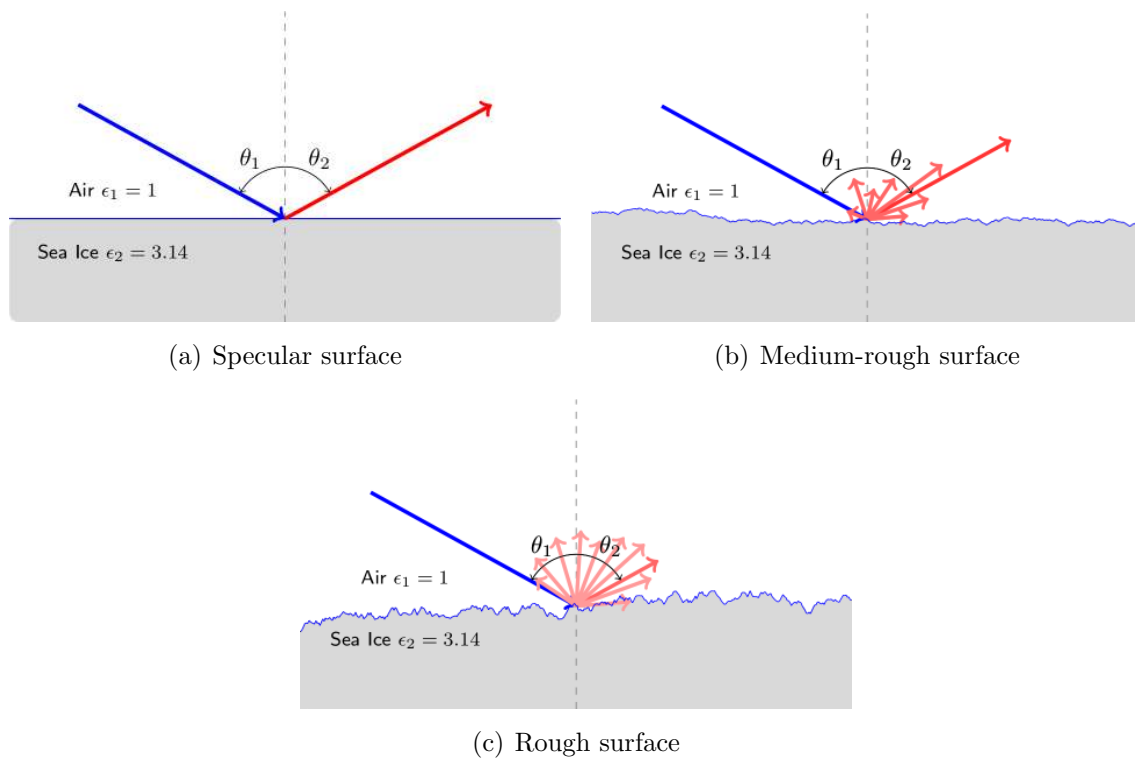


Figure 3.4: Surface scattering from surfaces with different degree of roughness: a) specular, b) medium-rough, c) rough. Adapted from Ulaby et al. (2014, pp. 252)

illustrates that with increasing σ_z the coherent component decreases and more radiation is scattered in a diffused manner.

Just like the reflectivity is influenced by the surface roughness, the transmissivity and the emissivity are also affected. Due to the roughness the refraction and emissions are no longer following the specular directions, as the Snell law would predict. Figure 3.5 shows a conceptual sketch of these processes.

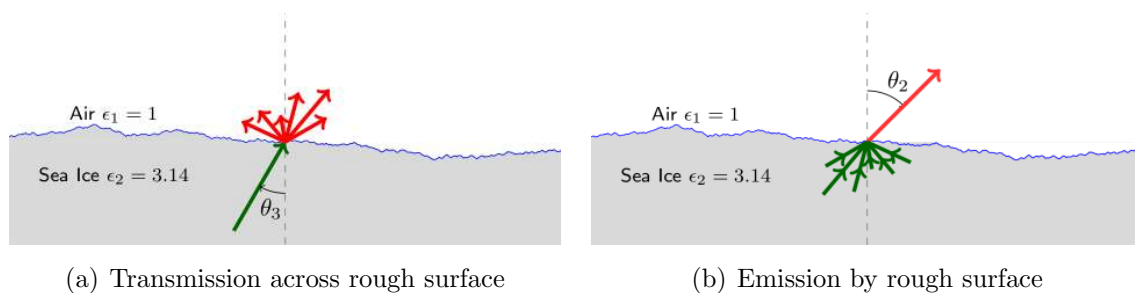


Figure 3.5: A Single beam transmitted through a rough surface results in a pattern of radiation in the upper medium. Similarly, the emissions from the rough surface originate from many directions. Adapted from (Ulaby et al., 2014, pp. 252)

3.4.2 Semi-empirical roughness model for surface reflectivity

The increase in surface roughness has two effects on the reflectivity. According to equations 3.10 and 3.11, it causes a decrease in coherent component and an increase in polarization mixing. These effects of the roughness are the foundation of the semi-empirical roughness model introduced by Wang and Choudhury (1981), hereinafter referred to as the *HQ – model*. The model (eq. 3.12) uses four parameters (H_R , Q_R , N_{Rp} , N_{Rq}) to relate the smooth and rough surface reflectivities at a given incidence angle θ and polarization p :

$$\Gamma_p = [(1 - Q_R)\Gamma_p^* + Q_R\Gamma_q^*] \exp(-H_R \cos^{N_{Rp}} \theta). \quad (3.12)$$

The H_R is related to the roughness vertical scale σ_z , in a similar way as ψ in equation 3.11. The Q_R is a polarization mixing parameter and $N_{Rp/q}$ parameters are accounting for the changes in angular dependency of $\Gamma_{p/q}$.

Commonly, to relate these four parameters to surface roughness, empirical relations are used (Wigneron et al., 2011; Lawrence et al., 2013). However, the *HQ – model* and the mentioned relations were developed for soil-related applications. The different permittivities and roughness scales of the sea ice, make these relations inappropriate for the sea ice reflectivity modeling. We present a new parametrization suitable for the sea ice applications in chapter 5.

3.4.3 Rough surface scattering models

Surface reflectivity can be expressed in terms of bi-static scattering coefficients (σ_{pq}^0) as shown in eq. 3.10. The development of mathematical models connecting the statistical parameters of random roughness (σ_z , l_C) with σ_{pq}^0 resulted in three scattering models, described below. The applicability of the scattering models depends on the horizontal and vertical roughness scales with respect to the incident wavelength (λ).

Small Perturbation Model

The small perturbation model was developed by Rice (1951) to calculate scattering coefficients of a slightly rough surface. The model is applicable for surfaces with mean-square slope less than 0.3 and with both the σ_z and the l_C are much smaller than the incident wavelength. These conditions are expressed as follows: $mss < 0.3$ and $k\sigma_z < 0.3$ and $kl_C < 0.3$, where $k = 2\pi/\lambda$ is the wave number of the incident wave.

Kirchoff Models

An approximation known as the Kirchoff scattering model was developed by Beckmann and Spizzichino (1963). This approximation is applicable for surfaces with horizontal roughness scales greater than σ_z . That means $l_c > \lambda$, $l_c^2 > 2.76 \cdot \sigma_z \lambda$.

This method has two variants depending on the vertical roughness scale. The first variant, is the stationary phase approximation or **geometrical optics** (*GO*). Geometrical Optics approximation is applicable for surfaces with large σ_z , with $\sigma_z \cos \theta_0 / \lambda > 0.25$. The second variant is the scalar approximation or **physical optics**. This approximation is suitable for surfaces with smaller vertical roughness scale expressed in terms of mean-square slope: $mss < 0.25$.

I2EM Model

The small perturbation model and the Kirchoff models have their respective domains of applicability. The model developed by Fung et al. (2002) is not constrained to specific horizontal and vertical roughness scale. This so-called *I2EM* model allows for computation of σ_{pq}^0 with contributions from multiple scattering and inclusion of shadowing.

3.5 Sea ice roughness

As indicated in section 3.4, the σ_z and the l_C are describing the vertical and horizontal roughness scales. These parameters need to be considered in the context of the local reference plane. The plane is an approximation of a surface at a given scale L . It is often the case for natural surfaces that several roughness scales are super-imposed, as illustrated in figure 3.6. Surface scattering occurs differently at each scale and therefore the selection of the domain size L has an influence on the σ_z and l_C (Mattia and Le Toan, 1999; Landy et al., 2015).

One way of dealing with multiple-scale roughness is to treat it as a random stationary process and apply the Wiener–Khinchin theorem to obtain the normalized auto-correlation function from the power spectrum of the surface profile (Dierking, 2000; Rivas et al., 2006). Then the calculation is limited by the maximum sampling frequency ($f_{max} = 1/(2\Delta x)$), calculated from sampling distance Δx and minimum ($f_{min} = 1/L$) sampling frequency. The resulting values are the band-limited roughness parameters σ_{bl} , l_{bl} . The power spectrum is crucial for analytical calculation of the surface scattering coefficients (σ_{pq}^0) and reflectivities.

Another option is based on the assumption that the roughness profile can be described as small ripples super-imposed over large-scale topography. Recent measurements of sea ice roughness with terrestrial lidar show that after high-pass

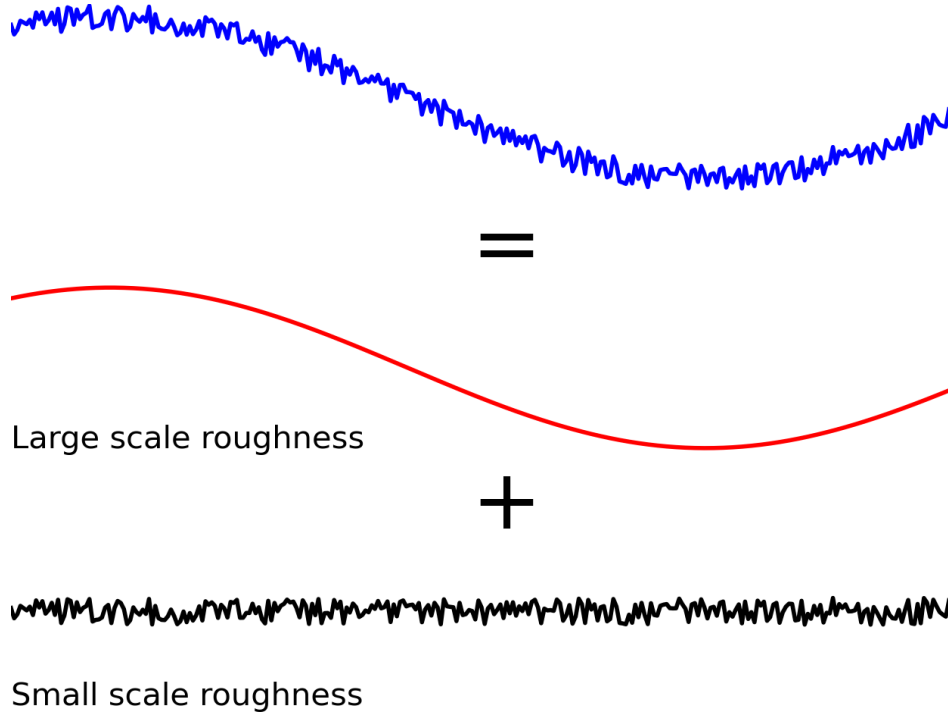


Figure 3.6: Illustration of the decomposition of the surface roughness into large scale and small scale roughness.

filtering (cut off at 0.25 m) the σ_z for different ice types, ranges from 0.16 to 0.64 cm (Landy et al., 2015). These results indicate that according to the Fraunhofer criterion (eq. 3.13), most sea ice types (except artificially grown frost flowers) can be treated as electromagnetically smooth surface for L-band radiation.

$$\sigma_z < \frac{\lambda}{32 \cos \theta_0}, \quad (3.13)$$

where θ_0 is the incidence angle.

Figure 3.7 shows the regions of validity of scattering approximations. The Fraunhofer criterion for incidence angles 0° and 60° are marked in dotted and dashed lines. The dots mark the lidar roughness measurements: in green over natural sea ice, in red over artificially grown ice (Landy et al., 2015).

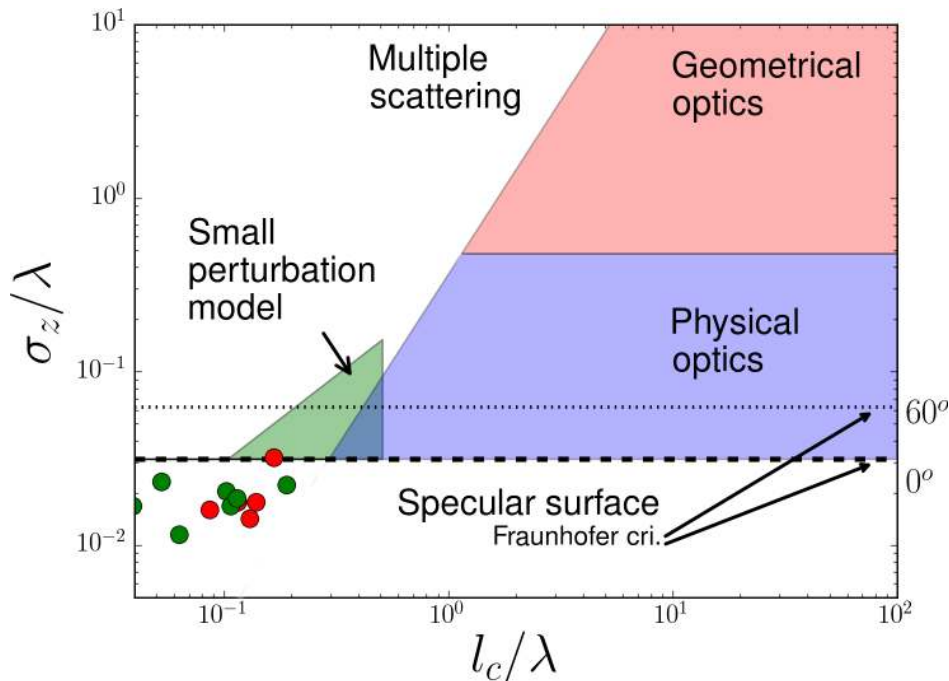


Figure 3.7: Scattering approximations and their applicability domains for $\lambda = 0.21$ m. The Fraunhofer smoothness criterion for $\theta_0 = 0^\circ$ and 60° marked in *dashed* and *dotted* line, respectively. Dots mark the results of surface roughness measurements made by Landy et al. (2015), in *green* over natural sea ice, in *red* over artificially grown ice.

We assumed that at the scale of 0.25 m sea ice is electromagnetically smooth, meaning that $\Gamma^* = \Gamma$. The large scale roughness is represented as a set of specular surfaces, the facets. The radiation is following the paths described by Fresnel and Snell equations (eq. 3.4 3.5). The large scale roughness changes the local incidence angle. such an approach is called the Geometrical Optics Approximation (Ulaby et al., 2014; Schanda, 1986b).

An analytical formula for the T_B of periodically undulating surface was shown by Wang et al. (1980). In this work we consider a surface consisting of multiple randomly oriented facets. First steps of our derivation, consist of the analysis of the coordinate systems associated with the radiometer and a local surface (Ulaby et al., 2014, pp. 564-567).

The radiometer antenna is placed over the center of the XY plane in global Cartesian coordinates $(\hat{x}, \hat{y}, \hat{z})$. The antenna look-direction is denoted by \hat{r} , and is described by the incidence angle θ_0 and the antenna azimuthal angle ϕ_0 (We consider a coordinate system with $\phi_0 = 0$):

$$\hat{r} = \hat{x}\sin(\theta_0)\cos(\phi_0) + \hat{y}\sin(\theta_0)\sin(\phi_0) - \hat{z}\cos(\theta_0). \quad (3.14)$$

The facet orientation is described by two angles: the local slope α and the facet azimuthal angle γ . Each facet has a local coordinate system $(\hat{x}', \hat{y}', \hat{z}')$, with local

normal vector $\hat{\mathbf{n}}'$, whose orientation in the global reference frame is described by:

$$\hat{\mathbf{n}}' = -\hat{\mathbf{x}}\sin(\alpha)\cos(\gamma) - \hat{\mathbf{y}}\sin(\gamma)\sin(\alpha) + \hat{\mathbf{z}}\cos(\alpha). \quad (3.15)$$

Therefore:

$$\hat{\mathbf{z}}' = \hat{\mathbf{n}}, \quad \hat{\mathbf{y}}' = \frac{\hat{\mathbf{n}} \times \hat{\mathbf{r}}}{|\hat{\mathbf{n}} \times \hat{\mathbf{r}}|}, \quad \hat{\mathbf{x}}' = \hat{\mathbf{y}}' \times \hat{\mathbf{z}}' \quad (3.16a,b,c)$$

Each facet has a local horizontal and vertical polarization coordinates $(\hat{\mathbf{h}}', \hat{\mathbf{v}}')$, which are rotated with respect to the horizontal and vertical vectors defined in the global reference frame $(\hat{\mathbf{h}}, \hat{\mathbf{v}})$:

$$\hat{\mathbf{h}}' = \hat{\mathbf{y}}' \quad (3.17a)$$

$$\hat{\mathbf{v}}' = -\hat{\mathbf{x}}'\cos\theta' - \hat{\mathbf{z}}'\sin\theta' \quad (3.17b)$$

$$\hat{\mathbf{h}} = -\hat{\mathbf{x}}\sin\gamma + \hat{\mathbf{y}}\cos\gamma \quad (3.17c)$$

$$\hat{\mathbf{v}} = -\hat{\mathbf{x}}\cos\theta_0\cos\gamma - \hat{\mathbf{y}}\cos\theta_0\sin\gamma - \hat{\mathbf{z}}\sin\theta_0 \quad (3.17d)$$

The facet orientation in relation to the antenna look-angle results in local incidence angle θ' :

$$\theta' = \cos^{-1}(-\hat{\mathbf{r}} \cdot \hat{\mathbf{n}}'). \quad (3.18)$$

Shadowing occurs when the local incidence angle $\theta' > \pi/2$, see figure 3.8, meaning that the facet is facing away from the radiometer. Such a facet is not contributing to the radiation registered by the radiometer. Our simulations do not include multiple reflections.

When calculating the T_{Bi} contribution originating from the i -th facet at the antenna aperture, the polarization rotation must be taken into account:

$$T_{Bi}(\theta'_i; H) = (\hat{\mathbf{h}} \cdot \hat{\mathbf{h}}'_i)^2 T_B^*(\theta'_i; H) + (\hat{\mathbf{h}} \cdot \hat{\mathbf{v}}'_i)^2 T_B^*(\theta'_i; V) \quad (3.19a)$$

$$T_{Bi}(\theta'_i; V) = (\hat{\mathbf{v}} \cdot \hat{\mathbf{h}}'_i)^2 T_B^*(\theta'_i; H) + (\hat{\mathbf{v}} \cdot \hat{\mathbf{v}}'_i)^2 T_B^*(\theta'_i; V) \quad (3.19b)$$

where $T_B^*(\theta'_i, p)$ is the brightness temperature originating from the i -th facet. For a visible facet ($\theta'_i < \pi/2$), the corresponding solid angle under it is observed is expressed by eq. 3.20.

$$\Omega_i = \frac{A \cos\theta'_i}{R^2 \cos\alpha_i}, \quad (3.20)$$

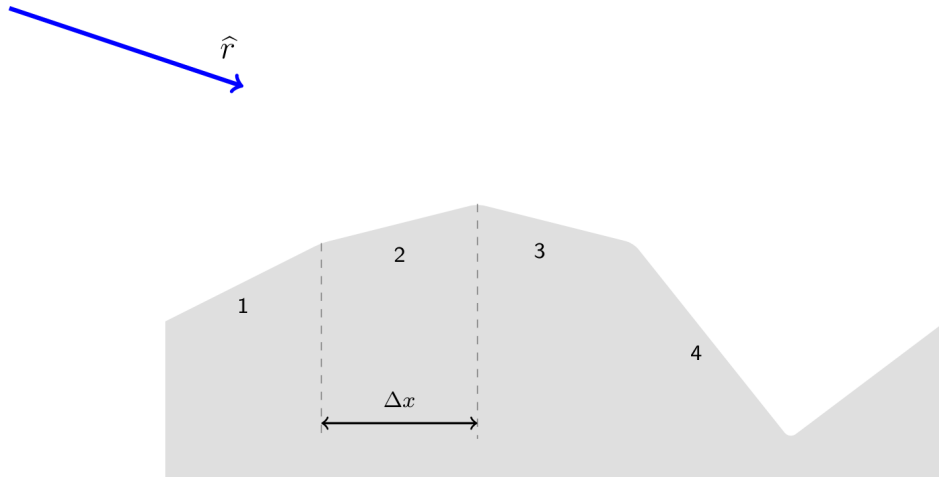


Figure 3.8: Schematic view of the faceted surface. The radiometer look direction \hat{r} is marked in *blue*. The sampling interval Δx is mark by arrow-span. The radiometer sees facets 1-3 under different local incidence angle. Facet 4 faces away from the radiometer, in this case shadowing occurs.

where A is the surface area of the facet. The sum over the entire antenna footprint consisting of N facets, with corresponding antenna gain ω_i , results in:

$$T_B(p; \theta_0) = \frac{1}{N \cos(\theta_0)} \sum_{i=1}^N w_i T_{Bi}(p; \theta'_i) \Omega_i \quad (3.21)$$

Assuming that the antenna gain function is constant across the footprint and radiometer is situated in the far field, so the θ_0 and \hat{r} can be considered constant across the antenna footprint, therefore:

$$T_B(p; \theta_0) = \frac{1}{N \cos(\theta_0)} \sum_{i=1}^N T_{Bi}(p; \theta'_i) \sec(\alpha_i) (-\hat{r} \cdot \hat{\mathbf{n}}_i) \quad (3.22)$$

3.6 Merging the geometrical optics with the radiation model

In the previous section the equation describing the brightness temperature of the faceted surface was introduced. It was assumed that the antenna is in a far field and the antenna gain function is constant across the footprint. The emissions from individual facets are described by the *MILLAS* model. The summation over the N facets requires knowledge about their orientation in space (α_i, γ_i) and with respect to the antenna looking-angle. Including N pairs of angles in eq 3.22 is possible, however impractical. Instead, we describe the surface topography with the probability distribution functions

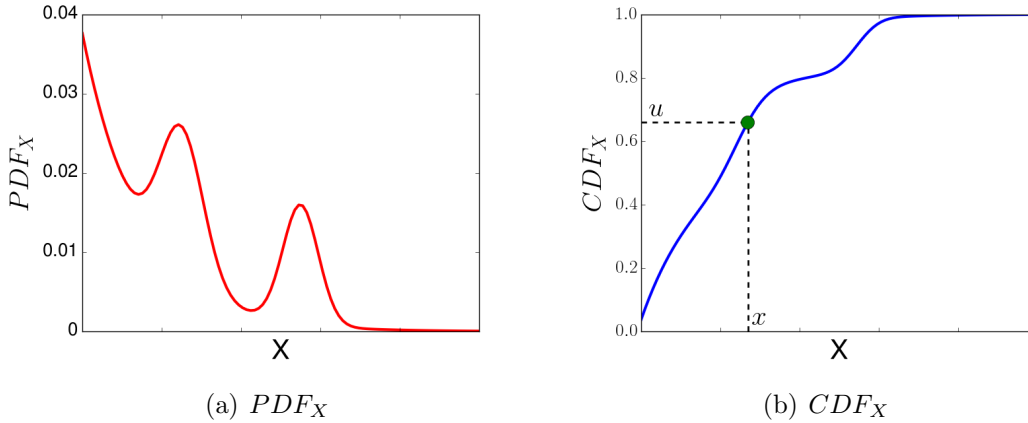


Figure 3.9: Conceptual sketch illustrating the inverse transform sampling method. u is a random number drawn from a uniform distribution $[0,1]$, then we invert the CDF_X so that $CDF_X^{-1}(u) = x$

of its slopes (PDF_α) and of slopes azimuths (PDF_γ). We calculate the cumulative distribution function of the facet slopes (CDF_α) from the PDF_α . Subsequently, the inverse transform sampling (*ITS*) is used to compute the facet orientation (Devroye, 2006) based on the CDF_α . Figure 3.9 illustrates the *ITS* concept.

In the inverse transform sampling method we assume that X is a continuous random variable with cumulative distribution function CDF_X . We obtain a population of x_i values drawn from the distribution described by CDF_X in three steps. First, we generate a random number u from a uniform distribution $[0, 1]$. Secondly, we look for a point that satisfies the condition $CDF_X(x) = u$. Finally, the algorithm returns the x , a random number from non-uniform distribution.

3.7 Summary

In this chapter we have presented the emission model that we use to simulate the brightness temperature (T_B) of the sea ice. As input parameters we use surface temperature and ice thickness. As the main purpose of this work is to investigate the surface roughness, for further studies we use a simplified setup of the *MILLAS* with one layer of snow on top of a one layer of ice, for the T_B simulations. We have presented arguments for neglecting the “small scale” roughness and using the geometrical optics approximation. At scales of 0.25 m sea ice is electromagnetically smooth. The large scale surface roughness can be characterized with *ALS* data as a faceted structure. Subsequently, we have presented how we simulate an orientation of multiple facets with inverse transform sampling, summarizing flow-chart of the used method is presented in figure 3.10. By merging the *MILLAS* model with geometrical optics, we obtained a statistical model to investigate the influence of the large scale roughness on the sea

Geometrical Roughness Model

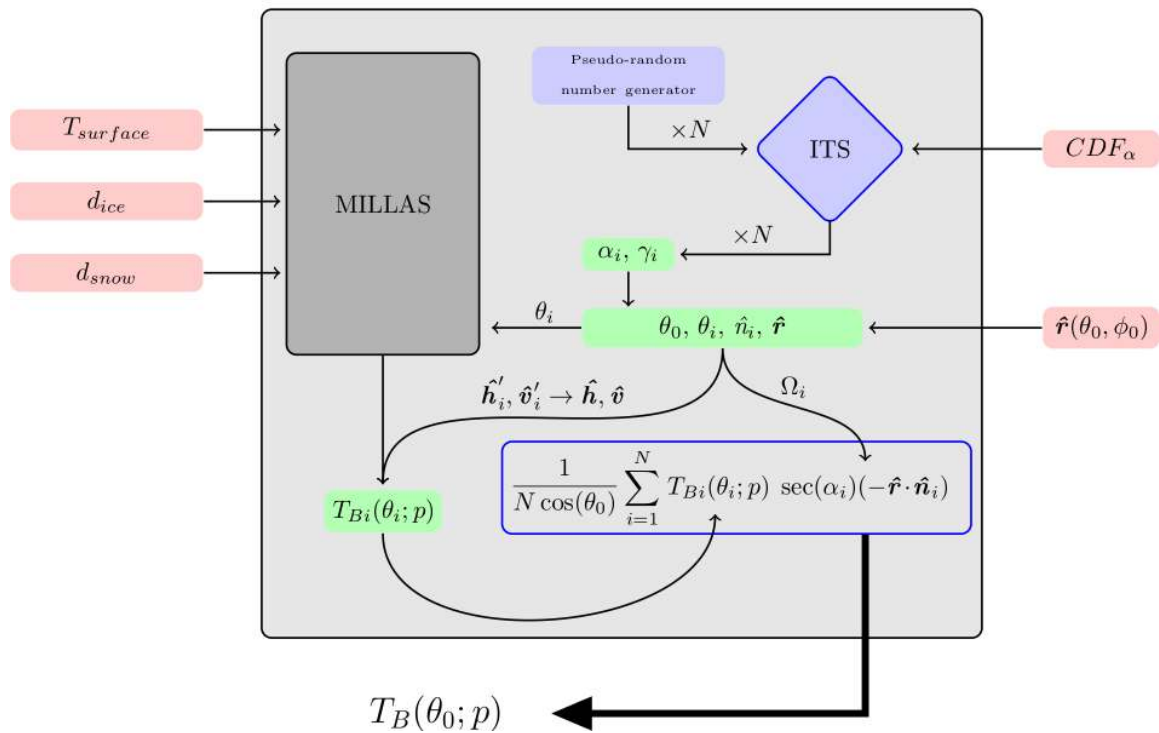


Figure 3.10: Flow chart presenting the individual components of the statistical roughness model. The brightness temperature simulation is done with *MILLAS* model, with T_{surf} , d_{ice} , d_{snow} as inputs. Antenna look angle is another input parameter ($\hat{r}(\theta_0, \phi_0)$). The N -facet orientation (α_i, γ_i) is computed with inverse transform sampling *ITS*, based on cumulative distribution functions of surface slopes orientation (CDF_{α}). Brightness temperature contributions from respective facets are weighted with solid angles under which they are observed (Ω_i). The $T_B(\theta_0, p)$ is the end-simulated brightness temperature of a rough surface.

ice T_B . In this place it is important to note the method assumptions. Firstly, the internal scattering within the ice is neglected. In addition, only bulk temperature and permittivity are considered. Secondly, the small scale roughness is neglected as well as multiple reflections from the surface facets. Thirdly, the radiometer is positioned in a far field, $\hat{r}(\theta_0, \phi_0) = \text{const.}$, and its idealized antenna has a constant gain across the footprint $\omega_i = 1$. This model setup will be used together with surface roughness characteristics from the SMOSice2014 campaign, presented in the next chapter.

Chapter 4

Surface roughness characteristics during SMOSice2014

In this chapter we present the measurements of the sea ice roughness made during the *SMOSice2014* campaign. The first section describes the identification of three ice types with distinct roughness characteristics by aerial photography. The ice types are labeled “smooth”, “medium-deformed” and “deformed”. We chose three ice types that can be easily distinguished from each other, so we can look in to robust method of characterizing the surface roughness from elevation data. Once labeled, we investigated the standard deviation of surface height (σ_z) each of the ice types. The second section focuses on the power spectral analysis of the surface elevation profiles measured over the three ice types. The best fitting type of auto-correlation function is calculated with a set of band-limited roughness parameters (σ_{bl} , l_{bl}). The third section presents the results of the Geometrical Optics approach to surface roughness description. Here the surface facets slopes orientation are derived from the digital elevation model (*DEM*). The probability distribution function of the surface slopes is a key input to the statistical roughness model described in the chapter 3.

4.1 Sea ice classification

The roughness-based sea ice classification is done manually by visual interpretation of the camera images. The photos were not taken continuously during the flight. The ice is flagged as “deformed” when ridges or rubble fields are dominating the image. When floes of similar dimensions without dominant ridges are visible, the ice is labeled as “medium-deformed”. The ice is classified as “smooth” when finger rafting or dark nilas are visible, indicating that the ice is newly formed. Images that contained few ice types are discarded.

The *ALS* elevation data is grouped into one-second sections. The section size corresponds to the footprint of the nadir-looking antenna of the radiometer. It consists

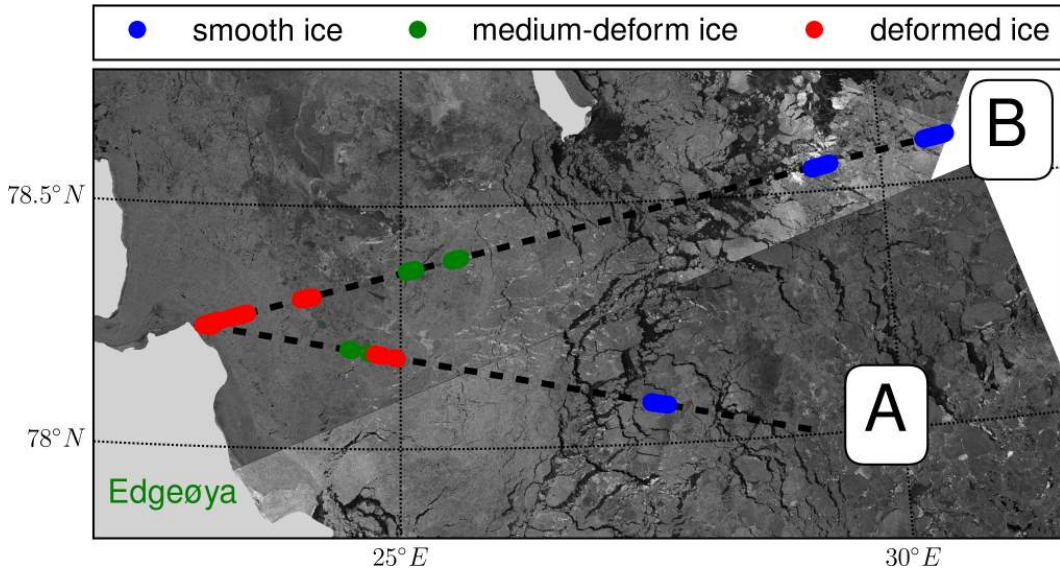


Figure 4.1: Locations of the three identified ice types smooth in *blue*, medium-deformed in *green* and deformed in *red*. In background is the TerraSAR-X wide swath mode (HH polarization), with frames taken at 05:35 UTC and 14:58 UTC. The aircraft tracks are marked in *black dashed lines* - **A** at 10:05-10:41 UTC and **B** at 11:25-12:07 UTC .

	d_{ice} (m)	Flight A	Flight B	Sum
Smooth ice	0.08 ± 0.23	54	100	154
Medium-deformed ice	1.42 ± 0.25	25	60	85
Deformed ice	1.90 ± 0.97	55	161	216

Table 4.1: Ice classification summary with the number of one-second sections in each flight and corresponding sea ice thickness.

of 150 scan lines spaced every 0.5 m. Each scan line is 70 m long and composed of 340 elevation measurements. Flights **A** and **B** contained 2189 and 2473 sections, respectively. All sections, in both flights, have the surface elevation distributions that fail the χ^2 test for "normal distribution" (p -value=0.05, $N_{bins} = 24$).

One-second sections corresponding to the ice type regions are used in the subsequent analysis. Figure 4.2 shows an example of "smooth ice" seen on a photography and in the raw *ALS* elevations. Table 4.1 presents the summary of the manual classification.

We calculate the standard deviation of surface height (σ_z) in the one-second sections associated with each of the defined ice types. Figure 4.3 shows the histograms of the σ_z for the three ice types, while table 4.2 summarizes the statistics of the histograms. The values corresponding to "smooth ice" are considerably lower than those of the other two ice types. The mean σ_z for this ice type is 0.02 m and it is less than the *ALS* accuracy. The "medium-deformed" ice has a symmetric distribution centered at 0.15 m with skewness of 0.04. The "deformed" ice has an asymmetric distribution with a mean of 0.25 m tailing towards higher values.

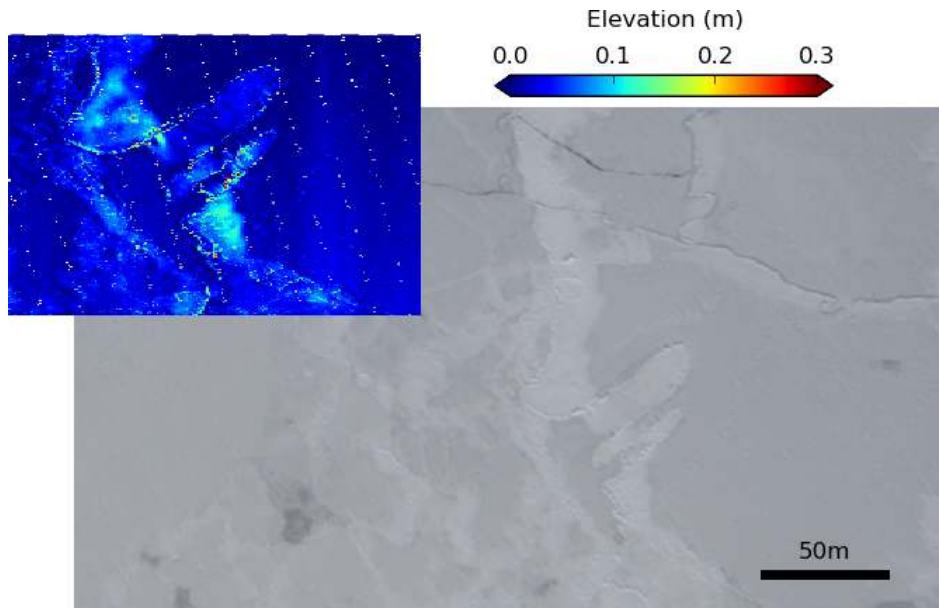


Figure 4.2: An example of “smooth ice” region. The aerial photography shows finger rafting, a feature also visible in the *ALS* raw elevation data in the upper subplot. The photo was taken at 10:03:14 at position: 78 5’ 6.39”N , 27 30’ 57.75”E.

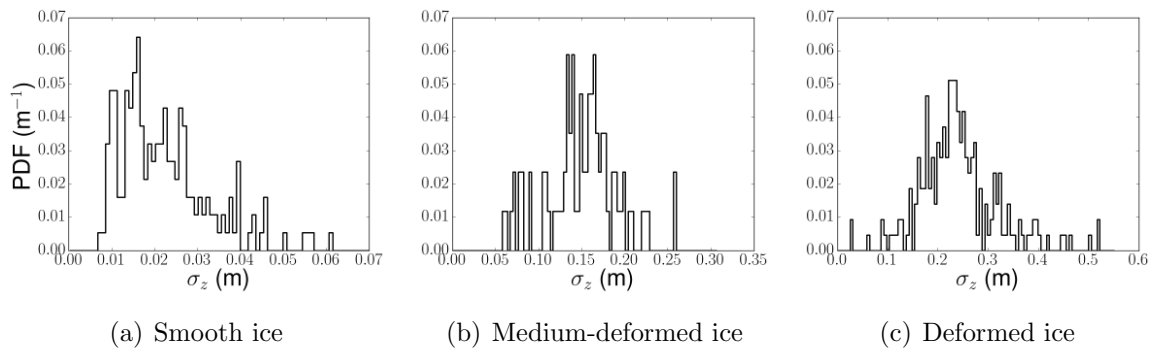


Figure 4.3: Histograms of the σ_z , calculated over one-second sections, for the three identified ice types.

	Distribution parameters			
	mean	standard deviation	skewness	kurtosis
Smooth ice	0.02	0.01	1.13	1.18
Medium-deformed ice	0.15	0.04	-0.04	0.19
Deformed ice	0.25	0.16	9.77	121.79

Table 4.2: Surface roughness (σ_z) distribution parameters for the three ice classes.

4.2 Power spectral densities

Given elevation profiles $z(x)$, where x represents the cross-track position in *ALS* scanline of length L with N samples, the roughness power spectral density ($PSD(f_x)$) is estimated in terms of the discrete Fourier transform of $z(x)$:

$$PSD(f_x) = |\mathcal{F}(z(x))|^2, \quad (4.1)$$

where $f_x = k\Delta f_x$, $\Delta f = 1/L$, $k = 1, \dots, N$. Similarly, in the spatial domain the discrete positions are $x = n\Delta x$, $\Delta x = L/N$ and $n = 1, \dots, N$

The band-limited roughness parameters σ_{bl} and l_{bl} are calculated from the PSD . According to the Wiener–Khinchin theorem for a stationary random process, the Fourier transform of the auto-correlation function ($R(\xi)$) is the PSD (Champeney, 1973). The $PSDs$ obtained from the *ALS* scans are confined to the interval $[f_{min}, f_{max}]$. For the sampling distance $\Delta x = 0.25$ m and scan length $L = 70$ m we obtain the values $f_{min} = 0.014 \text{ m}^{-1}$, $f_{max} = 2 \text{ m}^{-1}$.

We derive the $PSDs$ in three steps. Firstly, the scanlines are linearly interpolated to obtain a regular spacing of 0.2 m. Only scanlines with less than 5% missing values are considered. The remaining missing values are patched with white noise. Secondly, the discrete Fourier transform of the profile is computed and the modulus-squared taken. Thirdly, the $PSDs$ of each scanlines are averaged over one second to increase the statistical significance. Figure 4.4 shows the mean PSD over the three ice types, obtained by averaging the one-second sections falling in the regions attributed to the respective ice types. The gray area marks the sampling bandpass, a tail of values greater of 2 m^{-1} resouts from oversampling of the original data. The dashed line marks the best fit of the Lorentzian function.

The theoretical noise level (N_0) for the mean roughness spectra is $N_0 \approx 10^{-7} \text{ m}^2$

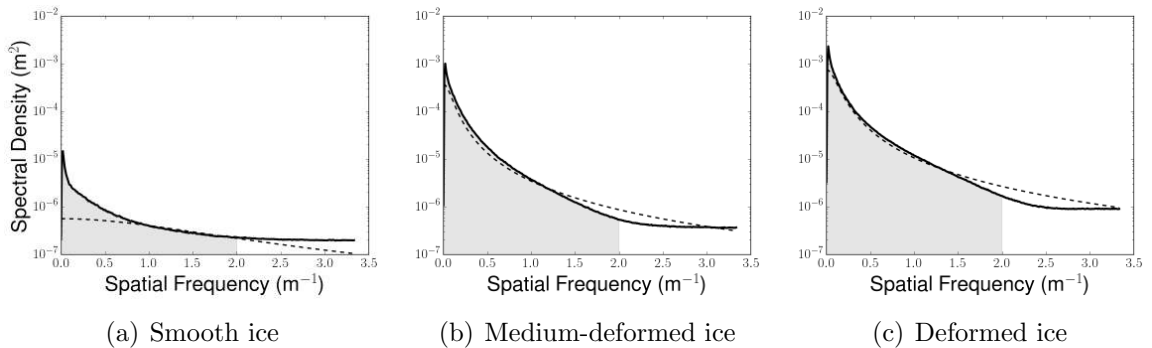


Figure 4.4: The power spectral densities of surface roughness profiles over the three ice types (*solid black line*). The dashed line marks the best-fit empirical spectral model (the Lorentzian function). *Gray area* marks the sampling bandpass, ranging from f_{min} to f_{max} .

derived from:

$$N_0 = \frac{\delta_{ALS}^2}{N\sqrt{N_{AV}}}, \quad (4.2)$$

where δ_{ALS} is the single elevation measurement uncertainty, N_{AV} is the number of profiles averaged. All three *PSD* are above the noise threshold. However, other sources of uncertainty need to be considered. The process of selecting the scenes with aerial photography is most difficult to assess. Surfaces put together in one ice type by visual interpretation can differ significantly, which explains the spread of σ_z shown in Figure 4.3c. Figure 4.4a suggest an exceptionally strong contribution from the low spatial frequency lower than 0.1 m^{-1} . We interpret this feature as one related to the swell that causes the undulations of the elastic thin ice. This partly explains the *PSD* - “model best-fit” mismatch.

In order to retrieve the $R(\xi)$, two empirical models are fitted to the *PSDs*. The first assumes that $R(\xi)$ is an exponential function, the second assumes it as Gaussian. The *PSDs* of the stationary random processes characterized by these $R(\xi)$ types correspond to Lorentzian and Gaussian functions, respectively (Champeney, 1973). Table 4.3 contains the relevant formulas.

$$R(\xi) \xrightarrow{\mathcal{F}} PSD(f)$$

Spatial		Frequency	
Exponential	$\sigma_{bl}^2 \exp(- \xi /l_{bl})$	Lorentzian	$\sigma_{bl}^2 \frac{2l_{bl}/L}{1+(2\pi l_{bl}f)^2}$
Gaussian	$\sigma_{bl}^2 \exp(-\xi^2/l_{bl}^2)$	Gaussian	$\sigma_{bl}^2 (l_{bl}/L)\sqrt{\pi} \exp(-\pi^2 f^2 l_{bl}^2)$

Table 4.3: Empirical models for autocorrelation function $R(\xi)$ and their *PSD* counterparts in a frequency domain.

The best-fit parameters σ_{bl} , l_{bl} for the Exponential-Lorentzian and Gaussian-Gaussian models are presented in the Table 4.5. In the case of “smooth ice” the correlation length is fitted to be less than the sampling interval. This indicates that the roughness signal is weak and σ_{bl} is comparable with *ALS* accuracy. Thus it is justified to treat “smooth ice” as a specular surface for the sampled frequencies. The two model estimations for the roughness parameters differ significantly, although in both models “deformed ice” has the highest σ_{bl} .

The values of mss are smaller than 0.4, which is critical value above which contributions from multiple scattering should be included (Dierking, 2000). In order to determine which spectral model represents better the *PSD* in the band-pass range, a normalized χ^2 test is performed as follows:

$$\chi^2/\nu = \frac{1}{\nu} \sum_i^N \frac{(PSD(f_i) - model(f_i))^2}{\sigma_i} \quad (4.3)$$

	m_{ss}	Model fits			
		Lorentzian		Gaussian	
		l_{bl}	σ_{bl}	l_{bl}	σ_{bl}
Smooth ice	0.008	0.14	0.01	0.17	0.01
Medium deformed ice	0.054	1.64	0.08	0.36	0.05
Deformed ice	0.167	1.33	0.14	0.35	0.09

Table 4.4: Fitted Band-limited roughness parameter values (σ_{bl} , l_{bl}), for the two proposed empirical autocorrelation functions.

χ^2/ν	smooth ice	medium-deformed ice	deformed ice
Lorentzian	15.5	10.7	6.4
Gaussian	14.6	80.5	59.3

Table 4.5: Values of the normalized χ^2

where $\nu = N - 2$ denotes the degrees of freedom, *model* is the candidate fitting function (Gaussian or Lorentzian), and $\sigma_i = PSD(f_i)/\sqrt{N_{AV}}$ describes the uncertainty in each spectral density estimate. Values $\chi^2/\nu < 1$ is a sign of overestimation of the uncertainties, whereas the values of $\chi^2/\nu > 1$ indicate a good model fit, $\chi^2/\nu \gg 1$ means poor model fit. Table 4.5 presents the results of this test. Both models have high values of normalized χ^2 statistic. Nonetheless, the Lorentzian spectral model is a better fit to the averaged *PSDs* for “medium-deformed ice” and “deformed ice”. In the case of ‘smooth ice’ both models have comparable results.

4.3 Geometrical optics and facet slopes orientation

The results from the previous sections show how the three ice types differ in terms of their σ_z and *PSDs*. In this section, we derive the slopes orientation statistics from the digital elevation model (*DEM*). The surface elevations measured by the *ALS* are spatially interpolated to a regular $0.5\text{ m} \times 0.5\text{ m}$ grid. The cross-track dimension is over sampled, whereas grid resolution matches the along-track distance between scan lines. The result is a *DEM* of the ice surface. Based on the *DEM* corresponding to each one-second section, the surface slopes α and their azimuthal orientations γ are calculated. Figure 4.5 presents examples of the *DEMs* for the three ice types, together with derived slopes and their orientation.

The azimuthal directions are expressed with respect to the true north. Subsequently, histograms of the α and γ are made in order to evaluate whether there is a preferential direction for the facet orientation. The number of bins in the histograms (N_{bins}) is set according to the formula 4.4 after Schönwiese (2013), first proposed

by Panofsky Hans A. and Brier Glenn W. (1958)

$$N_{bins} = 5 \log_{10}(N_m) \quad (4.4)$$

where N_m is the number of measurements. In the case of one-second sections N is approximately 6000 and the number of bins $N_{bins}=23$.

We found that in all one-second sections, in both flights, the distribution of azimuths fails the χ^2 test for the uniform distribution with a confidence level of 0.95. This means that in the studied region at the scale of one section (70 m) the hypothesis that slopes have no preferred orientation is rejected.

In the next step we validate at which length scale the slopes azimuthal distribution can be treated as uniform. For that, we approach this matter similarly to Beckers et al. (2015) and select 1000 random samples from the flights, each sample has a length of 15 km. We then compute the cumulative azimuth distribution statistics along the sample's length.

In order to evaluate the relative deviations from the uniform distribution, we define a f_R parameter (eq. 4.5). This parameter equals to zero for the perfectly uniform distribution, in which case the number of counts in each bin (n_i) equals to a mean number of counts (μ). The f_R parameter reaches its maximum value of $f_{Rmax} = 2-4/K$ when the slopes are aligned, i.e. grouped in two bins.

$$f_R = \frac{\sum_i^{N_{bins}} (|n_i - \mu|)}{N_{bins}\mu}, \quad \mu = \frac{1}{N_{bins}} \sum_i^{N_{bins}} n_i \quad (4.5)$$

The analysis of 1000 samples show that the deviation from the uniform distribution decreases sharply with increasing distance over first kilometer. In 90% of the samples the curve flattens at value of $f_R = 0.05$ for distance along the sample greater than 4.3 km. We assume that at scale greater than 4.3 km (vertical dashed line on figure 4.6 on page 48) the slopes orientations do not have a preferential direction beyond natural variability. This distance corresponds to approximately 60 one-second sections. In figure 4.6 the average value of the f_R is marked as thick black line. Several profiles are plotted in color lines to illustrate the variability.

In all three ice classes we have identified more than 60 one-second sections. Considering the above, we assume that there will be no preferential direction of the surface facets azimuthal orientation. As a result, we find that the 3 ice types show different characteristics with respect to facet slopes. Figure 4.7 on page 48 presents the histograms of measured slopes angles for the three ice types. In order to obtain the

	<i>GAUSS</i>		<i>EXP</i>		<i>EXP - n</i>		
	<i>RMSD</i>	$s_{\alpha,g}$	<i>RMSD</i>	$s_{\alpha,e}$	<i>RMSD</i>	$s_{\alpha,n}$	n
Smooth ice	3×10^{-5}	2.94	2×10^{-5}	2.94	2×10^{-5}	0.85	0.91
Medium-deformed ice	660×10^{-5}	7.33	55×10^{-5}	7.33	11×10^{-5}	3.73	0.76
Deformed ice	473×10^{-5}	14.79	3×10^{-5}	14.78	2×10^{-5}	10.96	0.98

Table 4.6: Facet slope distribution parameters.

slopes distributions, three types of curves are fitted: Gaussian (*GAUSS*), exponential (*EXP*), and Exponential with free exponent (*EXP - n*)(eq. 4.6).

$$PDF_{\alpha} \approx \exp(-|\alpha/s_{\alpha,X}|^n) \quad (4.6)$$

where $s_{\alpha,X}$ is the parameter characterizing the slop distribution. X stands for g , e or n for Gaussian, exponential or exponential with free exponent variants, respectively.

The results of the fit are displayed in table 4.6. Among these three curves the Gaussian function has the poorest fit with respect to the root-mean-square difference (*RMSD*). At the same time, the exponent parameter in *EXP - n* is close to one for “smooth” and “deformed ice” 0.91 and 0.98, respectively. For the “medium-deformed” ice this parameter is equal to 0.76. For further analysis we will use the one-parameter exponential curve for slope distribution description.

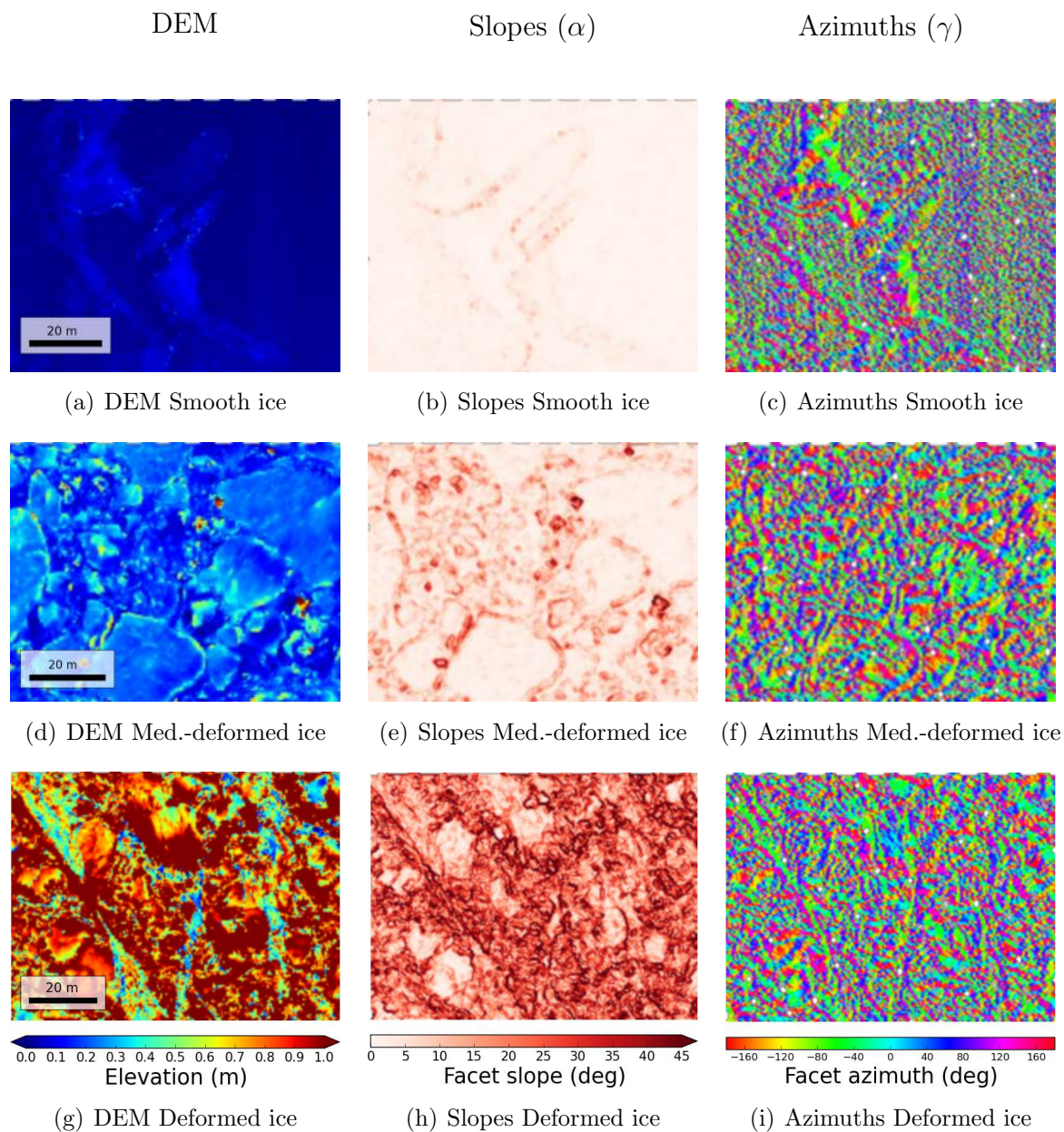


Figure 4.5: First columns contains examples of digital elevation model (*DEM*) for three ice classes: smooth ice (a), medium-deformed ice (d) and deformed ice (g). Second column (b,e,h) presents surface facet slopes derived from the *DEM*. In the third column (c,f,i) the azimuthal orientation of the facet is shown.

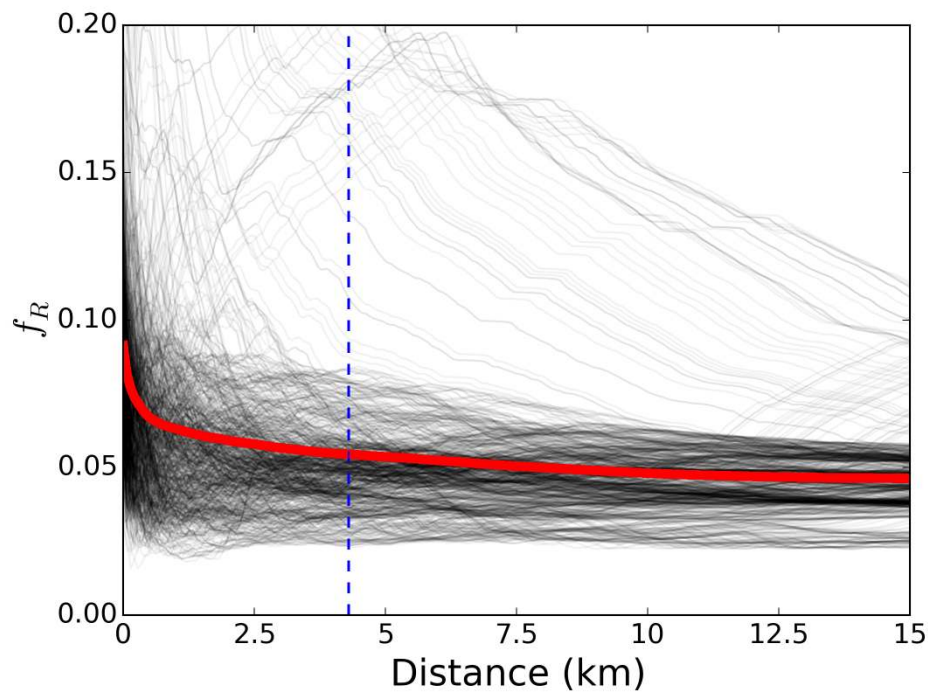


Figure 4.6: The values of the distribution parameter f_R calculated along the random samples. *Thick red* line marks the average value. To illustrate the variability, we present the f_R values for several samples, marked in gray lines.

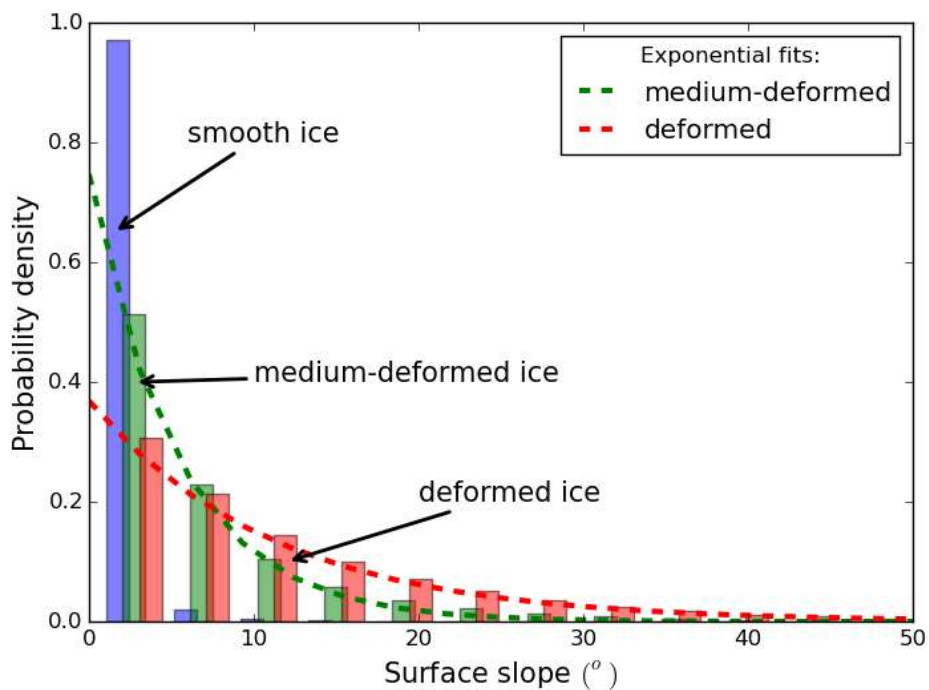


Figure 4.7: Histogram of surface slope distributions. The three ice types “smooth”, “medium deformed” and “deformed” are marked in blue, green, red, respectively. The *dashed lines* mark the exponential function fits to the slope histograms for “medium deformed” in *green* and “deformed” in *red*.

4.4 Summary and discussion

In this chapter we investigated roughness characteristics of the three ice types that we identified by aerial photography. We analyzed the standard deviation of surface heights and the power spectral densities of the “smooth”, “medium-deformed” and “deformed” ice types. Both methods showed clear differences between the ice types. Also, the “smooth ice” shows little difference to a specular surface. Furthermore, we determined that the exponential auto-correlation function is more appropriate than the gaussian one, regardless of the ice type. According to Oh and Kay (1998), the sampling interval should not be greater than $0.2l_c$ for an accurate calculation of the correlation length. The exponential band-limited correlation lengths for “medium-deformed” ($l_{bl,med} = 1.64$ m), and “deformed” ($l_{bl,def} = 1.33$ m) satisfy this criterion.

The facet orientation probability distribution function (*PDF*) is a key parameter in the statistical roughness model described in chapter 3. The facet orientation is described by two angles: the slope α and the azimuth γ . Dynamical processes such as piling of the ice against the coast or forming of pressure ridges can result in local elongated structures, which is a sign of a preferential slopes direction. On a larger scale, where wind and currents bring ice from different regions, these anisotropies should be negligible. However, in surface roughness analysis it is often assumed that surface slopes have an isotropic azimuthal distribution even on a scale of tens of meters (Liu et al., 2014). We evaluated the slopes orientation along the flight tracks during the *SMOSice2014* campaign. We found that at a scale larger than 4.3 km the sea ice surface slopes do not have any preferential azimuthal direction ($PDF_\gamma \approx const.$). In a case of an isotropic slopes orientation Schanda (1986b) proposed a symmetrical PDF_α with a maximum around zero. We used an exponential function to parametrize the PDF_α . This one-parameter function is a better fit to the measured data than the Gaussian function and is easier to handle than the two-parameter *EXP - n* model, which brings some improvement to the fit, but too insignificant to prove computationally cost-effective. Therefore, in further analysis we will use an exponential PDF_α model for all ice types. And s_α as way of measuring the degree of surface roughness.

Chapter 5

Influence of the surface roughness on the modeled brightness temperature

In this chapter we will combine the surface roughness characterization presented in chapter 4 with the statistical roughness model from Chapter 3. The aim is to investigate the change in angular characteristics of horizontal and vertical brightness temperature (T_B).

In section 5.1 we look into the model's sensitivity to input parameters: surface temperature (T_{surf}), ice thickness (d_{ice}), snow thickness (d_{snow}), as well as the surface slopes probability distribution described by s_α parameter. Section 5.2 combines the sensitivity study with typical uncertainty ranges of the input parameters. This allows to evaluate of the relative importance of surface roughness. In section 5.3 we propose a “fast model” parametrization of the time-consuming statistical model results. Section 5.4 presents a discussion on the possibility of extending the “fast model” parametrization to other surfaces with different permittivity.

5.1 The sensitivity study

We generate N randomly oriented facets with a Monte Carlo roughness model which takes as input the probability distribution function of surface slopes (PDF_α). The azimuthal orientation of the facet is assumed to be uniform and random, following the analysis in section 4.3. In this statistical approach the value of N must be large enough for accurate results. If N is too small, the individual model runs with identical setups will produce different results. In order to determine the optimal value for N we evaluate the standard deviation of 20 model runs, which is a reasonable sample size to draw conclusion on the distribution (Chelli, 2012). As a metric we chose the

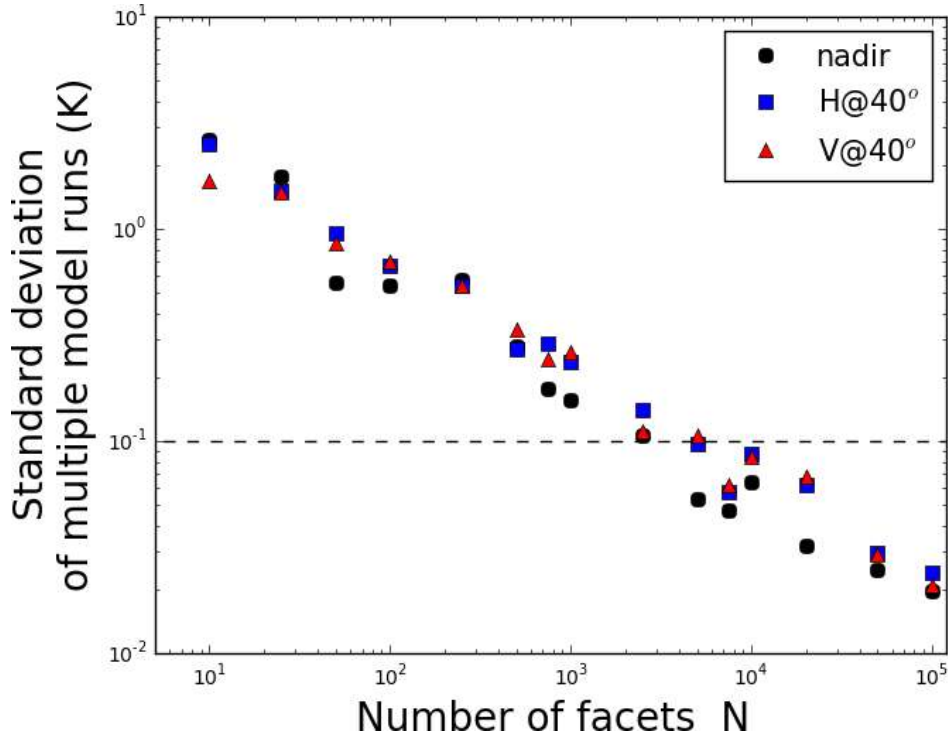


Figure 5.1: Standard deviation of the 20 model runs at nadir (black) and at 40° (H -blue, V -red) as a function of number of the facets N . The horizontal *dashed* line marks the *EMIRAD2* accuracy of 0.1 K obtained after 1 s integration time.

T_B at nadir and at 40° , which corresponds to the incidence angle of the side looking antenna of *EMIRAD2* and the one of *SMAP* (*SMOS* multi-angle measurements also include those angles). The setup for the *MILLAS* model is as follows: $T_{surf} = 260$ K, $d_{ice} = 1.42$ m, $d_{snow} = 0.14$ m. These values correspond to the conditions encounter over “medium-deformed ice” during *SMOSice2014* campaign (see chapter 4).

Figure 5.1 shows the standard deviation of 20 model runs at nadir (black) and at 40° (H -blue, V -red) as a function of the facet number N . The *EMIRAD2* radiometer accuracy is 0.1 K for a 1 s integration time (Søbjaerg et al., 2013; Hendricks et al., 2014), marked with a dashed line in the figure. The standard deviation of the selected measurements is lower than the 0.1 K threshold for $N \geq 10^4$. Therefore, for further analysis we set the number of facets to $N = 10000$.

5.1.1 The impact of ice concentration

In our simulations we assume that the sea ice concentration (C) is equal to 100%. However, this assumption is seldomly fulfilled on the scale of *SMOS* resolution (≈ 40 km). Ice openings, leads, polynya and constant movement of the ice contribute to the open water fraction, reducing C . We account for sea ice concentration with a

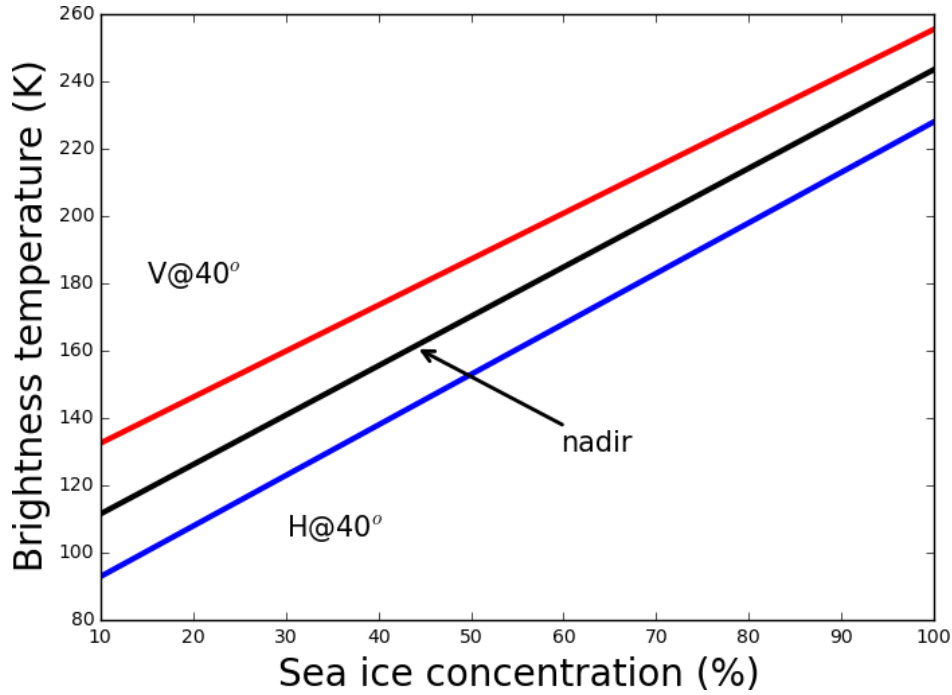


Figure 5.2: Sensitivity of the modeled brightness temperature to sea ice concentration (C). The other parameters are kept constant: $T_{surf} = 260$ K, $d_{ice} = 1.42$ m, $d_{snow} = 0.14$ m, $s_{\alpha} = 0^{\circ}$

simple linear mixing approach:

$$T_B(\theta) = C \cdot T_{Bice}(\theta) + (1 - C) \cdot T_{Bwater}(\theta) \quad (5.1)$$

where T_{Bice} and T_{Bwater} denote the brightness temperatures for sea ice and open water (the equation is valid for both polarizations). This method requires auxiliary data about the sea ice concentration. Figure 5.2 shows the effect of the changing ice concentration on the observed T_B , as calculated with eq. 5.1.

The respective slopes for nadir and 40° are $\frac{\partial T_B(0)}{\partial C} = 1.47$ K/1%, $\frac{\partial T_B(H,40)}{\partial C} = 1.50$ K/1%, $\frac{\partial T_B(V,40)}{\partial C} = 1.37$ K/1%.

5.1.2 The impact of ice thickness

Sensitivity of the L-band T_B to the sea ice thickness is essential for the sea ice thickness retrieval. The strongest increase in T_B is observed for ice thinner than 0.5 m (figure 5.3). Thin ice rarely has a deformed/rough surface which is characteristic of dynamic ice growth. The *MILLAS* model predicts little increase in T_B for thick ice. We focus on ice thicker than 0.7 m to single out the contribution of the surface roughness.

For the thick ice ($d_{ice} > 0.7$ m) the sensitivity of the nadir T_B to the ice thickness is $\frac{\partial T_B(0)}{\partial d_{ice}} = 0.73$ K m $^{-1}$. At an incidence angle of 40° the sensitivities of polarized T_B s are

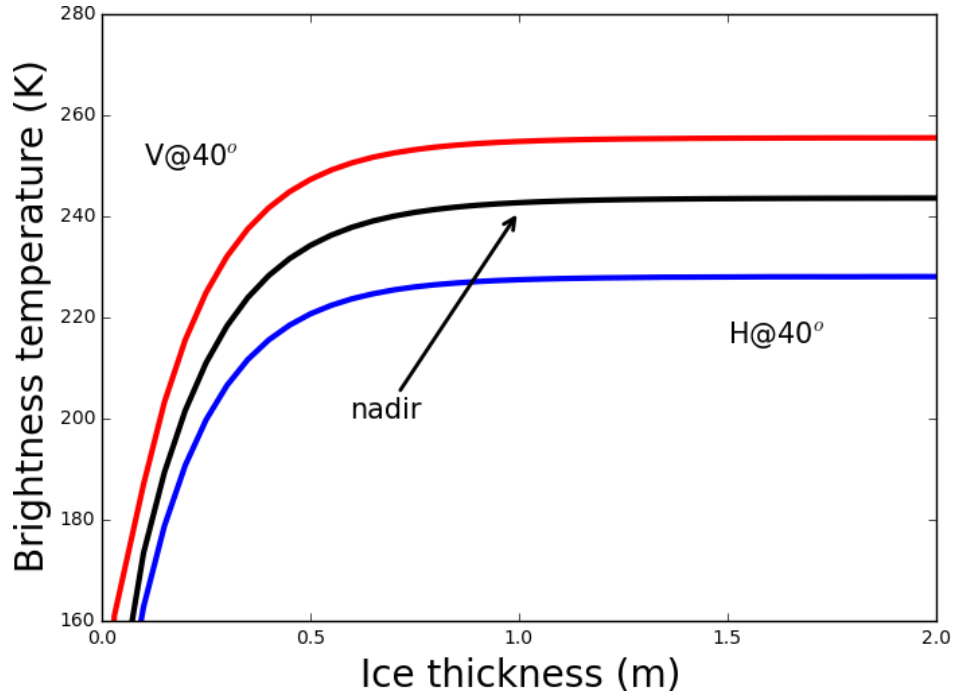


Figure 5.3: Sensitivity of the modeled brightness temperature to sea ice thickness (d_{ice}). The other parameters are kept constant: $T_{surf} = 260$ K, $d_{snow} = 0$ m, $s_{\alpha} = 0^{\circ}$

$\frac{\partial T_B(H,40)}{\partial d_{ice}} = 0.49$ K m $^{-1}$ for horizontal polarization and $\frac{\partial T_B(V,40)}{\partial d_{ice}} = 0.57$ K m $^{-1}$ for vertical polarization.

5.1.3 The impact of snow thickness

Snow on sea ice has two main implications for measured T_B (Maaß et al., 2013). First, it acts as an isolator separating sea ice from the cold atmosphere. This results in an increase of ice effective temperature, which also influences its dielectric properties. Secondly, the layer of snow, even with negligible absorption as it is the case of dry snow, refracts the L-band radiation (Maaß et al., 2015). During the *SMOSice2014* the snow radar was not functioning properly (Hendricks et al., 2014, Data acquisition report). To tackle this problem we use an approximation formula that sets snow thickness to 10% of ice thickness, a method previously applied for snow on sea ice (Yu and Rothrock, 1996; Mäkynen et al., 2013). Figure 5.4 shows the influence of snow thickness on the modeled T_B , with the other parameters kept constant ($T_{surf} = 260$ K, $d_{ice} = 1.42$ m, $s_\alpha = 0^\circ$). The simulated snow thickness changes from 0.01 m to 0.30 m, covering values up to 20% of the sea ice thickness.

The T_B curves have the strongest gradient for the snow thickness lower than 0.1 m: $\frac{\partial T_B(0)}{\partial d_{snow}} = 21$ K m⁻¹, $\frac{\partial T_B(H,40)}{\partial d_{snow}} = 16$ K m⁻¹, $\frac{\partial T_B(V,40)}{\partial d_{snow}} = 22$ K m⁻¹. For the thicker snow cover the increase in modeled T_B s is less pronounced. For the snow thickness between 0.1 m and 0.2 m the respective sensitivities are: $\frac{\partial T_B(0)}{\partial d_{snow}} = 5.7$ K m⁻¹, $\frac{\partial T_B(H,40)}{\partial d_{snow}} = 3.5$ K m⁻¹, $\frac{\partial T_B(V,40)}{\partial d_{snow}} = 7.6$ K m⁻¹.

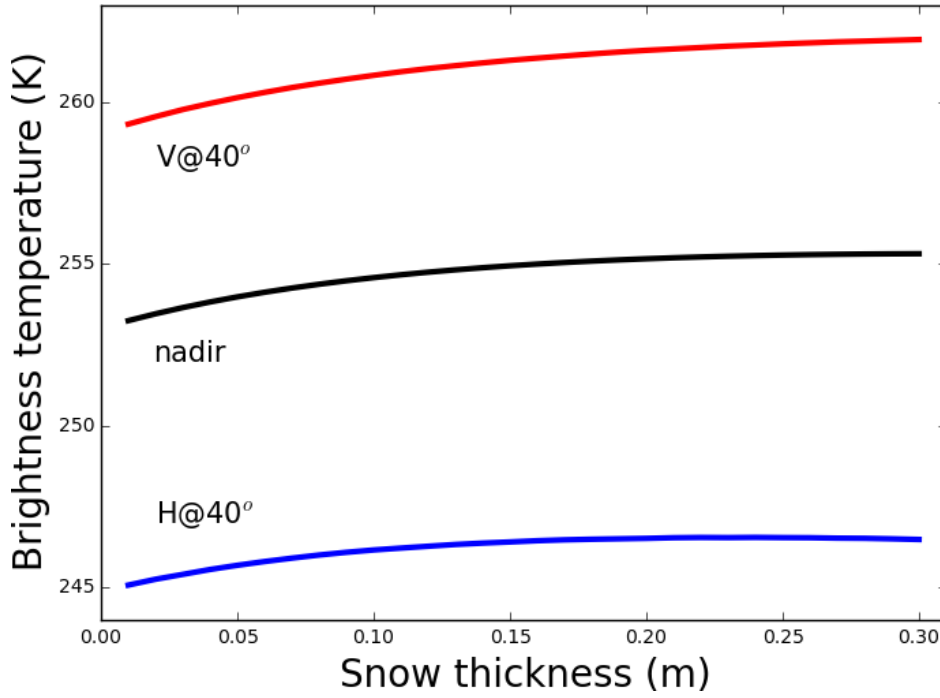


Figure 5.4: Sensitivity of modeled brightness temperature to snow thickness (d_{snow}). Other parameters are kept constant: $T_{surf} = 260$ K, $d_{ice} = 1.42$ m, $s_{\alpha} = 0^{\circ}$

5.1.4 The impact of surface temperature

Surface temperature is a crucial boundary condition that determines the temperature gradient within snow and ice. In the *MILLAS* model the permittivity of ice is linked to the ice temperature through brine volume fraction (Vant et al., 1978; Cox and Weeks, 1982). Therefore the surface temperature influences the ice effective temperature, as well as its emissivity. The effect on the sea ice emissivity is pronounced for the relatively warm conditions $T_{surf} > 265$ K. This is shown in figure 5.5 where the values of T_B are decreasing as the surface temperature rises above (265 K). Below this critical temperature the T_B s increase monotonically with approximately constant pace: $\frac{\partial T_B(0)}{\partial d_{snow}} = 0.14$ K K⁻¹, $\frac{\partial T_B(H,40)}{\partial d_{snow}} = 0.1$ K K⁻¹, $\frac{\partial T_B(V,40)}{\partial d_{snow}} = 0.17$ K K⁻¹.

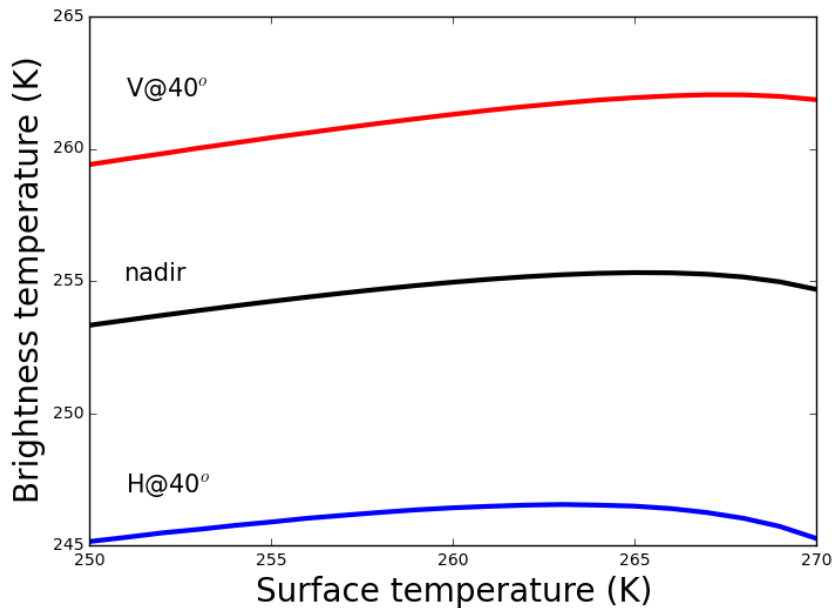


Figure 5.5: Sensitivity of the modeled brightness temperature to surface temperature (T_{surf}). The other parameters are kept constant: $d_{ice} = 1.42$ m, $d_{snow} = 0.14$ m, $s_\alpha = 0^\circ$

5.1.5 The impact of large scale surface roughness

In this work we evaluate the impact of surface roughness on the L-band T_B of sea ice. In our statistical roughness model we characterize the probability density function of surface slopes using an exponential function (PDF_α). The surface roughness parameter s_α describes the shape of PDF_α . Figure 5.6 presents the results of the $T_B(0)$ and $T_B(H/V, 40)$ simulations for the roughness parameter range $1^\circ < s_\alpha < 15^\circ$ with the other parameters kept constant ($T_{surf} = 260$ K, $d_{ice} = 1.42$ m, $d_{snow} = 0.14$ m).

For the $s_\alpha < 4$ we observe little change in the modeled T_B s. Beyond this value the most noticeable difference is the decrease in vertical polarization $T_B(V, 40)$. A smaller trend is visible for the nadir $T_B(0)$. The change in $T_B(H, 40)$ is five times smaller than for the $T_B(0)$ and $T_B(H, 40)$. The maximal sensitivities are observed for the most deformed ice (high s_α): $\frac{\partial T_B(0)}{\partial s_\alpha} = -0.25$ K/deg, $\frac{\partial T_B(H, 40)}{\partial s_\alpha} = 0.05$ K/deg, $\frac{\partial T_B(V, 40)}{\partial s_\alpha} = -0.31$ K/deg.

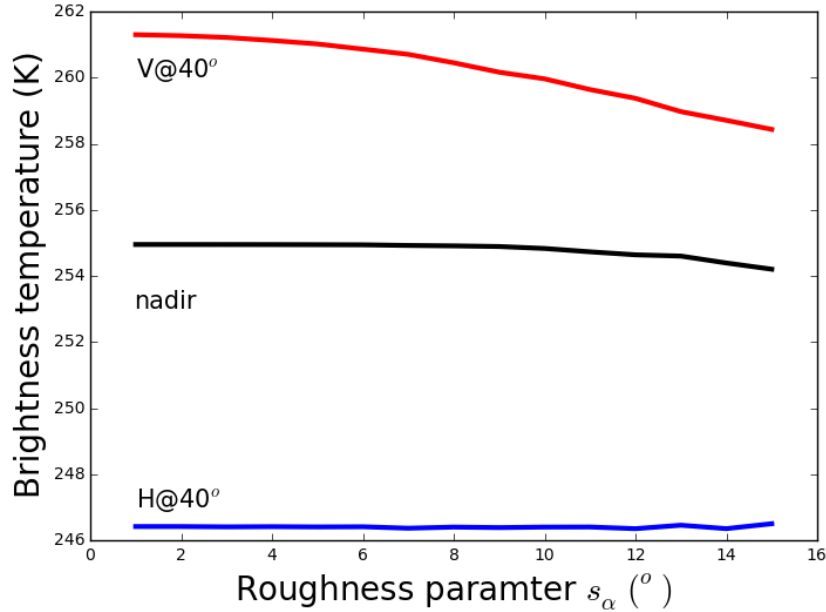


Figure 5.6: Sensitivity of the modeled brightness temperature to sea ice roughness (s_α). The other parameters are kept constant: $T_{surf} = 260$ K, $d_{ice} = 1.42$ m, $d_{snow} = 0.14$ m

5.2 The assessment of uncertainty factors in the modeled brightness temperature

In section 5.1, we have calculated the partial sensitivities of the simulation results to the model inputs. The partial sensitivities vary depending on the range of parameter change. The most pronounced example is the sea ice thickness which has high sensitivity for thin ice and low sensitivity for thick ice.

We compare the uncertainties associated with input parameters by constraining their variations to “realistic” ranges. We assume that sea ice is at least 0.7 m thick and has a snow cover proportional to its thickness. It is justified by the fact that thin sea ice is unlikely to exhibit large surface deformations. Furthermore, we assume that surface temperature is close to -20°C . As for uncertainties related to T_{surf} and d_{ice} we take as reference two satellite products with polar coverage. Sea ice surface temperature can be inferred from the thermal infrared channels of *MODIS*. Hall et al. (2004) have estimated the root mean square error of the *MODIS* sea ice temperature product to be equal to 3.7 K. For the sea ice thickness measurement uncertainty we take the value of 0.28 m, as calculated by Zygmontowska et al. (2014) in the analysis of “Cryosat2” sea ice thickness product accuracy. Sea ice concentration is not specifically included in our roughness model. In the “realistic” scenario we consider C to be close to 100% but with the uncertainty taken from Ivanova et al. (2015). In their study the uncertainty of several passive microwave sea ice contraction algorithms was considered. For the

arctic winter and high sea ice concentration the C standard deviation varied between 3.1% and 8.5%. In this study we take as C uncertainty the arithmetic mean of their results - 5.3% .

Figure 5.7 illustrates the absolute contributions of the mentioned factors to the simulated T_B change. When the respective sensitivities are multiplied by "realistic" parameter changes, the effect of sea ice concentration stands out. The variation in C is the only factor with an effect greater than the uncertainty of a single $SMOS$ measurement (4K). The 2.8K change in vertical polarization due to roughness is also prominent. Figure 5.7 shows the absolute change in modeled T_B . To present not only the magnitude but also the sign of the respective changes, we plot the modeled $T_B(H/V, 40)$ in I^{st} and II^{nd} Stokes coordinates ($\frac{1}{2}(T_B(V, 40) + T_B(H, 40))$, $T_B(V, 40) - T_B(H, 40)$). The simulation for the nadir-looking antenna shows little dependency on the surface roughness, which is shown in figure 5.6. Figure 5.8 uses the Stokes coordinates to present the simulation results for the three ice types: "smooth", "medium-deformed" and "deformed" marked in blue, green and red, respectively. Each point represents one simulation setup. In the simulations setups the sea ice concentration varies from 94% to 100%, d_{ice} from 1.2 to 1.5 m, d_{snow} from 0.12 to 0.15 m and T_{surf} from 253 to 257 K.

The decrease in sea ice concentration results in a lower intensity (x axis - I^{st} Stokes coordinate) and greater polarization difference (y axis - II^{nd} Stokes coordinate). As a result, the entire cloud of points is spread along NW-SE direction. The point clouds corresponding to the three roughness setups are separated. This suggests that retrieving surface roughness information from bi-polar data at 40° incidence angle might be possible.

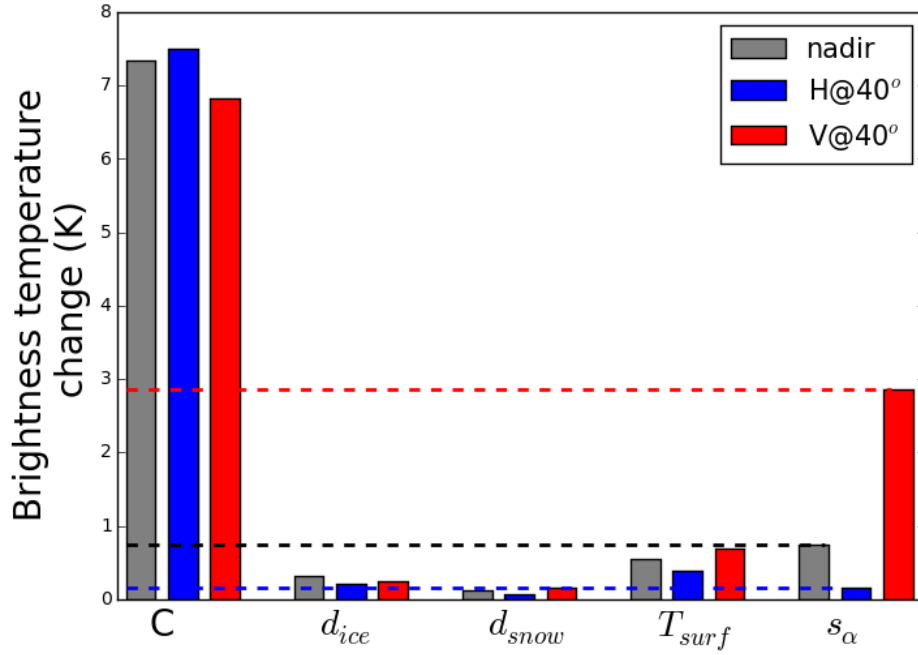


Figure 5.7: Absolute values of the ΔT_B caused by the “realistic” parameter variations. ($\Delta T_{surf} = 3.7$ K, $\Delta C = 5.3\%$, $\Delta d_{ice} = 0.28$ m, $0^\circ < s_\alpha < 15^\circ$). The dashed lines mark the levels of T_B change attributed to surface roughness.

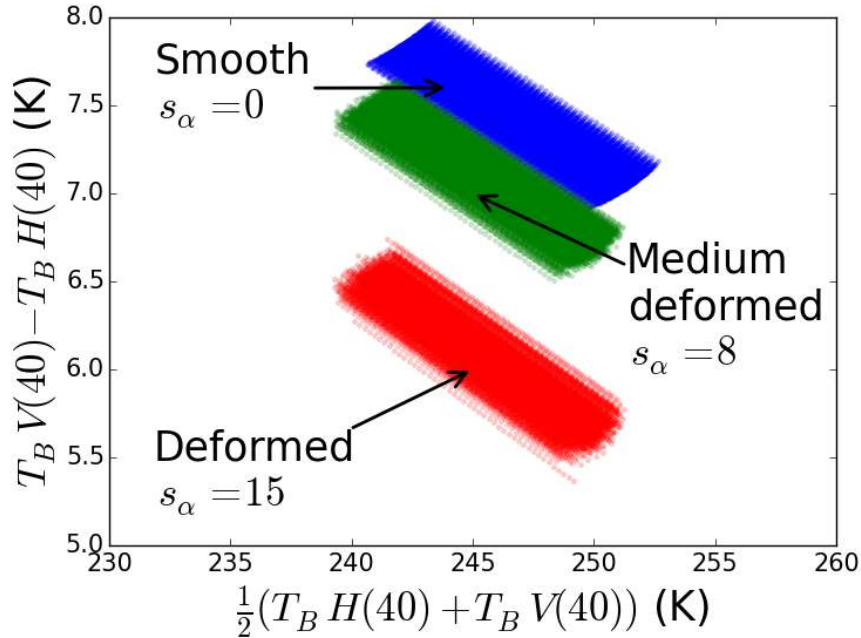


Figure 5.8: Scatter plot of polarization difference vs. mean intensity at 40° for different model setups. The three ice types, “smooth”, “medium-deformed” and “deformed” are marked in blue, green and red, respectively. The sea ice concentration varies from 94% to 100%, d_{ice} from 1.2 to 1.5 m, d_{snow} from 0.12 to 0.15 m and T_{surf} 253 to 257 K and s_α varies from 0° to 15° .

5.3 Fast roughness model

So far in this chapter we have described the influence of surface roughness on the brightness temperature at two incidence angles: 0° and 40° . The influence of the surface roughness on the nadir T_B is important for the *SMOS* sea ice thickness product (Kaleschke et al., 2013, ESA report). The angle of 40° is important because of *SMAP* scanning geometry and it is also the incidence angle of the side-looking *EMIRAD2* antenna. In this section we will describe changes in angular T_B characteristics in a wider range of angles from: 0° to 60° . We propose a parametrization that connects the changes in the modeled T_B with the large scale random surface roughness parameter s_α . Such parametrization eliminates the need for the time consuming Monte Carlo simulations.

Figure 5.9 shows the change in angular T_B characteristic induced by the increase in the roughness parameter s_α from 1° to 15° . The set of blue curves corresponds to the horizontal polarization, while the set of red curves corresponds to the vertical polarization. The more saturated is the color the greater is the value of s_α . The computation is made with the other input parameters kept constant ($T_{surf} = 260$ K, $d_{ice} = 1.42$ m, $d_{snow} = 0.14$ m). The most pronounced change is the decrease in vertical polarization T_B . The behavior of the horizontal polarization is more complex and can be decomposed into two counteracting factors. The first is the polarization mixing which elevates the $T_B(H)$ by adding to it part of the higher $T_B(V)$. The second factor is the slight decrease in T_B caused by the inclusion of high incidence angles ($\theta > 30^\circ$) for which the sum of the two polarizations has a negative trend. This factor becomes stronger with increasing s_α , as observation of high incidence angles is more likely.

We propose a parametrization of the two mentioned effects, the polarization mixing and the drop in T_B , inspired by the *HQ – model* described in chapter 2. Like in the *HQ – model*, we propose two parameters: the H_α that reproduces the change in total T_B intensity and the Q_α that is responsible for polarization mixing. The subscript marks the difference to the parameters from the original *HQ – model* which was dealing with small scale roughness. Equation 5.2 illustrates the relation between emissions from a flat surface ($T_B^*(q, \theta)$) and the one composed of randomly oriented facets with a probability distribution characterized by s_α :

$$T_B(p, \theta, s_\alpha) = [(1 - Q_\alpha) \cdot T_B^*(p, \theta) + Q_\alpha \cdot T_B^*(q, \theta)] \cdot H_\alpha \quad (5.2)$$

where p/q denotes the polarization (horizontal or vertical). For the results depicted in figure 5.9, we made a least square polynomial fit of the eq. 5.2 to determine the following relations: $H_\alpha = f(s_\alpha)$, $Q_\alpha = f(s_\alpha)$. The input data consists of $T_B(H/V)$ pairs for 30 incidence angles spaced at equal intervals in the range from 0° to 60° . Two versions of the parametrization are tested. The first neglects the intensity effect and assumes that $H_\alpha = 1$, named the one parameter version or **1p**. The second version

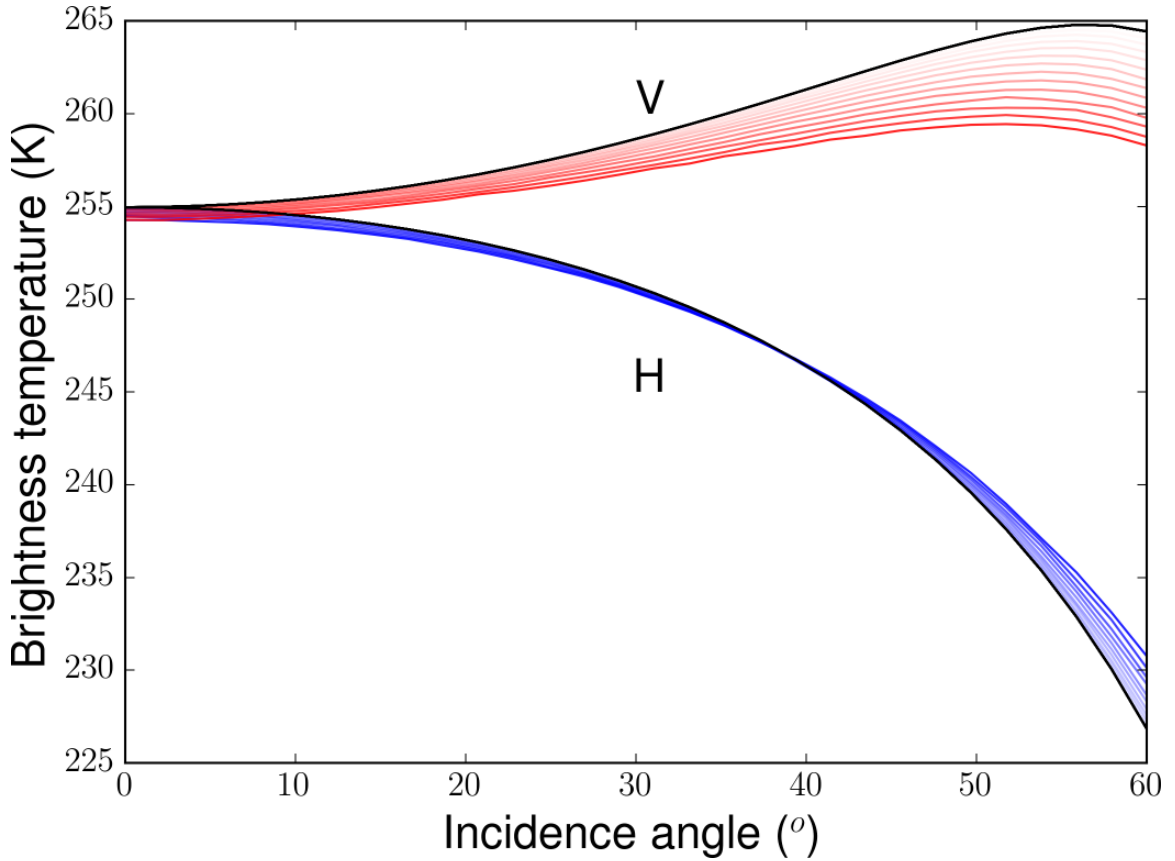


Figure 5.9: Brightness temperature as a function of the incidence angle. The family of red and blue curves represent the results for increasing s_α for each polarizations, the black lines mark the T_B curves for the smooth surface with $s_\alpha = 0^\circ$. The color of the lines intensifies with increasing surface roughness parameter from 1° to 15° . Other parameters are kept constant. ($T_{surf} = 260$ K, $d_{ice} = 1.42$ m, $d_{snow} = 0.14$ m)

allows variations of both parameters, being named the **2p** version. Figures 5.10 and 5.11 show the H_α and Q_α as functions of the roughness parameter s_α .

The boundary conditions for the polynomial fit require that no change in T_B will occur when the surface is flat ($s_\alpha = 0$). Among the functions satisfying this condition the second degree polynomial serves well for the parametrization of both coefficients.

$$H_\alpha = a_1 s_\alpha^2 + a_0, \quad Q_\alpha = b_1 s_\alpha^2 + b_0 \quad (5.3)$$

Table 5.1 contains the best fitting parameter values. The two-parameter version **2p** has a better fit to the data, having root mean square difference ($RMSD$) of 0.45 K in comparison to the one-parameter version that has a $RMSD$ equal to 0.91 K.

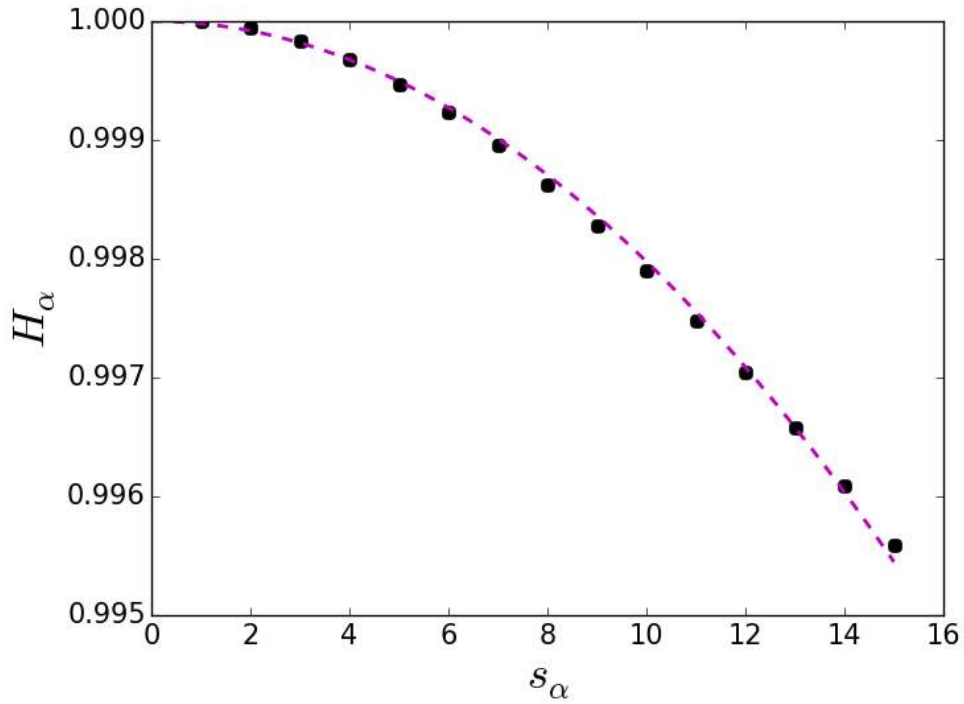


Figure 5.10: The intensity modifying parameter H_α as a function of the roughness parameter s_α . The input T_{BS} were simulated with statistical roughness model for the following reference values: $T_{surf} = 260$ K, $d_{ice} = 1.42$ m, $d_{snow} = 0.14$ m.

Method	Parameter	RMSD (K)
1p	$a_1 = 0, a_0 = 1$ $b_1 = 0.545 \times 10^{-3}, b_0 = 0$	0.91
2p	$a_1 = -0.020 \times 10^{-3}, a_0 = 1$ $b_1 = 0.537 \times 10^{-3}, b_0 = 0$	0.45

Table 5.1: Values of the polynomial coefficients describing the H_α and Q_α as a function of the roughness parameter s_α

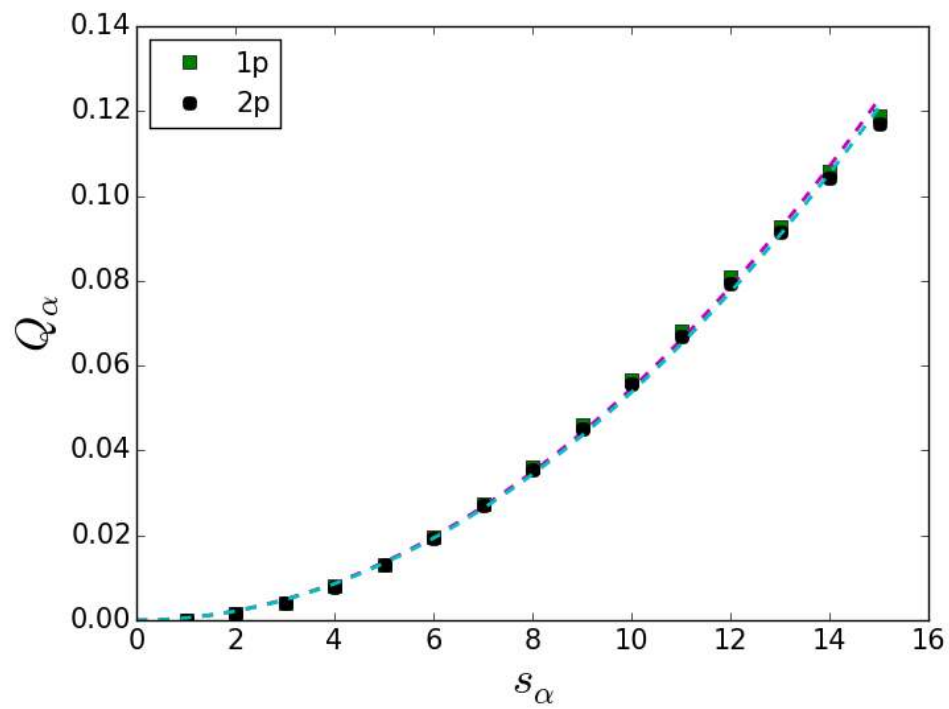


Figure 5.11: The polarization mixing parameter Q_α as a function of the roughness parameter s_α . The two parametrization variants **1p** and **2p** are shown. The input T_{BS} were simulated with the statistical roughness model with the following reference values: $T_{surf} = 260$ K, $d_{ice} = 1.42$ m, $d_{snow} = 0.14$ m

5.4 Extending the parametrization for other surfaces

The statistical roughness model simulates the brightness temperature of a faceted surface with uniformly random azimuthal orientation and predefined slopes probability distribution (PDF_α). In this work we used the slopes statistics derived from airborne laser scanner over sea ice and the *MILLAS* model to simulate the sea ice brightness temperature. Nonetheless, it is possible to use our statistical roughness model with a different emissivity model, such as the one used for soil moisture retrieval, with a PDF_α more suitable for the studied surface.

To demonstrate this principal we substitute the *MILLAS* model with specular emissivity described by Fresnel equations. The permittivities correspond to loamy soil (30.6% sand, 55.9% silt, 13.5% clay) with different volumetric water content (m_v) computed with Mironov et al. (2015), and the effective temperature of 300 K. Then we run the simulation just like in case of sea ice, assuming $PDF_\alpha \approx \exp(\alpha/s_\alpha)$ with s_α varying from 1° to 15° . This procedure is repeated for several values of the permittivity ϵ (imaginary part $\epsilon_{im} = 0$).

Figures 5.12 and 5.13 present H_α and Q_α , respectively, as a function of roughness for a range of permittivities. The intensity parameter H_α depends strongly on the angular characteristics of the T_B i.e. the Brewster angle and the spread between H and V polarizations. Those in turn are functions of the permittivity. Unlike H_α , Q_α varies little with changing ϵ , therefore Q_α mainly depends on surface slopes statistics rather than material properties.

The root mean square difference ($RMSD$) between the T_B s simulated with statistical roughness model and the T_B obtained from the simplified parametrization is shown in figure 5.14 as a function of surface permittivity. The $RMSD$ is highest for the low values of ϵ and decreases with increasing surface permittivity. It indicates that the simple parametrization captures better the polarization characteristic change for higher ϵ .

The relation between H_α and s_α depends on the surface permittivity. The bulk permittivity of sea ice simulated with the *MILLAS* model varies with ice temperature and salinity. The values likely to occur during Arctic conditions are confined between $\bar{\epsilon} = 3.1 + 0.05i$ (for $T=271$ K, $S_{ice}=7$ g kg $^{-1}$) and $\bar{\epsilon} = 4.6 + 0.8i$ (for $T=253$ K, $S_{ice}=1$ g kg $^{-1}$). For this interval little adjustment of H_α and Q_α is needed. Therefore we recommend the use of the **2p** parametrization introduced in the previous section for all first year ice types.

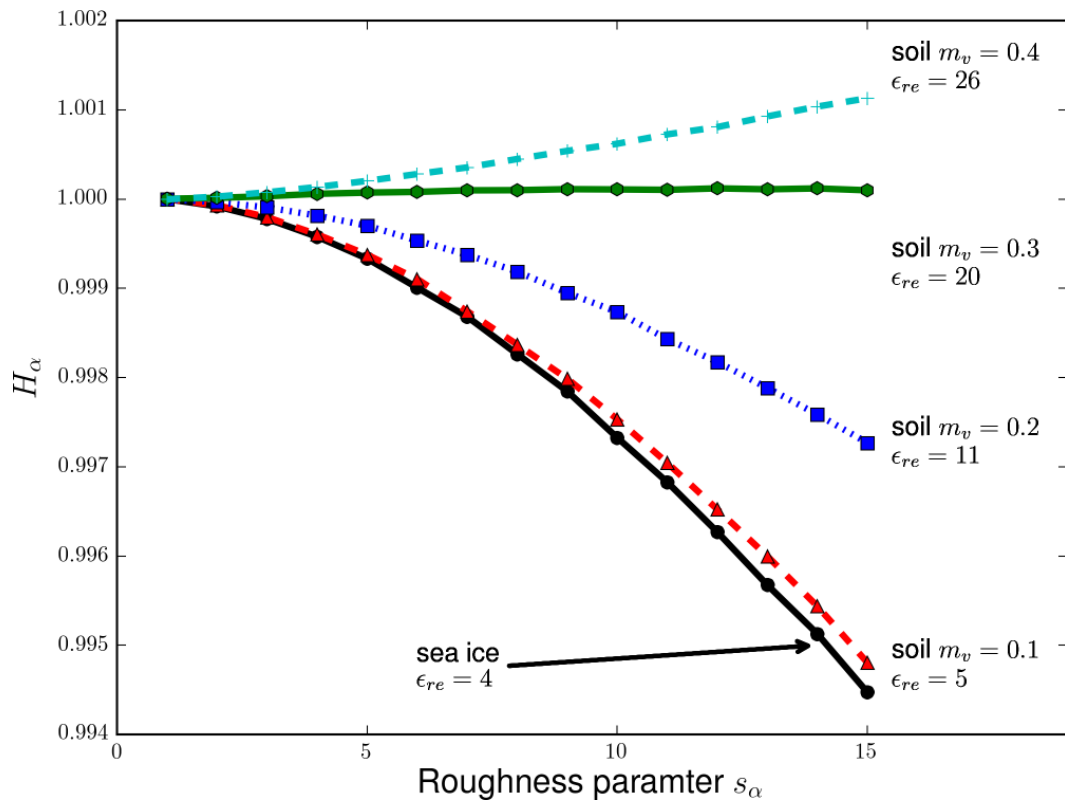


Figure 5.12: Parameter H_α as a function of roughness plotted for a range of permittivities.

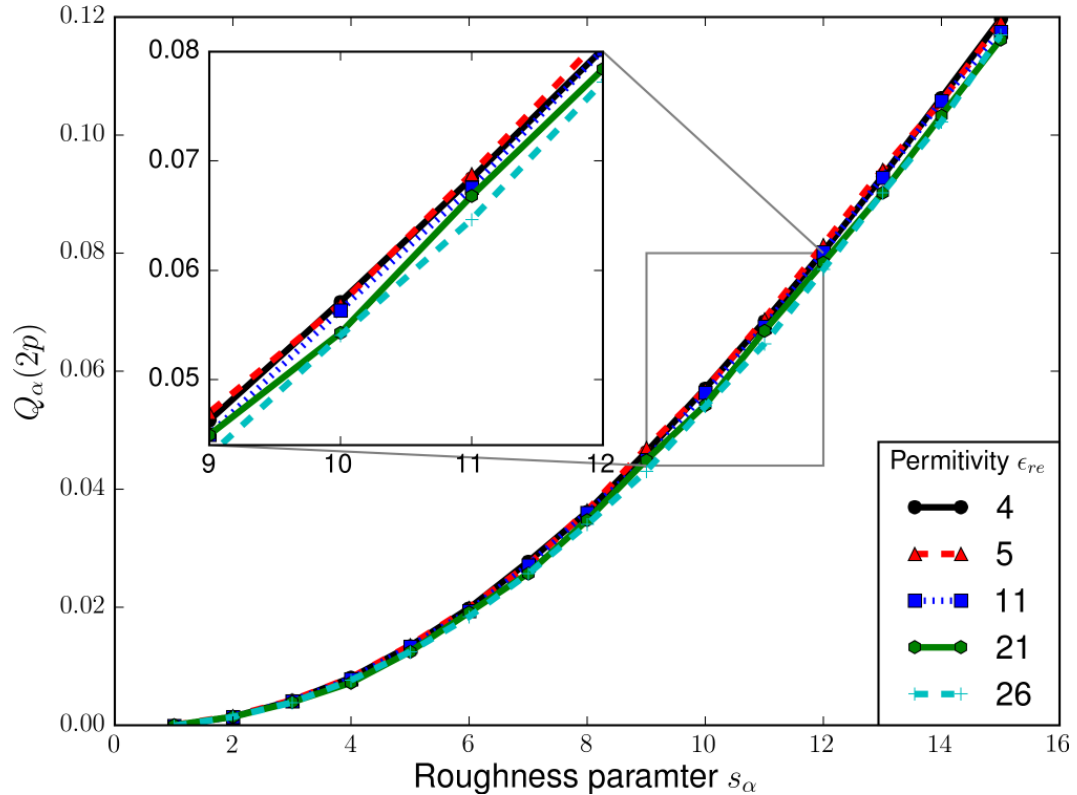


Figure 5.13: Parameter Q_α as a function of roughness plotted for a range of permittivities. (For the two-parameter parametrization schema)

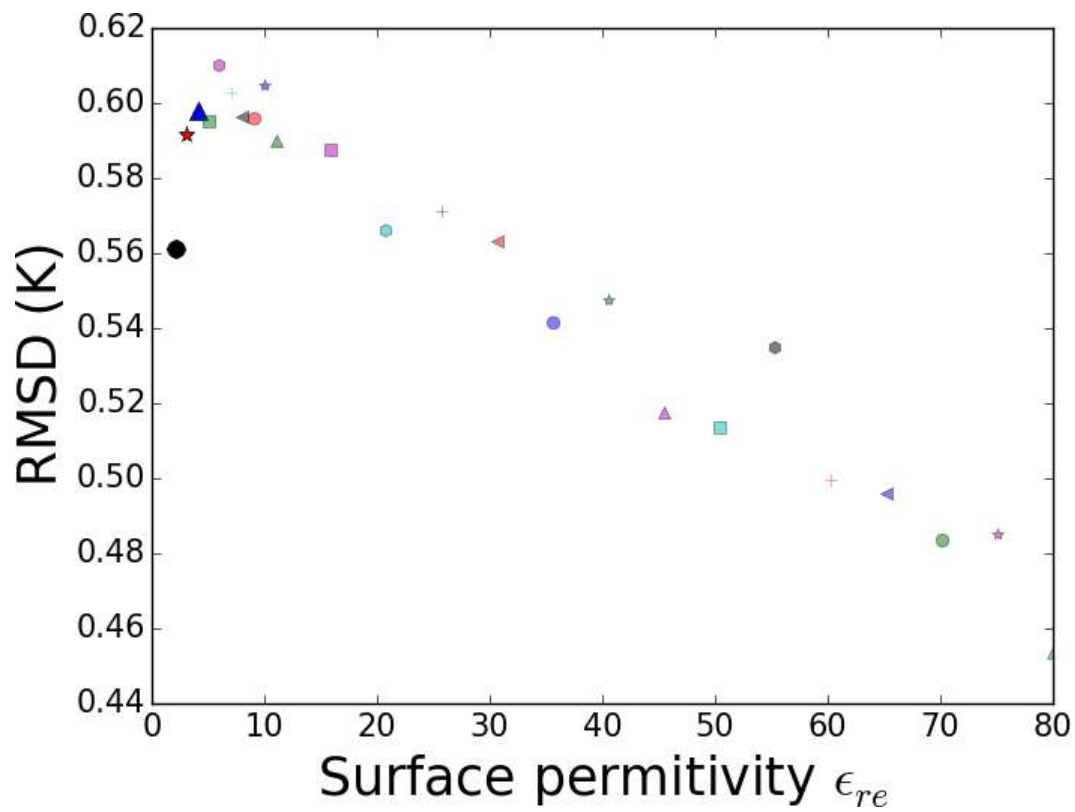


Figure 5.14: Root mean square difference between simulated with statistical roughness model T_{BS} and the simplified parametrization, for several values of surface permittivity. Colors and shapes correspond to permittivity values.

5.5 Summary and discussion

In this chapter, we have investigated two aspects of the brightness temperature (T_B) change caused by large scale surface roughness. The first one is the theoretical study involving the statistical roughness model initialized with sea ice roughness characteristics derived in chapter 4. We examined the magnitude of the T_B change and compared it with other prominent factors influencing the sea ice L-band emissions. The second aspect is the simple “fast model” parametrization of roughness effects on the T_B , which makes redundant the use of Monte Carlo simulations.

Brightness temperature over deformed sea ice.

For the simulation of sea ice T_B we used the *MILLAS* model with one layer of ice and one layer of snow equal to 10% of ice thickness. The model is initialized with surface temperature (T_{surf}), sea ice thickness (d_{ice}) and snow thickness (d_{snow}). The large scale surface roughness is included in a form of change in local incidence angles at multiple facets. The orientation of the facet with respect to the antenna look-angle is uniformly random in azimuthal direction and the facet slope is characterized by slope probability density function ($PDF_\alpha \approx \exp(-\alpha/s_\alpha)$). In the sensitivity study we also include the sea ice concentration C , which has to be considered during the uncertainty analysis of the roughness retrieval from radiometer data.

We choose the $T_B(0)$ and $T_B(H/V, 40)$ to measure the effect of the variations in model input parameters. The partial sensitivities can locally reach high values which are not indicative of real T_B uncertainties. We therefore constrain the parameter variations with uncertainty values specific to some satellite data. We take *Cryosat2* for a sea ice thickness uncertainty (we set $d_{snow} = 0.1 \cdot d_{ice}$), and *MODIS* for sea ice temperature and ice concentration uncertainty after Ivanova et al. (2015). We found that the sea ice concentration has a strongest effect for the simulated T_B s. The absolute changes in $T_B(0)$ and $T_B(H/V, 40)$ are about 7 K for the concentration variations of 5.3%. The overall result of decreasing C is the drop in total intensity and the increase in polarization difference of 1.3 K.

The variation in the other factors (T_{surf} , d_{ice} , d_{snow}) have non-monotonic sensitivities because of their interdependence in the thermodynamic part of the emissivity model. For that we made the uncertainty assessment for a thick ice in cold conditions ($T_{surf} = 253$ K, $d_{ice} = 1.42$ m, $d_{snow} = 0.14$ m), that represents the conditions encountered over “medium-deformed” ice. The thickness and temperature factors each make less than 1 K change in the investigated channels. Their influence is mainly on the total intensity, having little influence on the polarization difference.

As for the surface roughness, the strongest change is the reduction by of almost 3 K in vertical polarization at 40° , accompanied by a small increase (<0.2 K) in horizontal

T_B for the same incidence angle. Nadir T_B experiences a decrease of less than 1 K. These changes are calculated for the roughness parameter s_α varying from 0° to 15° . The pace of changes, however, increases with increase of s_α and is mostly pronounced in the vertical polarization resulting in polarization difference decrease.

When all the mentioned perturbations in the input data are included in the calculation (figure 5.8), the polarization difference in II^{nd} Stokes parameter ($T_B(V) - T_B(H)$) between “smooth ice” and “deformed ice” is 1.5 K. Such a small dynamic range makes the roughness types hard to distinguish in single *SMOS* measurement.

	$X \rightarrow$	$C(\%)$	$d_{ice}(\text{m})$	$d_{snow}(\text{m})$	$T_{surf}(\text{K})$	$s_\alpha(\text{deg})$
$\theta = 0^\circ$	$\partial T_B / \partial X$	1.47	0.73	5.7	0.14	-0.25
	ΔT_B	7.33	0.32	0.12	0.55	0.75
$\theta = 40^\circ$	$\partial T_B(H) / \partial X$	1.50	0.49	3.5	0.1	0.05
	$\Delta T_B(H)$	7.51	0.22	0.07	0.38	0.15
	$\partial T_B(V) / \partial X$	1.37	0.57	7.6	0.17	-0.31
	$\Delta T_B(V)$	6.83	0.25	0.15	0.69	2.87

Table 5.2: Table with partial sensitivities of the modeled brightness temperature to the variations in input parameters: C , d_{snow} , d_{ice} , T_{surf} , s_α . Rows labeled ΔT_B contain the brightness temperature change caused by “realistic” variation of input parameters. Partial sensitivities calculated with other values constant: $T_{surf} = 260$ K, $d_{ice} = 1.42$ m, $d_{snow} = 0.14$ m)

Table 5.2 contains the values of partial sensitivities of the T_B s to the model variables together with changes in T_B caused by perturbations in the input parameters within the “realistic ranges”.

Fast roughness model

A Monte Carlo simulation used for predicting the T_B characteristics of a rough surface is time consuming. For that reason we have developed a “Fast Roughness Model” (*FRM*) parametrization connecting the statistical model results directly to the T_B s of a smooth surface and surface roughness (s_α). The *FRM* is inspired by the semi-empirical *HQ - model* of Choudhury et al. (1979) and, likewise, it aims at capturing the change in emissions by introducing a factor for the change in the total intensity (H_α) and one responsible for polarization mixing (Q_α). Nonetheless, the physical mechanism behind it is different. The *HQ - model* deals with changes in reflectivity caused by small scale roughness. The *FRM* aims at capturing the purely geometric effect of multiple local incidence angles and their orientation.

As the *FRM* is focusing on the geometrical effects it can work with any kind of emissivity model. In section 5.4 we tested its application for different T_B polarization curves calculated with the Fresnel formula and for range of permittivities. The results indicate that the *FRM* can be extended to other surfaces provided that the corresponding $T_B^*(p/q, \theta)$ and PDF_α are given.

Chapter 6

The influence of surface roughness in the measured brightness temperature

In the previous chapter we have presented the statistical roughness model setup and studied its sensitivities to the input parameters. This chapter focuses on investigating the brightness temperature measured during the *SMOSice2014* campaign. We use the data from the campaign flights to test if the inclusion of surface roughness into T_B modeling leads to an improvement in the fraction of explained variance.

6.1 The emissivity model setup

In chapter 3 the **MI**crowave **L**-band **LA**yered **S**ea ice emission model (*MILLAS*) is presented. Emissivity model optimization was not an aim of this work, therefore we use a simple model setup that consists of four layers: air, snow, ice and water. Table 6.1 shows the values of the parameters characterizing the layers.

In the presented configuration the *MILLAS* model simulates the snow-covered sea ice brightness temperature as a function of ice thickness and surface temperature. The snow thickness d_{snow} is set to 10% of ice thickness d_{ice} . The snow is assumed to be dry, with a density of 300 kg/m^3 . The permittivities of snow and ice are linked to their temperature. A linear temperature gradient is assumed and the values of thermal conduction are as used in Maaß et al. (2013). We set the water salinity to 33 g/kg and the water temperature to 271.2 K .

Parameter		Value
Snow	surface temperature	measured (KT19)
	snow wetness	0%
	snow density	300 kg/ m ³
	snow thermal conductivity	0.31 W/(mK)
	snow thickness (d_{snow})	$0.1 \cdot d_{ice}$
Ice	ice thermal conductivity	$2.034 \text{ W}/(\text{mK}) + 0.13 \text{ W}/\text{m} \cdot S_{ice}(\text{g}/\text{kg})/T_{ice}(\text{K})$
	ice thickness (d_{ice})	measured (ALS)
	ice salinity (S_{ice})	4 g/kg
Water	water salinity	33 g/ kg
	water temperature	271.2 K

Table 6.1: Brightness temperature simulation setup used in *MILLAS* emission model.

6.2 Brightness temperature: modeled vs. measured

Following the introduction of the data set in chapter 2, we present the roughness parameter statistics derived from the digital elevation model (*DEM*). The surface roughness is well correlated with sea ice thickness, as illustrated in figure 6.1. The negative values of the thickness are attributed to measurement uncertainties over thin ice. The coefficient of determination is equal to $r^2 = 0.68$, and a simple least-square fit of a power function to the data is $s_\alpha(d_{ice}) = d_{ice}^{2.53}$. This result agrees with the findings of Petty et al. (2016), who observed a strong correlation between ice topography and ice thickness. The high correlation between s_α and d_{ice} might indicate that the surface deformation causes the unexpected increase in observed T_B .

Nonetheless, the change caused by the large scale surface roughness should have little effect on the near-nadir T_B . Our simulation predicts that a small negative difference of less than 1 K is to be expected for the heavy deformed ice. This is contradictory to the $T_B(0)$ increase with sea ice thickness of around 8 K/ m.

The positive trend observed in $T_B(0)$ from *EMIRAD2* over thick ice is not present in the co-located *SMOS* data (figure 6.2). The observations from space seem to confirm that $T_B(0)$ saturates over thick ice. It is important to note that the difference in footprint size of these measurements. The aircraft-mounted radiometer footprint is 70 m across and the data is averaged approximately every 4.3 km, whereas the *SMOS* nadir footprint is >30 km, as shown in chapter 3. Therefore the footprint heterogeneity must be considered. It is likely that different ice types, as well as open water and land are present within *SMOS* footprint.

An analogous comparison for the *EMIRAD2* side-looking antenna and *SMOS* is shown in the figure 6.3. This plot is made in Stokes parameters coordinates i.e. the sum

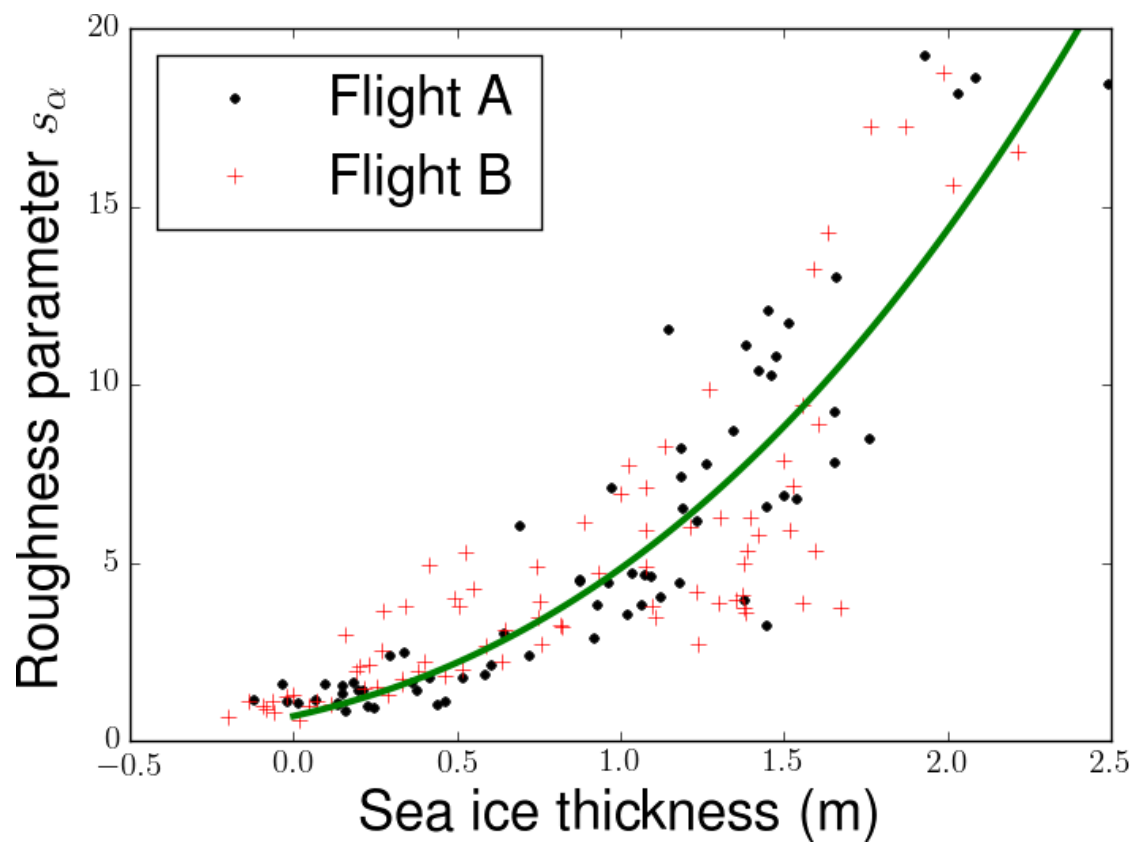


Figure 6.1: Surface roughness parameter s_α vs. sea ice thickness derived from *ALS*. The green curve fit equation: $s_\alpha(d_{ice}) = d_{ice}^{2.53}$

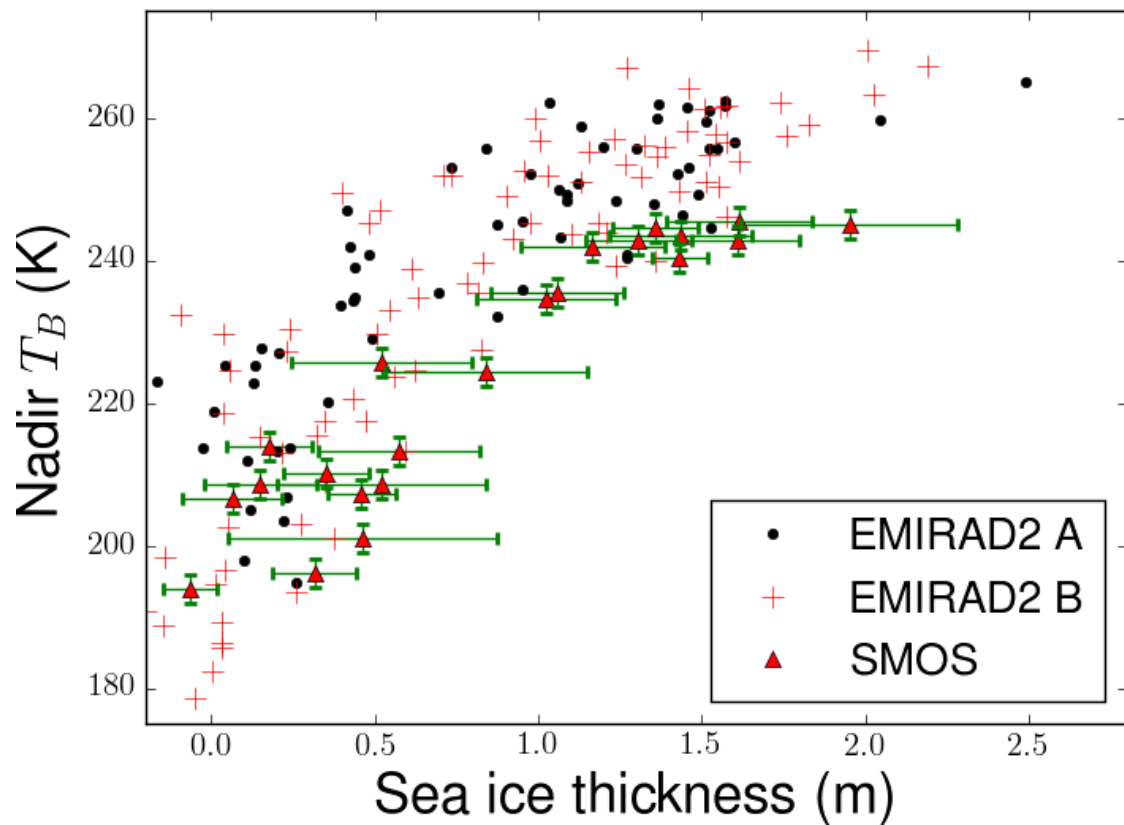


Figure 6.2: Near-nadir brightness temperatures from *EMIRAD2* and *SMOS* vs. sea ice thickness derived from *ALS*. Error bars mark the standard deviation of sea ice thickness measurements from *ALS* and *SMOS* radiometric accuracy.

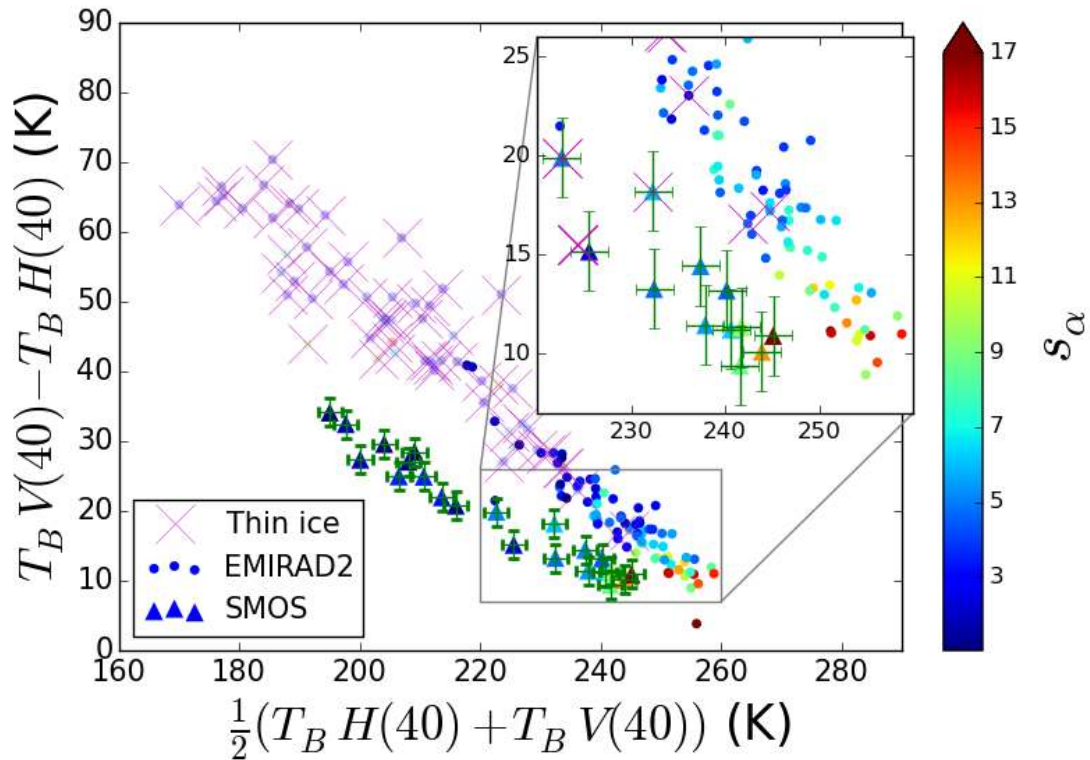


Figure 6.3: Polarization difference against mean intensity at 40° registered by *SMOS* and *EMIRAD2*. The color coding corresponds to the value of surface roughness parameter s_α . The points with corresponding mean sea ice thickness below 0.7 m are plotted in pale color.

and the difference of polarization channels. The color coding of the points corresponds to the roughness parameter computed over the respective footprints. The points of *SMOS* and *EMIRAD2* data are aligned along two lines with slightly different slopes.

We expect the strongest deformation over thick ice. Thus we are excluding the thin ice ($d_{ice} < 0.7$ m) from the analysis (crossed out in figure 6.3). The points attributed to the thick ice are displayed in the zoomed-in box in figure 6.3. The values of the total intensity (I^{st} Stokes) for the *EMIRAD2* are higher than for *SMOS*, just like in the case of the near-nadir antenna (fig. 6.2). The polarization difference in both data sets (II^{nd} Stokes) is comparable. Due to the *SMOS* footprint geometry and its size difference in comparison with *EMIRAD2*, we cannot single out the effect of surface roughness.

Until this point, it may appear that we cannot observe the surface roughness in the *SMOSice2014* data. In the studied region we have only a handful (8) of independent *SMOS* measurements, the effect of surface roughness is small compared with the one of sea ice concentration and land contamination (up to 25% of the footprint, not shown). Furthermore, the increase in *EMIRAD2* nadir T_B cannot be explained with large scale surface roughness. However, we have to also analyze the data from the side-looking

antenna. The limitation of this approach is that we assume the ice observed at 40° angle and the ice below the flight path as having the same properties.

We consider the surface temperature, the sea ice thickness and the surface roughness along the flight and we use them to run the statistical roughness model with a single ice layer *MILLAS* setup as the brightness temperature module. The snow thickness is set to be 10% of the sea ice thickness. The calculation is done for 60 s averages.

We simulate the T_B of the *EMIRAD2* channels (nadir, side *H/V* polarizations). For each channel we made four simulation setups, two without roughness: Flat no-snow, Flat snow, and two with roughness included: Rough no-snow, Rough snow. As for the performance metrics of the model setups, we use the coefficient of determination (r^2), the root-mean-square error (*RMSE*), the bias and unbiased root-mean-square error (*ubRMSE*). These metrics are widely used in the assessment of performance of satellite measurements (Entekhabi et al., 2010). Table 6.2 holds the results of the comparison expressed in terms of r^2 , *RMSE*, *bias* and *ubRMSE*.

		r^2	<i>RMSE</i> (K)	<i>bias</i> (K)	<i>ubRMSE</i> (K)
$T_B, \theta = 0^\circ$	Flat, no snow	0.21	30.9	12.6	27.8
	Flat, snow	0.29	26.1	1.3	26.7
	Rough, no snow	0.20	30.8	12.5	27.8
	Rough, snow	0.29	26.2	1.5	26.1
$T_{BH}, \theta = 40^\circ$	Flat, no snow	0.22	29.9	4.6	29.5
	Flat, snow	0.30	30.3	-13.2	27.3
	Rough, no snow	0.22	29.8	4.5	29.4
	Rough, snow	0.30	30.3	-13.2	27.3
$T_{BV}, \theta = 40^\circ$	Flat, no snow	0.16	29.1	4.0	28.9
	Flat, snow	0.24	27.2	-1.9	27.1
	Rough, no snow	0.15	29.3	5.0	28.9
	Rough, snow	0.22	27.1	-1.2	27.1

Table 6.2: Performance of the different T_B simulation setups in terms of coefficient of determination (r^2), *RMSE*(K), *bias*(K), *ubRMSE*(K). For *EMIRAD2* channels four model setups are tested: Flat no snow, Flat snow, Rough no snow, Rough snow. Nadir-looking antenna channels are treated together.

The values of r^2 for all channel - setup combinations do not exceed 0.3. The simplified one-layer model managed to capture only 30% of the signal variance even

with surface roughness included. Furthermore, the inclusion of surface roughness brings little improvement to the statistics. In case of vertical polarization, where the model studies indicate the most sensitivity to roughness, the r^2 is even worse. Our very crude snow thickness parametrization is more successful in capturing the radiometer measurements variability. Also, all metrics show the four model setups perform poorly in reproducing the *EMIRAD2* measurements. The *bias* is lowest for the side-looking vertical channel (-1.9 K to 5 K). For nadir channel the inclusion of snow in the model reduces the *bias* by 11 K to the value of 1.5 K. For the horizontal polarization channel the inclusion of snow has an opposite effect, changing the absolute value of *bias* from 4.5 K to -13.2 K. The high values of *RMSE* and *ubRMSE* show a general miss-fit of the model to the data.

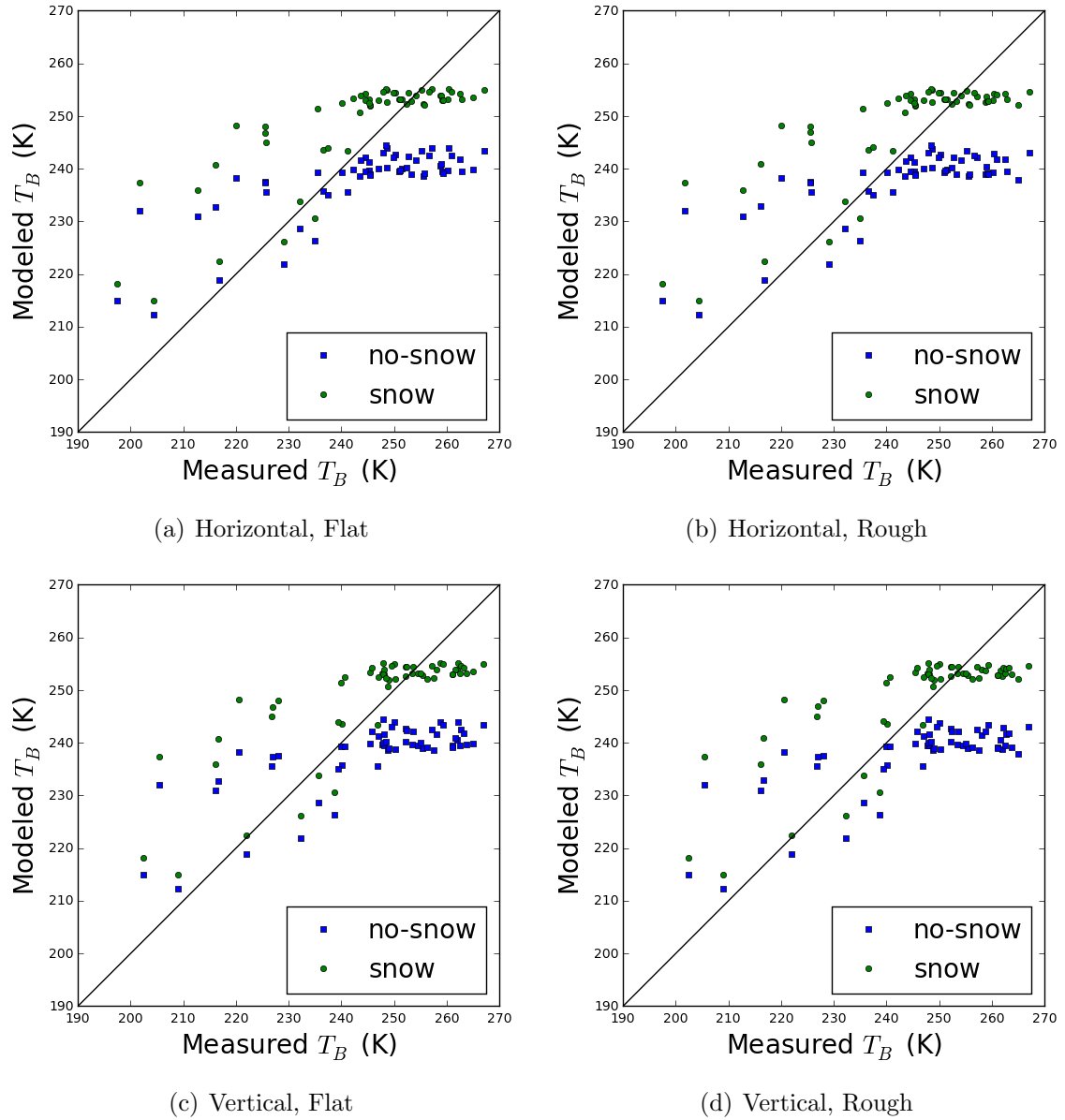
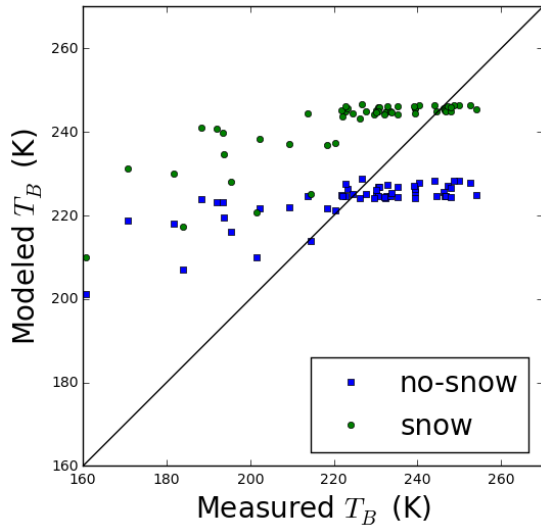
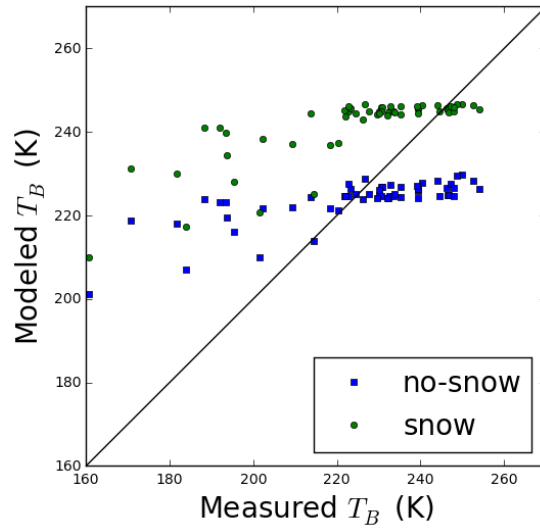


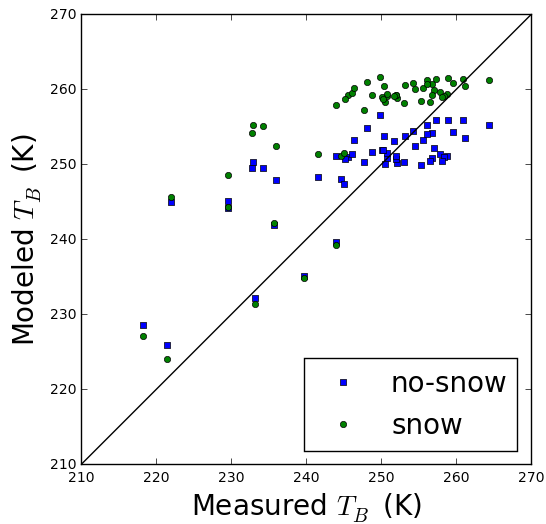
Figure 6.4: Scatterplots of modeled vs. measured brightness temperature for the **nadir-looking** *EMIRAD2* antenna channels ($\theta = 0^\circ$). The T_B s are averaged over 60 s. The simulations including geometrical roughness are placed in the right column. Flights **A** and **B** are combined.



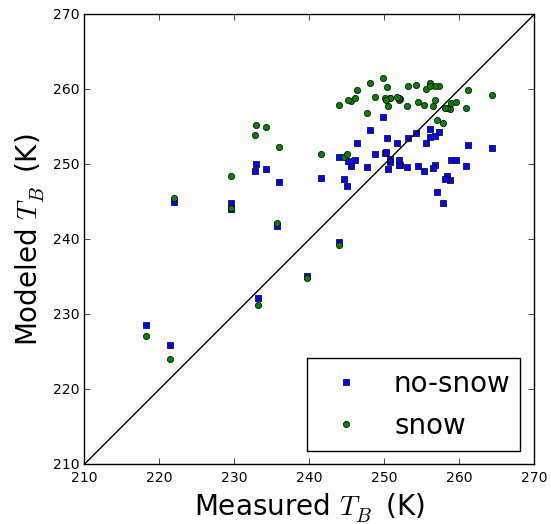
(a) Horizontal, Flat



(b) Horizontal, Rough



(c) Vertical, Flat



(d) Vertical, Rough

Figure 6.5: Scatterplots of modeled vs. measured brightness temperature for the **side-looking** *EMIRAD2* antenna channels ($\theta = 40^\circ$). The T_B s are averaged over 60 s. The simulations including geometrical roughness are placed in the right column. Flights **A** and **B** are combined.

6.3 Summary and discussion

In this chapter we have investigated the brightness temperature measured by *SMOS* and *EMIRAD2* in the region of Barents Sea covered by *SMOSice2014* campaign.

The increase in near-nadir T_B over thick ice is only present in the *EMIRAD2* data. Due to the footprint size differences such comparison is far from conclusive (the time difference is less than 6h). It is possible that the large *SMOS* footprint captures open water or thin ice, which decrease the T_B . If the lower *SMOS* T_B is caused by open water or thin ice beyond the *EMIRAD2* field of view, we should also observe an increase in polarization difference. However, as shown in figure 6.3, the polarization difference for the points with comparable roughness remains at the same level for both radiometers. It is a puzzling result which encouraged us to take a deeper look into radiometer data along the flight tracks.

During the campaign flights the sea ice thickness, surface temperature and surface elevation were co-registered with the T_B . We used those variables to simulate the sea ice T_B with *MILLAS* and the corresponding slopes statistics ($PDF_\alpha(s_\alpha)$). The roughness parameter s_α is highly correlated ($r^2 = 0.68$) with sea ice thickness (fig. 6.1). This can be intuitively explained by the fact that the thick ice in the region was formed by dynamic processes which also influenced the surface roughness.

We evaluated four model setups in terms of the percent of the explained variance in the radiometer data at nadir and at 40° H/V channels (tab. 6.2). All setups are clearly imperfect failing to reproduce more than 30% of the total variance. We observe that including snow adds 7 to 10% to the explained variance. The surface roughness accounts for up to 1% improvement in the nadir and the $T_B H(40)$ explained variance. In case of vertical polarization the inclusion of roughness has an opposite effect: it lowers the result by 1 to 4%. Regardless of the r^2 , the large values of *RMSE* show that the simple model setup reproduces poorly the measured T_B s.

Our hypothesis that the large scale surface roughness causes the ≈ 8 K/m increase in T_B is not supported by the theoretical study of the geometrical effects related to the change of local incidence angle. The roughness parameter s_α is highly correlated with sea ice thickness, but simulations with the statistical roughness model suggest little change in the nadir T_B . The most pronounced effect is predicted for the vertical polarization. The comparison with field data indicates that roughness is a less important factor than snow cover. Based on modeling results and field measurements we conclude that large scale (geometrical) surface roughness is not responsible for the observed increase in the nadir T_B of thick ice.

Chapter 7

Summary and conclusions

In this study we have investigated the effect of surface roughness on the L-band brightness temperature of sea ice. We have used a combination of field measurements from the *SMOSice2014* campaign, satellite observations from *SMOS* and radiative transfer model *MILLAS* simulations. We have focused on the large scale surface roughness, as sea ice is electromagnetically smooth for L-band radiation on the scale of 0.25 m (Landy et al., 2015; Ulaby et al., 2014, pp.427). The studies with finite element models (*FEM*) show that a domain of $8\lambda \times 8\lambda$ is large enough for the scattering simulations involving small scale roughness (Lawrence et al., 2013). This leaves the larger scales to be characterized with geometrical optics. The airborne laser scanner (*ALS*) data used in this study measured surface elevation with 0.5×0.25 m resolution. The derived from the interpolated *ALS* data digital elevation model (*DEM*) has a resolution of 1 m. For L-band the electromagnetic wavelength in sea ice is ≈ 0.12 m ($\lambda_{ice} = \lambda/\sqrt{\epsilon}$). Thus, our *DEM* is suitable for characterizing the large scale roughness.

In chapter 4, we have presented the sea ice classification based on aerial photography. We made an analysis of surface roughness encountered over three ice classes: “smooth”, “medium-deformed”, “deformed” ice. The three ice types differ significantly. “Smooth” ice has a thickness of 0.08 ± 0.23 m and without elevated surface features can be treated as a specular surface. The thicknesses of “medium-deformed” and “deformed” ice are 1.42 ± 0.25 m and 1.90 ± 0.97 m, respectively. We found that the correlation function is best characterized by an exponential function.

The core section of chapter 4 covers the surface slopes statistics. We derive surface slopes (α) and their orientation (γ) from the *DEM*. We found that probability density functions of surface slopes (PDF_α) can be parametrized with an exponential function. The shape of the $PDF_\alpha \approx \exp(-\alpha/s_\alpha)$ is characterized by s_α . We use the s_α as a roughness parameter, characterizing the large scale surface roughness. The “medium-deformed” and “deformed” ice have s_α values of 8° and 15° , respectively. Unlike previous studies we have not assumed the isotropic distribution of γ . Instead, we have evaluated the deviation from the isotropic distribution along 1000 random

samples from the flight track. On average the PDF_γ was isotropic on a scale greater than 4.3 km, which corresponds to approximately 60 s of flight time.

In chapter 5, we used the PDF_α to simulate a rough surface with the Monte Carlo method. We varied the roughness parameter s_α from 0° to 15° in order to obtain faceted surfaces with different degrees of roughness. For each of the surfaces we have computed the sum of emissions from the facets at horizontal and vertical polarizations. The computation was done under the assumption of a constant antenna gain and for the case of far field (Constant antenna look-direction.) Further, we have parametrized the results of the Monte Carlo simulations with a “fast roughness model”.

In chapter 6, we compared the *EMIRAD2* and *SMOS* radiometer data with brightness temperature simulations done with our statistical roughness model. The comparison was done with values averaged every 60 s. For the input parameters we used the surface temperature measured by *KT19*, the sea ice thickness and the PDF_α from *ALS*. As for the snow thickness, we used an approximate formula relating it to sea ice thickness: $d_{snow} = 0.1 \cdot d_{ice}$.

7.1 Back to the research questions

The results presented in the chapters 5, 4 and 6 enabled us to address the main research questions posed in the introduction to this work.

How are the angular T_B characteristics changing with increasing roughness of the sea ice surface?

An increase in large scale surface roughness results in a change in T_B angular characteristics. The most pronounced effect is the decrease in vertical polarization, which for a deformed ice can reach up to 8 K close to the Brewster angle. Changes in horizontal polarization range from a small decrease (≈ 1 K) for incidence angles $< 40^\circ$ to 4 K increase at 60° . The nadir T_B decreases monotonically with increasing roughness. For the deformed ice the change in $T_B(0)$ is less than 1 K. The changes in angular $T_B(H/V)$ can be expressed as a superposition of two effects: the change in total intensity (H_α) and polarization mixing (Q_α) equation 5.2. The “fast roughness model” expresses the H_α , Q_α as a function of slope distribution parameter s_α . The exact formula for $H_\alpha(s_\alpha)$, $Q_\alpha(s_\alpha)$ depends on PDF_α and shape of $T_B^*(p/q)$. The latter is a function of permittivity. This approach can be used to characterize the $T_B(\theta)$ for a variety of surfaces if a corresponding emissivity model and PDF_α are provided. In the case of sea ice ($\epsilon < 5$), the large scale surface roughness is not a cause of the observed increase in nadir T_B over thick ice.

What is the magnitude of the T_B changes due to roughness in comparison with other factors?

To evaluate the magnitude of T_B changes we considered as metrics the values at incidence angles of $\theta = 0^\circ$ and $\theta = 40^\circ$. The partial sensitivities to the model parameters can locally reach very high values. For that reason we have constrained the sensitivity analysis to a “realistic case”, where the model input variables (C , d_{ice} , d_{snow} , T_{surf}) are constrained with satellite product uncertainties. The analysis was done for a case of thick ice ($d_{ice} > 0.7$ m) where the greatest variability of surface roughness is to be expected. As shown in figure 5.7 the sea ice concentration uncertainty results in around 7 K decrease in T_B channels under investigation. The decrease in $T_B(V, 40)$ of 2.8 K resulting from surface roughness change (s_α from 0° to 15°) is the only other contribution of surface roughness that exceeds 1 K. The relatively high sensitivity is promising for the surface roughness retrieval (see figure 5.8).

However, it is important to note the limitations of the used method. The first limitation is the assumption of one ice type within the radiometer footprint, whereas in nature one can expect several ice types of different thickness and emissivities. The second limitation is the set of assumption in the emissivity model: as a goal of this work is to characterize the large scale geometrical roughness, we took the simplest four-layer setup for the *MILLAS* model to compute the ice emissivities. Furthermore, we parametrize the thickness of snow with ice thickness. Additionally we assumed that the side looking antenna of *EMIRAD2* is observing the same ice conditions as the nadir one and the *ALS*. These factors contribute to the mismatch between the observed and simulated brightness temperature for the *SMOSice2014* campaign. We have tested four different model setups to simulate the T_B of the *EMIRAD2* channels. The setups involved combinations of surface roughness and snow cover: Flat no-snow, Flat snow, Rough no-snow, Rough snow. The results of the comparison are to be found in table 6.2. The high root-mean-square error (values of ≈ 28 K) for all setups indicate poor model fitting. As far as the r^2 is concerned, i.e. the fraction of explained variance, an inclusion of surface roughness in the simulation brings little improvement (from -0.01 to 0.005). On the other hand, the inclusion of snow adds 7-8% of explained variance.

To conclude, the surface roughness reveals itself strongest in the vertical T_B . But in order to distinguish its effect from the other factors a more sophisticated emissivity model is needed. Another possible improvement might come from the direct simulation of surface facet orientation instead of the PDF_α .

Is it possible to measure the sea ice deformation with multi-angular *SMOS* data?

The question if *SMOS* multi-angular brightness temperatures can be used for the detection of sea ice deformation remains open. Our model studies indicate that the vertical polarization at high incidence angle $\approx 50^\circ$ is most affected by the surface roughness (8K). In order to take advantage of this effect in detecting the sea ice deformation two main issues have to be addressed. The first is the lack of an appropriate validation data set. During the *SMOSice2014* the *ALS* data covered only a small fraction of heterogeneous *SMOS* footprints. Furthermore we had only few independent *SMOS* measurements in the region, and of them the ones contain the most deformed ice were contained significant land fraction (8-25%). The second issue, as shown in Chapters 5 and 6, is the accurate representation of snow cover, ice thickness and all other factors influencing the T_B , as these are crucial for the detection of ice deformation from *SMOS*. For example, using a region of deformed ice such as Lincoln Sea for studying the surface roughness has its limitations, mainly because that little is known about the permittivity and snow cover.

Appendix A

Coordinates of the identified ice types

In this work we used aerial photography to identify ice types with distinct surface roughness features. Tables with the coordinates of the scenes by ice type:

Smooth ice				Med.-deformed ice		Deformed ice			
Latitude	Longitude	Latitude	Longitude	Latitude	Longitude	Latitude	Longitude	Latitude	Longitude
78.0858	27.5043	78.5508	29.3776	78.1972	24.6744	78.2476	23.0417	78.2549	23.0853
78.0857	27.5072	78.551	29.3808	78.1972	24.6773	78.2475	23.0448	78.2551	23.0883
78.0856	27.5101	78.5511	29.384	78.1971	24.6802	78.2474	23.048	78.2553	23.0913
78.0854	27.513	78.5513	29.3872	78.197	24.6832	78.2474	23.0512	78.2555	23.0943
78.0853	27.5159	78.5514	29.3904	78.1969	24.6861	78.2473	23.0544	78.2557	23.0973
78.0851	27.5188	78.5516	29.3936	78.1968	24.6891	78.2473	23.0576	78.2558	23.1002
78.085	27.5216	78.5516	29.3969	78.1967	24.692	78.2472	23.0608	78.256	23.1032
78.0849	27.5245	78.5518	29.4001	78.1966	24.695	78.2471	23.064	78.2562	23.1062
78.0847	27.5274	78.552	29.4032	78.1965	24.6979	78.2471	23.0672	78.2564	23.1092
78.0846	27.5303	78.5521	29.4065	78.1964	24.7009	78.247	23.0704	78.2566	23.1122
78.0845	27.5332	78.5522	29.4096	78.2049	24.4712	78.247	23.0735	78.2568	23.1152
78.0843	27.5361	78.5523	29.4128	78.2048	24.474	78.2469	23.0767	78.2569	23.1182
78.0842	27.539	78.5525	29.4161	78.2047	24.4768	78.2469	23.0798	78.2571	23.1212
78.0841	27.542	78.5526	29.4195	78.2046	24.4797	78.2468	23.083	78.2573	23.1242
78.084	27.5449	78.5528	29.4228	78.2045	24.4826	78.2468	23.0862	78.2575	23.1272
78.0839	27.5478	78.5529	29.426	78.2044	24.4854	78.1881	24.9355	78.2576	23.1303
78.0837	27.5508	78.5531	29.4293	78.2043	24.4883	78.188	24.9384	78.2578	23.1332
78.0836	27.5537	78.5532	29.4325	78.2042	24.4911	78.1879	24.9413	78.258	23.1363
78.0835	27.5567	78.5534	29.4358	78.2041	24.494	78.1878	24.9442	78.2582	23.1393
78.0834	27.5597	78.5535	29.4391	78.204	24.4968	78.1877	24.9471	78.2584	23.1424
78.0833	27.5627	78.5537	29.4424	78.2038	24.4997	78.1876	24.95	78.2585	23.1454
78.0832	27.5656	78.5539	29.4456	78.2037	24.5025	78.1875	24.9529	78.2587	23.1485
78.0831	27.5686	78.554	29.4489	78.2036	24.5053	78.1874	24.9558	78.2589	23.1515
78.083	27.5716	78.5542	29.4521	78.2035	24.5081	78.1873	24.9587	78.2591	23.1546
78.0821	27.5924	78.5544	29.4554	78.2034	24.511	78.1872	24.9615	78.2592	23.1577
78.082	27.5954	78.5544	29.4588	78.3655	25.0611	78.1954	24.7332	78.2594	23.1607
78.0819	27.5983	78.5546	29.462	78.3656	25.0641	78.1953	24.7362	78.2596	23.1638
78.0818	27.6013	78.5547	29.4653	78.3658	25.0672	78.1952	24.7391	78.2598	23.1668
78.0817	27.6042	78.5548	29.4687	78.3659	25.0703	78.1951	24.7421	78.26	23.1698
78.0816	27.6072	78.5583	30.4634	78.3661	25.0734	78.195	24.745	78.2601	23.1728
78.0815	27.6102	78.5884	30.4666	78.3663	25.0765	78.1949	24.748	78.2656	23.2649
78.0814	27.6132	78.5885	30.4698	78.3664	25.0796	78.1948	24.7509	78.2658	23.2679
78.0812	27.6161	78.5886	30.473	78.3666	25.0826	78.1947	24.7538	78.2659	23.2708
78.0811	27.6191	78.5887	30.4762	78.3667	25.0857	78.1946	24.7568	78.2661	23.2737
78.081	27.6221	78.5889	30.4792	78.3669	25.0888	78.1945	24.7597	78.2663	23.2767
78.0809	27.625	78.589	30.4824	78.3671	25.0919	78.1944	24.7626	78.2664	23.2797
78.0808	27.628	78.5891	30.4857	78.3672	25.095	78.1943	24.7655	78.2667	23.2826
78.0807	27.631	78.5892	30.4889	78.3674	25.0981	78.1942	24.7684	78.2668	23.2855
78.0806	27.634	78.5893	30.4922	78.3675	25.1012	78.1941	24.7712	78.267	23.2884
78.0805	27.6369	78.5894	30.4954	78.3677	25.1042	78.194	24.7741	78.2673	23.2913
78.0804	27.6399	78.5896	30.4987	78.3678	25.1073	78.1939	24.777	78.2674	23.2943

Smooth ice			
Latitude	Longitude	Latitude	Longitude
78.0803	27.6429	78.5897	30.502
78.0802	27.6458	78.5898	30.5053
78.0801	27.6488	78.5899	30.5086
78.0799	27.6517	78.59	30.5119
78.0798	27.6546	78.5901	30.5152
78.0797	27.6575	78.5903	30.5185
78.0796	27.6605	78.5904	30.5218
78.0795	27.6634	78.5905	30.525
78.0794	27.6663	78.5905	30.5284
78.0792	27.6692	78.5908	30.5317
78.0791	27.6721	78.5909	30.535
78.079	27.6751	78.591	30.5383
78.0789	27.678	78.5911	30.5416
78.5471	29.2765	78.5912	30.5449
78.5473	29.2831	78.5914	30.5515
78.5474	29.2865	78.5914	30.5547
78.5475	29.2898	78.5915	30.558
78.5477	29.293	78.5916	30.5613
78.5478	29.2963	78.5918	30.5645
78.5479	29.2996	78.5918	30.5679
78.548	29.3028	78.5919	30.5712
78.5481	29.3061	78.592	30.5744
78.5483	29.3093	78.5921	30.5777
78.5484	29.3126	78.5922	30.581
78.5485	29.3158	78.5923	30.5842
78.5486	29.319	78.5924	30.5875
78.5487	29.3223	78.5925	30.5909
78.5488	29.3256	78.5926	30.5942
78.5489	29.3288	78.5926	30.5975
78.5491	29.3321	78.5927	30.6008
78.5492	29.3354	78.5928	30.6042
78.5493	29.3386	78.5929	30.6075
78.5494	29.3418	78.593	30.6109
78.5496	29.3451	78.5931	30.6142
78.5497	29.3484	78.5932	30.6175
78.5499	29.3515	78.5933	30.6209
78.5501	29.3547	78.5934	30.6243
78.5501	29.358	78.5935	30.6276
78.5503	29.3612	78.5936	30.6309
78.5503	29.3646	78.5937	30.6343
78.5505	29.3677	78.5937	30.6376
78.5505	29.3711	78.5939	30.641
78.5507	29.3743	78.594	30.6443
78.5949	30.6707	78.5941	30.6476
78.595	30.674	78.5942	30.6509
78.5951	30.6773	78.5943	30.6543
78.5954	30.6804	78.5944	30.6575
78.5956	30.6836	78.5945	30.6608
78.5958	30.6869	78.5946	30.6642
78.596	30.6901	78.5947	30.6674
78.5967	30.6937	78.5964	30.6966

Med.-deformed ice	
Latitude	Longitude
78.368	25.1104
78.3681	25.1135
78.3683	25.1165
78.3684	25.1196
78.3686	25.1227
78.3687	25.1257
78.3689	25.1288
78.369	25.1318
78.3692	25.1349
78.3693	25.1379
78.3694	25.141
78.3696	25.144
78.3697	25.1471
78.3698	25.1502
78.3883	25.5267
78.3885	25.5297
78.3886	25.5328
78.3888	25.5358
78.3889	25.5389
78.3891	25.5419
78.3892	25.545
78.3894	25.548
78.3896	25.551
78.3897	25.554
78.3899	25.5571
78.39	25.5601
78.3902	25.5631
78.3903	25.5662
78.3905	25.5692
78.3907	25.5723
78.3908	25.5754
78.391	25.5785
78.3912	25.5816
78.3913	25.5847
78.3915	25.5878
78.3917	25.5909
78.3918	25.594
78.392	25.5971
78.3922	25.6002
78.3924	25.6033
78.3925	25.6064
78.3927	25.6095
78.3929	25.6126

Deformed ice			
Latitude	Longitude	Latitude	Longitude
78.1938	24.7798	78.2676	23.2972
78.1937	24.7827	78.2678	23.3002
78.1936	24.7856	78.2679	23.3031
78.1935	24.7884	78.2681	23.306
78.1934	24.7913	78.2683	23.309
78.1933	24.7942	78.2685	23.3119
78.1932	24.7971	78.2686	23.3149
78.1931	24.7999	78.2688	23.3178
78.193	24.8028	78.269	23.3207
78.1929	24.8057	78.2691	23.3237
78.1928	24.8086	78.2693	23.3266
78.1927	24.8114	78.2695	23.3296
78.1926	24.8143	78.2696	23.3326
78.1925	24.8172	78.2698	23.3355
78.2493	22.9993	78.2701	23.3415
78.2495	23.0023	78.2703	23.3444
78.2497	23.0053	78.2705	23.3474
78.2499	23.0083	78.2706	23.3504
78.2501	23.0112	78.2708	23.3533
78.2503	23.0142	78.271	23.3563
78.2505	23.0172	78.2711	23.3593
78.2507	23.0201	78.2713	23.3623
78.2509	23.0231	78.2715	23.3653
78.2511	23.0261	78.2717	23.3682
78.2513	23.029	78.2718	23.3712
78.2514	23.032	78.272	23.3742
78.2516	23.0349	78.2722	23.3772
78.2518	23.0378	78.2723	23.3801
78.252	23.0408	78.2725	23.3831
78.2522	23.0437	78.2727	23.3861
78.2524	23.0467	78.2728	23.3891
78.2526	23.0496	78.273	23.392
78.2528	23.0526	78.2732	23.395
78.253	23.0556	78.2734	23.3978
78.2532	23.0585	78.2735	23.4009
78.2534	23.0615	78.2737	23.4038
78.2536	23.0645	78.2739	23.4069
78.2538	23.0674	78.2741	23.4098
78.254	23.0704	78.2742	23.4127
78.2542	23.0734	78.2744	23.4157
78.2543	23.0764	78.2746	23.4186
78.2545	23.0793	78.2747	23.4217
78.2547	23.0823	78.2749	23.4245
78.3086	24.028	78.2751	23.4275
78.3088	24.0309	78.2753	23.4304
78.309	24.0338	78.2755	23.4334
78.3091	24.037	78.2756	23.4364
78.3092	24.0401	78.2758	23.4393
78.3093	24.0431	78.276	23.4423
78.3094	24.0461	78.2762	23.4453
78.3095	24.0492	78.2764	23.4483
78.3096	24.0523	78.2766	23.4513
78.3097	24.0553	78.2768	23.4543
78.3099	24.0584	78.277	23.4573
78.31	24.0614	78.2772	23.4603

Appendix B

Atmospheric corrections

In this work we used a simplified model allowing for atmospheric corrections in L-band, as used in SMOS sea surface salinity prototype processor (Zine et al., 2008). The atmospheric attenuation and emissions are described as:

$$k_{atm} = k_{O_2} + k_{H_2O} \quad (B.1)$$

$$T_{B,atm} = T_{B,O_2} + T_{B,H_2O} \quad (B.2)$$

$$T_{B,X} = (T_0 - \Delta T_X)k_X \quad (B.3)$$

where X stand for H_2O or O_2 .

$$k_{O_2} = \frac{a_0 + a_1T_0 + a_2P_0 + a_3T_0^2 + a_4P_0^2 + a_5T_0P_0}{\cos \theta} 10^{-6} \quad (B.4)$$

$$\Delta T_{O_2} = b_0 + b_1T_0 + b_2P_0 + b_3T_0^2 + b_4P_0^2 + b_5T_0P_0 \quad (B.5)$$

$$k_{H_2O} = \max \left(\frac{c_0 + c_1P_0 + c_2WVC}{\cos \theta} 10^{-6}, 0 \right) \quad (B.6)$$

$$\Delta T_{H_2O} = d_0 + d_1P_0 + d_2WVC \quad (B.7)$$

where P_0 is the surface pressure in hPa, T_0 is surface temperature in K and WVC is the total precipitable water-vapor content.

Coefficient	Value	Units
a_0	8.03325×10^{-3}	neper
a_1	-1.03999×10^{-2}	neper \cdot K ⁻¹
a_2	2.82992×10	neper \cdot hPa ⁻¹
a_3	2.62584×10^{-1}	neper \cdot K ⁻²
a_4	6.43081×10^{-3}	neper \cdot hPa ⁻²
a_5	-9.42431×10^{-2}	neper \cdot K ⁻¹ \cdot hPa ⁻¹
b_0	-7.78882×10^{-1}	K
b_1	1.37576×10^{-1}	dimensionless
b_2	-1.14919×10^{-3}	K \cdot hPa ⁻¹
b_3	-1.15781×10^{-4}	K ⁻¹
b_4	1.28474×10^{-6}	K \cdot hPa ⁻²
b_5	-1.11330×10^{-5}	hPa ⁻¹
c_0	-1.47866×10^{-2}	neper
c_1	1.50999×10^{-1}	neper \cdot hPa ⁻¹
c_2	3.75477	neper \cdot m ² \cdot kg ⁻¹
d_0	8.18092	K
d_1	2.79377×10^{-4}	K \cdot hPa ⁻¹
d_2	3.72190×10^{-2}	K \cdot m ² \cdot kg ⁻¹

Figure A.1: Table with parameter values used in atmospheric correction. Taken from Zine et al. (2008).

Acronyms and symbols

<i>ALS</i>	Airborne laser scanner
<i>AMSR – E</i>	Advanced Microwave Scanning Radiometer onboard EOS
α	angle of the facet slope
<i>C</i>	sea ice concentration
<i>CDF</i>	Cumulative probability distribution function
δ_{ALS}	elevation measurement accuracy
$\Delta\mathbf{x}$	sampling distance
<i>e</i>	emissivity
<i>ESA</i>	European Space Agency
ϵ	permittivity
γ	azimuth angle of the facet orientation
Γ	surface reflectivity
Γ^*	reflectivity of a specular surface
<i>H</i>	Horizontal Polarization
k_a	absorption coefficient
k_{atm}	atmospheric attenuation coefficient
l_C	correlation length
l_{bl}	band-limited correlation length
<i>L</i>	scan/domain length
λ	electromagnetic wavelength
<i>MILLAS</i>	Microwave L-band Layered Sea ice emission model

<i>MODIS</i>	Moderate Resolution Imaging Spectroradiometer
<i>mss</i>	root-mean square slope
\hat{n}	normal vector
<i>NASA</i>	National Aeronautics and Space Administration, USA
<i>PDF</i>	probability distribution function
<i>PM</i>	passive microwave
<i>PSD</i>	power spectral density
<i>RFI</i>	radio frequency interference
$R(\xi)$	surface auto-correlation function
\hat{r}	antenna looking direction
<i>SMAP</i>	Soil Moisture Active and Passive
<i>SMOS</i>	Soil Moisture and Ocean Salinity
s_α	surface slope distribution parameter
σ^0	radar backscatter
σ_z	standard deviation of surface height
σ_{bl}	band-limited standard deviation of surface height
T_B	Brightness Temperature
θ	incidence angle
<i>V</i>	Vertical Polarization
<i>WEF</i>	antenna gain function
$\hat{x}, \hat{y}, \hat{z}$	Cartesian reference frame vectors
$\hat{x}', \hat{y}', \hat{z}'$	local/facet reference frame

List of Figures

- 1.1 Nadir brightness temperature vs. sea ice thickness, measurements from *SMOSice2014*, averaged every 60s. The *green dashed line* marks the *MILLAS* model prediction. The *black line* marks a linear fit for ice thicker than 0.7 m. 4
- 2.1 Example of a *SMOS* snapshot, taken south-west of Svalbard on March 24th, 2014. Individual granules of the 15 km ISEA 4H9 grid are marked with circles. The colors indicate the incidence angle associated with *DGG* pixels. The black ellipsoids illustrate the orientation and relative size of the individual measurement footprints (not to scale). 9
- 2.2 *SMOS* Antenna patterns. The -3 dB footprint contours are marked in *solid lines*, the -20 dB contours are marked in *dashed lines*. The mean antenna weighing function (Mean.*WEF*) approximation is plotted as a color background, with a color scale showed in subplot above in a cross section of the Mean.*WEF* cutting through the center. The actual size for the nadir *SMOS* measurement is showed in *green*. The elongated *elliptical red contours* correspond to the footprint at 45° incidence angle. 11
- 2.3 Sea ice thickness on March 24, 2014 derived from *SMOS*. The *SMOS* sea ice thickness product with resolution of 40 km is presented on 15 km grid. An aggregation of thick ice (>1 m) is visible along the Edgeøya's eastern coast. 12
- 2.4 Sea ice conditions in the flights region on March 24. The TerraSAR-X wide swath mode (HH polarization), with frames taken at 05:35 UTC and 14:58 UTC. The aircraft tracks are marked in red - **A** at 10:05-10:41 UTC and **B** at 11:25-12:07 UTC 13
- 2.5 Histograms of sea ice thickness along flight **A** and **B** computed from *ALS* freeboard. 15
- 2.6 Flight **A**, **Nadir** antenna (zero kilometer marks the start of the track at the coast of Edgeøya). *Thin lines* show 1 s measurements, *thick lines* mark the 30 s averaged values. The sea ice thickness from *ALS* freeboard (d_{ice}) is marked in *green*, surface temperature registered by KT19 in *cyan* ($T_{surface}$) and nadir brightness temperature ($T_B(0)$) in *black*. 16

2.7	Flight A , Side antenna (zero kilometer marks the start of the track at the coast of Edgeøya). <i>Thin lines</i> show 1 s measurements, <i>thick lines</i> mark the 30 s averaged values. The sea ice thickness from <i>ALS</i> freeboard (d_{ice}) is marked in <i>green</i> , surface temperature registered by KT19 in <i>cyan</i> ($T_{surface}$) and brightness temperatures from side-looking antenna are marked in <i>blue</i> for horizontal polarization ($T_B(H, 40)$) and <i>red</i> for vertical polarization ($T_B(V, 40)$).	17
2.8	Flight B , Nadir antenna (zero kilometer marks the start of the track at the coast of Edgeøya). <i>Thin lines</i> show 1 s measurements, <i>thick lines</i> mark the 30 s averaged values. The sea ice thickness from <i>ALS</i> freeboard (d_{ice}) is marked in <i>green</i> , surface temperature registered by KT19 in <i>cyan</i> ($T_{surface}$) and nadir brightness temperature ($T_B(0)$) in <i>black</i> .	18
2.9	Flight B , Side antenna (zero kilometer marks the start of the track at the coast of Edgeøya). <i>Thin lines</i> show 1 s measurements, <i>Thick lines</i> mark the 30 s averaged values. The sea ice thickness from <i>ALS</i> freeboard (d_{ice}) is marked in <i>green</i> , surface temperature registered by KT19 in <i>cyan</i> ($T_{surface}$) and brightness temperatures from side-looking antenna are marked in <i>blue</i> for horizontal polarization ($T_B(H, 40)$) and <i>red</i> for vertical polarization ($T_B(V, 40)$).	19
3.1	Planck curves for 300 K (<i>black solid line</i>) and 6000 K (<i>red solid line</i>). The Rayleigh-Jeans approximation is marked in <i>dashed line</i> . The L-band frequency of 1.4 GHz is marked by a blue vertical line.	22
3.2	Emissivities calculated with Fresnel equations. Horizontal (H) polarization in <i>blue solid lines</i> , Vertical polarization (V) in <i>red dashed lines</i> . The L-band permittivities of ice ($\epsilon = 3.18$) and water ($\epsilon = 81.51$) cause the difference in calculated emissivities.	23
3.3	An example of temperature (<i>black</i>) and permittivity (<i>green</i> and <i>red</i>) profiles calculated with multilayer setup of <i>MILLAS</i> . The snow permittivity $\epsilon_{snow} \approx 1.5 + 0.001i$ is not visible at this axis scale. Input values: $T_{surf} = 260$ K, $d_{snow} = 0.15$ m, $d_{ice} = 1.35$ m.	27
3.4	Surface scattering from surfaces with different degree of roughness: a) specular, b) medium-rough, c) rough. Adapted from Ulaby et al. (2014, pp. 252)	29
3.5	A Single beam transmitted through a rough surface results in a pattern of radiation in the upper medium. Similarly, the emissions from the rough surface originate from many directions. Adapted from (Ulaby et al., 2014, pp. 252)	29
3.6	Illustration of the decomposition of the surface roughness into large scale and small scale roughness.	32
3.7	Scattering approximations and their applicability domains for $\lambda = 0.21$ m. The Fraunhofer smoothness criterion for $\theta_0 = 0^\circ$ and 60° marked in <i>dashed</i> and <i>dotted</i> line, respectively. Dots mark the results of surface roughness measurements made by Landy et al. (2015), in <i>green</i> over natural sea ice, in <i>red</i> over artificially grown ice.	33

3.8	Schematic view of the faceted surface. The radiometer look direction \hat{r} is marked in <i>blue</i> . The sampling interval Δx is mark by arrow-span. The radiometer sees facets 1-3 under different local incidence angle. Facet 4 faces away from the radiometer, in this case shadowing occurs.	35
3.9	Conceptual sketch illustrating the inverse transform sampling method. u is a random number drawn from a uniform distribution $[0,1]$, than we invert the CDF_X so that $CDF_X^{-1}(u) = x$	36
3.10	Flow chart presenting the individual components of the statistical roughness model. The brightness temperature simulation is done with <i>MILLAS</i> model, with T_{surf} , d_{ice} , d_{snow} as inputs. Antenna look angle is another input parameter ($\hat{r}(\theta_0, \phi_0)$). The N -facet orientation (α_i, γ_i) is computed with inverse transform sampling <i>ITS</i> , based on cumulative distribution functions of surface slopes orientation (CDF_α). Brightness temperature contributions from respective facets are weighted with solid angles under which they are observed (Ω_i). The $T_B(\theta_0, p)$ is the end-simulated brightness temperature of a rough surface.	37
4.1	Locations of the three identified ice types smooth in <i>blue</i> , medium-deformed in <i>green</i> and deformed in <i>red</i> . In background is the TerraSAR-X wide swath mode (HH polarization), with frames taken at 05:35 UTC and 14:58 UTC. The aircraft tracks are marked in <i>black dashed</i> lines - A at 10:05-10:41 UTC and B at 11:25-12:07 UTC	40
4.2	An example of “smooth ice” region. The aerial photography shows finger rafting, a feature also visible in the <i>ALS</i> raw elevation data in the upper subplot. The photo was taken at 10:03:14 at position: 78 5' 6.39"N , 27 30' 57.75"E.	41
4.3	Histograms of the σ_z , calculated over one-second sections, for the three identified ice types.	41
4.4	The power spectral densities of surface roughness profiles over the three ice types (<i>solid black line</i>). The dashed line marks the best-fit empirical spectral model (the Lorentzian function). <i>Gray area</i> marks the sampling bandpass, ranging from f_{min} to f_{max}	42
4.5	First columns contains examples of digital elevation model (<i>DEM</i>) for three ice classes: smooth ice (a), medium-deformed ice (d) and deformed ice (g). Second column (b,e,h) presents surface facet slopes derived from the <i>DEM</i> . In the third column (c,f,i) the azimuthal orientation of the facet is shown. . .	47
4.6	The values of the distribution parameter f_R calculated along the random samples. <i>Thick red</i> line marks the average value. To illustrate the variability, we present the f_R values for several samples, marked in gray lines.	48
4.7	Histogram of surface slope distributions. The three ice types “smooth”, “medium deformed” and “deformed” are marked in blue, green, red, respectively. The <i>dashed lines</i> mark the exponential function fits to the slope histograms for “medium deformed” in <i>green</i> and “deformed” in <i>red</i>	48

5.1	Standard deviation of the 20 model runs at nadir (black) and at 40° (H -blue, V -red) as a function of number of the facets N . The horizontal <i>dashed</i> line marks the <i>EMIRAD2</i> accuracy of 0.1 K obtained after 1 s integration time.	52
5.2	Sensitivity of the modeled brightness temperature to sea ice concentration (C). The other parameters are kept constant: $T_{surf} = 260$ K, $d_{ice} = 1.42$ m, $d_{snow} = 0.14$ m, $s_\alpha = 0^\circ$	53
5.3	Sensitivity of the modeled brightness temperature to sea ice thickness (d_{ice}). The other parameters are kept constant: $T_{surf} = 260$ K, $d_{snow} = 0$ m, $s_\alpha = 0^\circ$	54
5.4	Sensitivity of modeled brightness temperature to snow thickness (d_{snow}). Other parameters are kept constant: $T_{surf} = 260$ K, $d_{ice} = 1.42$ m, $s_\alpha = 0^\circ$	56
5.5	Sensitivity of the modeled brightness temperature to surface temperature (T_{surf}). The other parameters are kept constant: $d_{ice} = 1.42$ m, $d_{snow} = 0.14$ m, $s_\alpha = 0^\circ$	57
5.6	Sensitivity of the modeled brightness temperature to sea ice roughness (s_α). The other parameters are kept constant: $T_{surf} = 260$ K, $d_{ice} = 1.42$ m, $d_{snow} = 0.14$ m	58
5.7	Absolute values of the ΔT_B caused by the “realistic” parameter variations. ($\Delta T_{surf} = 3.7$ K, $\Delta C = 5.3\%$, $\Delta d_{ice} = 0.28$ m, $0^\circ < s_\alpha < 15^\circ$). The dashed lines mark the levels of T_B change attributed to surface roughness.	60
5.8	Scatter plot of polarization difference vs. mean intensity at 40° for different model setups. The three ice types, “smooth”, “medium-deformed” and “deformed” are marked in blue, green and red, respectively. The sea ice concentration varies from 94 % to 100 %, d_{ice} from 1.2 to 1.5 m, d_{snow} from 0.12 to 0.15 m and T_{surf} 253 to 257 K and s_α varies from 0° to 15°	60
5.9	Brightness temperature as a function of the incidence angle. The family of red and blue curves represent the results for increasing s_α for each polarizations, the black lines mark the T_B curves for the smooth surface with $s_\alpha = 0^\circ$. The color of the lines intensifies with increasing surface roughness parameter from 1° to 15° . Other parameters are kept constant. ($T_{surf} = 260$ K, $d_{ice} = 1.42$ m, $d_{snow} = 0.14$ m)	62
5.10	The intensity modifying parameter H_α as a function of the roughness parameter s_α . The input T_B s were simulated with statistical roughness model for the following reference values: $T_{surf} = 260$ K, $d_{ice} = 1.42$ m, $d_{snow} = 0.14$ m.	63
5.11	The polarization mixing parameter Q_α as a function of the roughness parameter s_α . The two parametrization variants 1p and 2p are shown. The input T_B s were simulated with the statistical roughness model with the following reference values: $T_{surf} = 260$ K, $d_{ice} = 1.42$ m, $d_{snow} = 0.14$ m	64
5.12	Parameter H_α as a function of roughness plotted for a range of permittivities.	66
5.13	Parameter Q_α as a function of roughness plotted for a range of permittivities. (For the two-parameter parametrization schema)	66

5.14	Root mean square difference between simulated with statistical roughness model T_{BS} and the simplified parametrization, for several values of surface permittivity. Colors and shapes correspond to permittivity values.	67
6.1	Surface roughness parameter s_α vs. sea ice thickness derived from <i>ALS</i> . The green curve fit equation: $s_\alpha(d_{ice}) = d_{ice}^{2.53}$	73
6.2	Near-nadir brightness temperatures from <i>EMIRAD2</i> and <i>SMOS</i> vs. sea ice thickness derived from <i>ALS</i> . Error bars mark the standard deviation of sea ice thickness measurements from <i>ALS</i> and <i>SMOS</i> radiometric accuracy. . . .	74
6.3	Polarization difference against mean intensity at 40° registered by <i>SMOS</i> and <i>EMIRAD2</i> . The color coding corresponds to the value of surface roughness parameter s_α . The points with corresponding mean sea ice thickness below 0.7 m are plotted in pale color.	75
6.4	Scatterplots of modeled vs. measured brightness temperature for the nadir-looking <i>EMIRAD2</i> antenna channels ($\theta = 0^\circ$). The T_{BS} are averaged over 60 s. The simulations including geometrical roughness are placed in the right column. Flights A and B are combined.	78
6.5	Scatterplots of modeled vs. measured brightness temperature for the side-looking <i>EMIRAD2</i> antenna channels ($\theta = 40^\circ$). The T_{BS} are averaged over 60 s. The simulations including geometrical roughness are placed in the right column. Flights A and B are combined.	79
A.1	Table with parameter values used in atmospheric correction. Taken from Zine et al. (2008).	x

List of Tables

3.1	Brightness temperature simulation setup of the MI crowave L -band LA yered Sea ice emission model (<i>MILLAS</i>).	26
4.1	Ice classification summary with the number of one-second sections in each flight and corresponding sea ice thickness.	40
4.2	Surface roughness (σ_z) distribution parameters for the three ice classes.	41
4.3	Empirical models for autocorrelation function $R(\xi)$ and their <i>PSD</i> counterparts in a frequency domain.	43
4.4	Fitted Band-limited roughness parameter values (σ_{bl}, l_{bl}), for the two proposed empirical autocorrelation functions.	44
4.5	Values of the normalized χ^2	44
4.6	Facet slope distribution parameters.	46
5.1	Values of the polynomial coefficients describing the H_α and Q_α as a function of the roughness parameter s_α	63
5.2	Table with partial sensitivities of the modeled brightness temperature to the variations in input parameters: $C, d_{snow}, d_{ice}, T_{surf}, s_\alpha$. Rows labeled ΔT_B contain the brightness temperature change caused by “realistic” variation of input parameters. Partial sensitivities calculated with other values constant: $T_{surf} = 260$ K, $d_{ice} = 1.42$ m, $d_{snow} = 0.14$ m)	69
6.1	Brightness temperature simulation setup used in <i>MILLAS</i> emission model.	72
6.2	Performance of the different T_B simulation setups in terms of coefficient of determination (r^2), $RMSE(K)$, $bias(K)$, $ubRMSE(K)$. For <i>EMIRAD2</i> channels four model setups are tested: Flat no snow, Flat snow, Rough no snow, Rough snow. Nadir-looking antenna channels are treated together.	76

References

- Aagaard, K. and E. C. Carmack, 1989: The role of sea ice and other fresh water in the arctic circulation. *Journal of Geophysical Research: Oceans*, **94 (C10)**, 14 485–14 498, doi:10.1029/JC094iC10p14485, URL <http://dx.doi.org/10.1029/JC094iC10p14485>.
- Abdalati, W., et al., 2010: The ICESat-2 laser altimetry mission. *Proceedings of the IEEE*, **98 (5)**, 735–751, doi:10.1109/JPROC.2009.2034765.
- Arya, S. P. S., 1973: Contribution of form drag on pressure ridges to the air stress on arctic ice. *Journal of Geophysical Research*, **78 (30)**, 7092–7099, doi:10.1029/JC078i030p07092, URL <http://dx.doi.org/10.1029/JC078i030p07092>.
- Balling, J. E., S. S. Søbjaerg, S. S. Kristensen, and N. Skou, 2012: RFI detected by kurtosis and polarimetry: Performance comparison based on airborne campaign data. *2012 12th Specialist Meeting on Microwave Radiometry and Remote Sensing of the Environment, MicroRad 2012 - Proceedings*.
- Beckers, J. F., A. H. H. Renner, G. Spreen, S. Gerland, and C. Haas, 2015: Sea-ice surface roughness estimates from airborne laser scanner and laser altimeter observations in fram strait and north of svalbard. *Annals of Glaciology*, **56 (69)**, 235–244, doi:<https://doi.org/10.3189/2015AoG69A717>.
- Beckmann, P. and A. Spizzichino, 1963: *The scattering of electromagnetic waves from rough surfaces*. International series of monographs on electromagnetic waves, Pergamon Press; [distributed in the Western Hemisphere by Macmillan, New York].
- Bojinski, S., M. Verstraete, T. C. Peterson, C. Richter, A. Simmons, and M. Zemp, 2014: The Concept of Essential Climate Variables in Support of Climate Research, Applications, and Policy. *Bulletin of the American Meteorological Society*, **95 (9)**, 1431–1443, doi:10.1175/BAMS-D-13-00047.1, URL <http://dx.doi.org/10.1175/BAMS-D-13-00047.1>, <http://dx.doi.org/10.1175/BAMS-D-13-00047.1>.
- Burke, W. J., T. Schmugge, and J. F. Paris, 1979: Comparison of 2. 8- and 21-cm microwave radiometer observations over soils with emission model calculations. *J Geophys Res*, **84 (C1)**, 287–294, doi:10.1029/JC084iC01p00287.
- Carsey, F. D., 1992: *Microwave Remote Sensing of Sea Ice*. 68, American geophysical Union.
- Champeney, D., 1973: *Fourier Transforms and their Physical Applications*. Academic Press, London and New York.

- Chelli, Z., 2012: *e-Handbook of Statistical Methods*, <http://www.itl.nist.gov/div898/handbook/prc/section2/prc242.htm>. NIST/SEMATECH.
- Choudhury, B. J., T. J. Schmugge, A. Chang, and R. W. Newton, 1979: Effect of surface roughness on the microwave emission from soils. *Journal of Geophysical Research*, **84 (C9)**, 5699–5706, doi:10.1029/JC084iC09p05699.
- Corbella, I., F. Torres, L. Wu, N. Duffo, I. Duran, and M. Martin-Neira, 2014: Smos image reconstruction quality assessment. *International Geoscience and Remote Sensing Symposium (IGARSS)*, 1914–1916.
- Cox, G. F. N. and W. F. Weeks, 1982: Equations for determining the gas and brine volumes in sea ice samples. *CRREL Report (US Army Cold Regions Research and Engineering Laboratory)*.
- Devroye, L., 2006: Chapter 4 nonuniform random variate generation. *Simulation*, S. G. Henderson and B. L. Nelson, Eds., Elsevier, Handbooks in Operations Research and Management Science, Vol. 13, pp. 83–121, doi:10.1016/S0927-0507(06)13004-2.
- Dierking, W., 1995: Laser profiling of the ice surface topography during the Winter Weddel Gyre Study 1992. *Journal of Geophysical Research*, **100 (C3)**, 4807–4820.
- Dierking, W., 2000: RMS slope of exponentially correlated surface roughness for radar applications. *IEEE Transactions on Geoscience and Remote Sensing*, **38 (3)**, 1451–1454, doi:10.1109/36.843040.
- Entekhabi, D., H. R. Reichle, D. R. Koster, and T. W. Crow, 2010: Performance metrics for soil moisture retrievals and application requirements. *Journal of Hydrometeorology*, **11 (3)**, 832–840, doi:http://dx.doi.org/10.1175/2010JHM1223.1.
- Fung, A. K., W. Y. Liu, K. S. Chen, and M. K. Tsay, 2002: An improved iem model for bistatic scattering from rough surfaces. *Journal of Electromagnetic Waves and Applications*, **16 (5)**, 689–702, doi:http://dx.doi.org/10.1163/156939302X01119.
- Hall, D. K., J. R. Key, K. A. Casey, G. A. Riggs, and D. J. Cavalieri, 2004: Sea ice surface temperature product from MODIS. *IEEE Transactions on Geoscience and Remote Sensing*, **42 (5)**, 1076–1087, doi:10.1109/TGRS.2004.825587.
- Hendricks, S., et al., 2014: Smosice 2014: Data acquisition report. Tech. rep. URL <https://earth.esa.int/web/guest/campaignsProject:Technicalsupportforthe2014SMOSicecampaigninSESvalbardESAcontractnumber:4000110477/14/NL/FF/lfttechnicalreportNo.1,2014>.
- Huntemann, M., G. Heygster, L. Kaleschke, T. Krumpen, M. Mäkynen, and M. Drusch, 2014: Empirical sea ice thickness retrieval during the freeze-up period from SMOS high incident angle observations. *Cryosphere*, **8 (2)**, 439–451, doi:10.5194/tc-8-439-2014.
- Ivanova, N., et al., 2015: Inter-comparison and evaluation of sea ice algorithms: Towards further identification of challenges and optimal approach using passive microwave observations. *Cryosphere*, **9 (5)**, 1797–1817, doi:10.5194/tc-9-1797-2015.

- Jackson, J., 1975: *Classical Electrodynamics*, 278–282. John Wiley & Sons, New York, Chichester, Brisbane, Toronto.
- Kaleschke, L., N. Maaß, C. Haas, S. Hendricks, G. Heygster, and R. Tonboe, 2010: A sea-ice thickness retrieval model for 1.4 ghz radiometry and application to airborne measurements over low salinity sea-ice. *Cryosphere*, **4** (4), 583–592, doi:10.5194/tc-4-583-2010.
- Kaleschke, L., X. Tian-Kunze, N. Maaß, M. Mäkynen, and M. Drusch, 2012: Sea ice thickness retrieval from smos brightness temperatures during the arctic freeze-up period. *Geophysical Research Letters*, **39** (5), doi:10.1029/2012GL050916.
- Kaleschke, L., et al., 2013: SMOS Sea Ice Retrieval Study (SMOSIce), ESA Support To Science Element (STSE), Final Report ESA ESTEC. Tech. Rep. 4000101476/10/NL/CT, Univ. Hamburg, Institute of Oceanograph. URL https://icdc.cen.uni-hamburg.de/fileadmin/user_upload/icdc_Dokumente/SMOSICE_FinalReport_2013.pdf.
- Kaleschke, L., et al., 2016: SMOS sea ice product: Operational application and validation in the barents sea marginal ice zone. *Remote Sensing of Environment*, **180**, 264–273, doi:http://doi.org/10.1016/j.rse.2016.03.009.
- Kerr, Y., P. Waldteufel, P. Richaume, I. Davenport, P. Ferrazzoli, and J.-P. Wigneron, 2011: SMOS Level 2 processor soil moisture ATBD, SM-ESL (CBSA). Tech. rep. URL https://earth.esa.int/c/document_library/get_file?folderId=127856&name=DLFE-1506.pdf.
- Kerr, Y. H., et al., 2010: The SMOS: New tool for monitoring key elements of the global water cycle. *Proceedings of the IEEE*, **98** (5), 666–687, doi:10.1109/JPROC.2010.2043032.
- Ketchum, R., 1971: Airborne laser profiling of the arctic pack ice. *Remote Sensing of Environment*, **2** (C), 41–52.
- Klein, L. and C. Swift, 1977: An improved model for the dielectric constant of sea water at microwave frequencies. *IEEE Transactions on Antennas and Propagation*, **25** (1), 104–111, doi:10.1109/TAP.1977.1141539.
- Lagerloef, G., et al., 2008: The aquarius/SAC-D mission: Designed to meet the salinity remote-sensing challenge. *Oceanography*, **21** (SPL.ISS. 1), 68–81.
- Landy, J., D. Isleifson, A. Komarov, and D. Barber, 2015: Parameterization of centimeter-scale sea ice surface roughness using terrestrial lidar. *Geoscience and Remote Sensing, IEEE Transactions on*, **53** (3), 1271–1286, doi:10.1109/TGRS.2014.2336833.
- Lawrence, H., F. Demontoux, J. P. Wigneron, P. Paillou, T. D. Wu, and Y. H. Kerr, 2011: Evaluation of a numerical modeling approach based on the finite-element method for calculating the rough surface scattering and emission of a soil layer. *IEEE Geoscience and Remote Sensing Letters*, **8** (5), 953–957, doi:10.1109/LGRS.2011.2131633.
- Lawrence, H., J. . Wigneron, F. Demontoux, A. Mialon, and Y. H. Kerr, 2013: Evaluating the semiempirical H-Q model used to calculate the L-band emissivity of a rough bare soil.

- IEEE Transactions on Geoscience and Remote Sensing*, **51** (7), 4075–4084, doi:10.1109/TGRS.2012.2226995.
- Laxon, S. W., et al., 2013: Cryosat-2 estimates of arctic sea ice thickness and volume. *Geophysical Research Letters*, **40** (4), 732–737, doi:10.1002/grl.50193, URL <http://dx.doi.org/10.1002/grl.50193>.
- Le Vine, D. M., S. Abraham, Y. H. Kerr, W. J. Wilson, N. Skou, and S. S. Søbærg, 2005: Comparison of model prediction with measurements of galactic background noise at L-band. *IEEE Transactions on Geoscience and Remote Sensing*, **43** (9), 2018–2022, doi:10.1109/TGRS.2005.853190.
- Liu, C., J. Chao, W. Gu, L. Li, and Y. Xu, 2014: On the surface roughness characteristics of the land fast sea-ice in the Bohai Sea. *Acta Oceanologica Sinica*, **33** (7), 97–106, doi:10.1007/s13131-014-0509-3.
- Loose, B., et al., 2011: Gas diffusion through columnar laboratory sea ice: implications for mixed-layer ventilation of CO₂ in the seasonal ice zone. *Tellus B: Chemical and Physical Meteorology*, **63** (1), 23–39, doi:10.1111/j.1600-0889.2010.00506.x, URL <http://dx.doi.org/10.1111/j.1600-0889.2010.00506.x>, <http://dx.doi.org/10.1111/j.1600-0889.2010.00506.x>.
- Maaß, N., L. Kaleschke, X. Tian-Kunze, and M. Drusch, 2013: Snow thickness retrieval over thick arctic sea ice using smos satellite data. *Cryosphere*, **7** (6), 1971–1989, doi:10.5194/tc-7-1971-2013.
- Maaß, N., L. Kaleschke, X. Tian-Kunze, and R. T. Tonboe, 2015: Snow thickness retrieval from l-band brightness temperatures: A model comparison. *Annals of Glaciology*, **56** (69), 9–17, doi:<https://doi.org/10.3189/2015AoG69A886>.
- Martín-Neira, M., et al., 2016: SMOS instrument performance and calibration after 6years in orbit. *Remote Sensing of Environment*, doi:10.1016/j.rse.2016.02.036, article in Press.
- Mattia, F. and T. Le Toan, 1999: Backscattering properties of multi-scale rough surfaces. *Journal of Electromagnetic Waves and Applications*, **13** (4), 493–527, doi:10.1163/156939399X00240.
- Matzler, C. and A. Standley, 2000: Relief effects for passive microwave remote sensing. *International Journal of Remote Sensing*, **21** (12), 2403–2412, doi:10.1080/01431160050030538.
- Maykut, G. A., 1978: Energy exchange over young sea ice in the central Arctic. *Journal of Geophysical Research: Oceans*, **83** (C7), 3646–3658, doi:10.1029/JC083iC07p03646, URL <http://dx.doi.org/10.1029/JC083iC07p03646>.
- Maykut G., U. N., 1971: Some results from a time- dependent thermodynamic model of sea ice. *J Geophys Res*, **76** (6), 1550–1575, doi:10.1029/JC076i006p01550.

- McMullan, K. D., M. A. Brown, M. Martín-Neira, W. Rits, S. Ekholm, J. Marti, and J. Lemanczyk, 2008: SMOS: The payload. *IEEE Transactions on Geoscience and Remote Sensing*, **46** (3), 594–605, doi:10.1109/TGRS.2007.914809.
- Mills, P. and G. Heygster, 2011: Sea ice emissivity modeling at L-band and application to 2007 Pol-Ice campaign field data. *IEEE Transactions on Geoscience and Remote Sensing*, **49** (2), 612–617, doi:10.1109/TGRS.2010.2060729.
- Mironov, V. L., Y. H. Kerr, L. G. Kosolapova, I. V. Savin, and K. V. Muzalevskiy, 2015: A temperature-dependent dielectric model for thawed and frozen organic soil at 1.4 GHz. *IEEE Journal of Selected Topics in Applied Earth Observations and Remote Sensing*, **8** (9), 4470–4477, doi:10.1109/JSTARS.2015.2442295.
- Mäkynen, M., B. Cheng, and M. Similä, 2013: On the accuracy of thin-ice thickness retrieval using MODIS thermal imagery over arctic first-year ice. *Annals of Glaciology*, **54** (62), 87–96, doi:10.3189/2013AoG62A166.
- Obbard, R. W., G. Troderman, and I. Baker, 2009: Imaging brine and air inclusions in sea ice using micro-X-ray computed tomography. *Journal of Glaciology*, **55** (194), 113–115.
- Oh, Y. and Y. C. Kay, 1998: Condition for precise measurement of soil surface roughness. *IEEE Transactions on Geoscience and Remote Sensing*, **36** (2), 691–695, doi:10.1109/36.662751.
- O’Neill, P., D. Entekhabi, E. Njoku, and K. Kellogg, 2010: The nasa soil moisture active passive (smap) mission: Overview. 3236–3239, doi:10.1109/IGARSS.2010.5652291.
- Panofsky Hans A. and Brier Glenn W., 1958: *Some applications of statistics to meteorology*. Pennsylvania State University Press.
- Peng, J., E. Kim, and J. Piepmeier, 2013: Global simplified atmospheric radiative transfer model at L-band. *IEEE Geoscience and Remote Sensing Letters*, **10** (3), 437–440, doi:10.1109/LGRS.2012.2208213.
- Petty, A. A., M. C. Tsamados, N. T. Kurtz, S. L. Farrell, T. Newman, J. P. Harbeck, D. L. Feltham, and J. A. Richter-Menge, 2016: Characterizing Arctic sea ice topography using high-resolution IceBridge data. *The Cryosphere*, **10** (3), 1161–1179, doi:10.5194/tc-10-1161-2016, URL <http://www.the-cryosphere.net/10/1161/2016/>.
- Prigent, C. and P. Abba, 1990: Sea surface equivalent brightness temperature at millimeter wavelengths. *Annales Geophysicae [0992-7689]*, **8**, 627–634.
- Rice, S. O., 1951: Reflection of electromagnetic waves from slightly rough surfaces. *Communications on Pure and Applied Mathematics*, **4** (2-3), 351–378, doi:10.1002/cpa.3160040206.
- Ricker, R., S. Hendricks, V. Helm, H. Skourup, and M. Davidson, 2014a: Sensitivity of CryoSat-2 Arctic sea-ice freeboard and thickness on radar-waveform interpretation.

- The Cryosphere*, **8** (4), 1607–1622, doi:10.5194/tc-8-1607-2014, URL <http://www.the-cryosphere.net/8/1607/2014/>.
- Ricker, R., S. Hendricks, V. Helm, H. Skourup, and M. Davidson, 2014b: Sensitivity of CryoSat-2 Arctic sea-ice freeboard and thickness on radar-waveform interpretation. *Cryosphere*, **8** (4), 1607–1622, doi:10.5194/tc-8-1607-2014.
- Rivas, M., J. Maslanik, J. Sonntag, and P. Axelrad, 2006: Sea ice roughness from airborne lidar profiles. *Geoscience and Remote Sensing, IEEE Transactions on*, **44** (11), 3032–3037, doi:10.1109/TGRS.2006.875775.
- Schanda, E., 1986a: *Physical Fundamentals of Remote Sensing*, 143–145. Springer-Verlag Berlin heidelberg New York Tokyo.
- Schanda, E., 1986b: *Physical Fundamentals of Remote Sensing*, 120–128. Springer-Verlag Berlin heidelberg New York Tokyo.
- Schönwiese, C.-D., 2013: *Praktische Statistik für Meteorologen und Geowissenschaftler*, 25–29. Gebr. Borntraeger Verlagsbuchhandlung, Stuttgart, Germany.
- Søbjaerg, S., S. Kristensen, J. Balling, and N. Skou, 2013: The airborne emirad l-band radiometer system. 1900–1903, doi:10.1109/IGARSS.2013.6723175.
- Soldo, Y., F. Cabot, A. Khazaal, M. Miernecki, E. Słomińska, R. Fieuzal, and Y. H. Kerr, 2015: Localization of rfi sources for the smos mission: A means for assessing smos pointing performances. *IEEE Journal of Selected Topics in Applied Earth Observations and Remote Sensing*, **8** (2), 617–627.
- Stroeve, J. C., et al., 2006: Impact of surface roughness on AMSR-E sea ice products. *IEEE Transactions on Geoscience and Remote Sensing*, **44** (11), 3103–3116, doi:10.1109/TGRS.2006.880619.
- Strübing, K. and J. Schwarz, 2014: Die Eisverhältnisse in der Barentssee während der IRO-2-Testfahrt mit R/V Lance 17. – 27.03.2014. Tech. rep. Abschlussbericht vorgelegt von JS Consulting, Großhansdorf, im Auftrag des AWI, Bestellnummer 12/45086354 zum Werkvertrag Vor -/Nachbereitung und Durchführung der IRO-2-Testfahrt im Rahmen des Vorhabens Entwicklung und Optimierung eines Ozean-Meereis Vorhersagemodells für das Nordpolarmeer, BMWi-Förderkennzeichen: 03SX328H.
- Suess, M., P. Matos, A. Gutiérrez, M. Zundo, and M. Martin-Neira, 2004: Processing of SMOS level 1C data onto a discrete global grid. *International Geoscience and Remote Sensing Symposium (IGARSS)*, Vol. 3, 1914–1917, doi:10.1109/IGARSS.2004.1370716.
- Tian-Kunze, X., L. Kaleschke, N. Maaß, M. Mäkynen, N. Serra, M. Drusch, and T. Krumpen, 2014: SMOS-derived thin sea ice thickness: Algorithm baseline, product specifications and initial verification. *Cryosphere*, **8** (3), 997–1018, doi:10.5194/tc-8-997-2014.
- Timco, G. and W. Weeks, 2010: A review of the engineering properties of sea ice. *Cold Regions Science and Technology*, **60** (2), 107–129, doi:10.1016/j.coldregions.2009.10.003.

- Tiuri, M. E., A. H. Sihvola, E. G. Nyfors, and M. T. Hallikaiken, 1984: The complex dielectric constant of snow at microwave frequencies. *IEEE Journal of Oceanic Engineering*, **9** (5), 377–382, doi:10.1109/JOE.1984.1145645.
- Tsamados, M., D. L. Feltham, D. Schroeder, D. Flocco, S. L. Farrell, N. Kurtz, S. W. Laxon, and S. Bacon, 2014: Impact of Variable Atmospheric and Oceanic Form Drag on Simulations of Arctic Sea Ice. *Journal of Physical Oceanography*, **44** (5), 1329–1353, doi:10.1175/JPO-D-13-0215.1, URL <http://dx.doi.org/10.1175/JPO-D-13-0215.1>, <http://dx.doi.org/10.1175/JPO-D-13-0215.1>.
- Ulaby, F. T., et al., 2014: *Microwave radar and radiometric remote sensing*. University of Michigan Press Ann Arbor.
- Untersteiner, N., 1964: Calculations of temperature regime and heat budget of sea ice in the central arctic. *Journal of Geophysical Research*, **69** (22), 4755–4766, doi:10.1029/JZ069i022p04755, URL <http://dx.doi.org/10.1029/JZ069i022p04755>.
- Vant, M. R., R. O. Ramseier, and V. Makios, 1978: The complex-dielectric constant of sea ice at frequencies in the range 0.1-40 GHz. *Journal of Applied Physics*, **49** (3), 1264–1280.
- Vine, D. M. L. and S. Abraham, 2004: Galactic noise and passive microwave remote sensing from space at l-band. *IEEE Transactions on Geoscience and Remote Sensing*, **42** (1), 119–129, doi:10.1109/TGRS.2003.817977.
- Wang, J. R. and B. J. Choudhury, 1981: Remote sensing of soil moisture content over bare field at 1.4 GHz frequency. *Journal of Geophysical Research*, **86** (C6), 5277–5282, doi:10.1029/JC086iC06p05277.
- Wang, J. R., J. C. Shiue, and J. E. McMurtrey, 1980: Microwave remote sensing of soil moisture content over bare and vegetated fields. *Geophysical Research Letters*, **7** (10), 801–804, doi:10.1029/GL007i010p00801, URL <http://dx.doi.org/10.1029/GL007i010p00801>.
- Warren, S. G., I. G. Rigor, N. Untersteiner, V. F. Radionov, N. N. Bryazgin, Y. I. Aleksandrov, and R. Colony, 1999: Snow depth on arctic sea ice. *Journal of Climate*, **12** (6), 1814–1829, doi:10.1175/1520-0442(1999)012<1814:SDOASI>2.0.CO;2.
- Wigneron, J. ., et al., 2011: Evaluating an improved parameterization of the soil emission in L-MEB. *IEEE Transactions on Geoscience and Remote Sensing*, **49** (4), 1177–1189, doi:10.1109/TGRS.2010.2075935.
- Wingham, D. J., et al., 2006: Cryosat: A mission to determine the fluctuations in earths land and marine ice fields. *Advances in Space Research*, **37**, 841–871, doi:10.1016/j.asr.2005.07.027.
- Yu, Y. and D. A. Rothrock, 1996: Thin ice thickness from satellite thermal imagery. *Journal of Geophysical Research C: Oceans*, **101** (C11), 25 753–25 766, doi:10.1029/96JC02242.
- Zine, S., et al., 2008: Overview of the smos sea surface salinity prototype processor. *IEEE Transactions on Geoscience and Remote Sensing*, **46** (3), 621–645.

-
- Zwally, H. J., et al., 2002: ICESat's laser measurements of polar ice, atmosphere, ocean, and land. *Journal of Geodynamics*, **34** (3-4), 405–445, doi:10.1016/S0264-3707(02)00042-X.
- Zygmuntowska, M., P. Rampal, N. Ivanova, and L. H. Smedsrud, 2014: Uncertainties in arctic sea ice thickness and volume: New estimates and implications for trends. *Cryosphere*, **8** (2), 705–720, doi:10.5194/tc-8-705-2014.
- Øystein Jensen, 2016: The international code for ships operating in polar waters: Finalization, adoption and law of the sea implications. *Arctic Review*, **7** (1), URL <https://arcticreview.no/index.php/arctic/article/view/236>.

Danksagung

I am very grateful to Prof. Dr. Lars Kaleschke for his guidance, helpful consultations, patience and constructive remarks during past years.

Likewise, I would like to thank advisory panel members Prof. Dr. Stefan Bühler, Prof. Dr. Gualtiero Badin and in my first year Prof. Dr. Alexander Löw.

Thanks go to the HGF Alliance, Remote Sensing and Earth System Dynamics that financed my work, and provided great opportunities for fruitful discussions and networking.

The author acknowledges the institutions providing the data and people involved in carrying out the measurements. The European Space Agency co-financed the AWI research aircraft Polar 5 and helicopter flights (ESA contract 4000110477/14/NL/FF/lf; PI S.Hendricks) and the development and validation of SMOS sea ice thickness retrieval methods (ESA contracts 4000101476/10/NL/CT and 4000112022/14/I-AM; PI L.Kaleschke). Stefan Hendricks for pre-processing the ALS data. Technical University of Denmark (DTU) co-financed and conducted the measurements with EMIRAD2 L-band radiometer on Polar 5 made by Sten Schmidl Søbjaerg . The TerraSAR-X and TanDEM-X teams for providing the SAR data for this study.

I thank my office mates, Alexander Beitsch, Andreas Wernecke, Nina Maaß, Amelie Tetzlaff, Valentin Ludwig, Xiangshan Tian-Kunze, Louisa Tiemann, Mara Muchow, Zoe Rehder for the great time we had, and support from ACTD group.

Many thanks, to other friends from the Institute of Oceanography and from the University for their friendship and support. Among them the resilient core of the scientific writing group for proof reading: Julia Polkova, Marjan Ghobadian, Oleksandr Bobryshev, Norman Rüggen with his fine tuned nuclear sense of humor, Clara Burgard for arctic camping with polar bears. Last but not least, Elina Plesca who carried a disproportionate, self imposed, burden of correcting the manuscript.

Finally, I thank my family for their support and patience (Karol).

Podziękowania

Paragraf w którym autor grzecznie, acz stanowczo dziękuje licznym zastępom bliznich za okazana pomoc i wsparcie.

Erklärung

Hiermit erkläre ich an Eides statt, dass ich die vorliegende Dissertationsschrift selbst verfasst und keine anderen als die angegebenen Quellen und Hilfsmittel benutzt habe.

Hamburg, den 02.05.2017